CONFOCAL MICROSCOPY AND NUCLEAR SEGMENTATION ALGORITHM FOR QUANTITATIVE IMAGING OF EPITHELIAL TISSUE

A Dissertation

by

MEAGAN ALYSSA HARRIS

Submitted to the Office of Graduate and Professional Studies of
Texas A&M University
in partial fulfillment of the requirements for the degree of

DOCTOR OF PHILOSOPHY

Chair of Committee,	Kristen C. Maitland
Committee Members,	Javier A. Jo
	Brian E. Applegate
	Robert S. Chapkin
Head of Department,	Gerard L. Coté

August 2015

Major Subject: Biomedical Engineering

ABSTRACT

Carcinomas, cancers that originate in the epithelium, account for more than 80% of all cancers. When detected early, the 5-year survival rate is greatly increased. Biopsy and histopathology is the current gold standard for diagnosis of epithelial carcinomas which is an invasive, time-intensive, and stressful procedure. *In vivo* confocal microscopy has the potential to non-invasively image epithelial tissue in near-real time. This dissertation describes the development of a confocal microscope for imaging epithelial tissues and an image processing algorithm for segmentation of epithelial nuclei.

A rapid beam and stage scanning combination was used to acquire fluorescence confocal images of cellular and tissue features along the length of excised mouse colon. A single 1×60 mm^2 field of view is acquired in 10 seconds. Disruption of crypt structure such as size, shape, and distribution is visualized in images of inflamed colon tissue, while the normal mouse colon exhibited uniform crypt structure and distribution.

An automated pulse coupled neural network segmentation algorithm was developed for epithelial nuclei segmentation. An increase in nuclear size and the nuclear-to-cytoplasmic ratio is a potential precursor to pre-cancer development. The spiking cortical model algorithm was evaluated using a developed confocal image model of epithelial tissues with varying contrast. It was further validated on reflectance confocal images of porcine and human oral tissue from two separate confocal imaging systems. Biopsies of human oral mucosa are used to determine the tissue and system effects on measurements of nuclear-to-cytoplasmic ratio.

DEDICATION

To my late father, Martin Saldua, who instilled in me the perseverance required to overcome any obstacle.

ACKNOWLEDGEMENTS

I would like to thank my advisor, Dr. Kristen Maitland for her guidance, encouragement, and support. From our first meeting in her office, I knew she would have a positive and long-lasting impact on my life in both personal and professional capacities. I truly appreciate the dedication she has for her students and her research.

I want to acknowledge my committee members, Dr. Jo, Dr. Applegate, and Dr. Chapkin, and thank them for their guidance and support throughout the course of this research. I want to thank Evelyn Callaway for her assistance with the mouse study and Dr. Lisa Cheng for taking the time to review the pig tissue pathology. I extend my gratitude to my past and present lab members for their immeasurable support: Cory Olsovsky, Andrew Van, Dr. Joey Jabbour, Dr. Bilal Malik, and Fatemeh Nooshabadi.

Special thanks go to my friends and colleagues that I met while in graduate school, especially John Wilson. I want to thank the department faculty and staff for making my time at Texas A&M University a wonderful experience.

I would like to acknowledge the sources from which I have received funding: the Texas A&M University Diversity Fellowship, the National Action Council for Minorities in Engineering Scholars Program, the Carl Storm Underrepresented Minority Fellowship Program, U.S. Senator Phil Gramm Doctoral Fellowship, and the National Military Family Association's Joanne Holbrook Patton Military Spouse Scholarship Program.

Finally, thanks to my mother, Irma Saldua, my husband, Josh Harris, and my brothers, Marty and Damon Saldua, for their endless encouragement and love.

NOMENCLATURE

RCM	Reflectance Confocal Microscopy
PSF	Point Spread Function
FWHM	Full Width Half Maximum
FOV	Field of View
NA	Numerical Aperture
PMT	Photomultiplier Tube
NCR	Nuclear-to-Cytoplasmic Ratio
SCM	Spiking Cortical Model
PCNN	Pulse Coupled Neural Network
ANN	Artificial Neural Network
PBS	Phosphate Buffered Solution

TABLE OF CONTENTS

Page

LIST OF FIGURES

LIST OF TABLES

1. INTRODUCTION

1.1 Motivation

Carcinomas, cancers of epithelial tissues that cover the external and internal surfaces of the body, account for more than 80% of all cancers [1]. Visual or endoscopic examination followed by invasive tissue biopsy and histopathology is the current standard of care for detection and diagnosis of carcinoma. The microscopic examination of fixed, sectioned, and stained tissue includes evaluation of morphologic and architectural alterations, including increased nuclear-to-cytoplasmic ratio (NCR), enlarged nuclei, cellular pleomorphism, and irregular epithelial stratification [2]. Many carcinomas are preceded by a premalignant stage, in which the development of cancer can be prevented if detected and treated successfully. However, the clinical presentation of these precancerous lesions, such as oral leukoplakia, Barrett's esophagus, colon polyps, and actinic keratosis of the skin, can be widespread, multifocal, and/or diffuse. Furthermore, regions of premalignancy can be clinically indistinguishable from benign lesions, complicating selection of a representative site to biopsy for accurate diagnosis and staging.

In contrast to the physical sectioning of tissue required for histology, confocal microscopy achieves "optical sectioning" by spatially filtering light with a small aperture at the conjugate image plane of the microscope focus [3]. By detecting light from the focal plane and significantly rejecting out of focus light, confocal microscopy enables high resolution imaging in three dimensions of thick tissue. Recent advances in acquisition speed and miniaturization of confocal microscopes and endomicroscopes have enabled

minimally-invasive real-time imaging of cellular and tissue features *in vivo* [4-10]. These features provide information comparable to histologic characteristics of the mucosa and submucosa without the tissue excision and processing required for histology. Confocal endomicroscopes have been implemented through working channels of conventional endoscopes and as independent instruments [4]. Beyond the current clinical use of confocal microscopy to detect neoplasia in gastroenterology and dermatology, confocal imaging is currently under investigation to improve early detection of cancer and precancer in a number of other organs [11-21].

The focus of this dissertation is the development of a reflectance and fluorescence confocal microscope and image processing algorithm for large area imaging and quantitative evaluation of epithelial tissues for preclinical studies. The fluorescence confocal microscope was used to evaluate the effects of induced inflammation in murine colon tissue. Using both custom and commercial reflectance confocal microscopes, tissue and system effects on the measured NCR were qualitatively and quantitatively recorded. A nuclear segmentation algorithm based on a pulse coupled neural network was developed for automated detection of nuclei in porcine buccal mucosa for fast reporting of the NCR, average nuclear area, and number of objects present in a single frame.

1.2 Specific Aims

My research focused on the design and construction of a confocal microscope, development of a nuclear segmentation algorithm, and application of confocal imaging to epithelial tissues. My specific goals are:

1. Design and construct a large field of view, dual-mode confocal reflectance and fluorescence microscope for imaging bulk epithelial tissues for preclinical studies.

2. Evaluate colon crypt structural changes due to inflammation along the length of the colon using large area confocal fluorescence microscopy.

3. Develop an automated segmentation algorithm to segment nuclear objects in low-contrast confocal images of epithelial tissue.

4. Determine the effects of tissue sample processing, autolysis, and system axial resolution on the measurement of nuclear to cytoplasmic ratio in confocal reflectance microscopy images of epithelial tissue.

1.3 Dissertation Overview

In this dissertation, Chapter 2 gives background information on confocal microscopy, a review of literature on confocal imaging applications of epithelial tissues, and potential contrast agents for precancer or disease detection. Chapter 3 describes the custom designed dual-mode confocal microscope. Chapter 4 presents the results of the fluorescence confocal imaging of induced inflammation in the murine colon. Chapter 5 describes an automated pulse coupled neural network segmentation algorithm for segmentation of cell nuclei. Chapter 6 presents results from imaging porcine buccal mucosa and the effect of system parameters and tissue processing on nuclear to cytoplasmic ratio measured by reflectance confocal microscopy and the automated nuclear segmentation algorithm. Lastly, Chapter 7 provides a summary of results and conclusions from this research.

2. BACKGROUND*

2.1 Introduction

The goal of this research is to design and construct a dual-mode confocal microscope to characterize induced inflammation in mouse colon tissue and evaluate system and tissue effects on the measured epithelial nuclear to cytoplasmic ratio. In this section, I will review the fundamental concepts of confocal microscopy, discuss the dual-modality of the system based on fluorescence and reflectance imaging, and discuss how I tailored this custom confocal system to meet the needs of my tissue imaging studies.

2.2 Confocal Microscopy

Confocal microscopy can image bulk tissue in three dimensions with higher levels of resolution and contrast than widefield microscopy [22]. In contrast to the physical sectioning and two dimensional imaging of traditional histology, confocal imaging allows optical sectioning of bulk tissue, enabling acquisition of three dimensional images of intact tissue.

Confocal microscopy uses a point source illumination that is focused onto a sample and a point detector for collection of signal. Fig 1 shows a simple schematic of confocal microscopy [23]. If imaging in reflectance mode, the light passes through a beam splitter since the entire signal coming back from the focal plane within the sample is collected. If

---

* Part of this section is reprinted with permission from Confocal Endomicroscopy: Instrumentation and Medical Applications by Joey M. Jabbour, Meagan A. Saldua, Joel N. Bixler, and Kristen C. Maitland, 2011. Annals of Biomedical Engineering, 40(2), 378-397, Copyright 2011 by Springer New York LLC.

imaging in fluorescence mode, the beam splitter is replaced with a dichroic mirror so only the fluorescence signal is detected, not the illumination source wavelength. The light is focused to a point within the sample, and the reflectance or fluorescence signal is collected by the same lens and reflects off of the beam splitter or dichroic mirror.

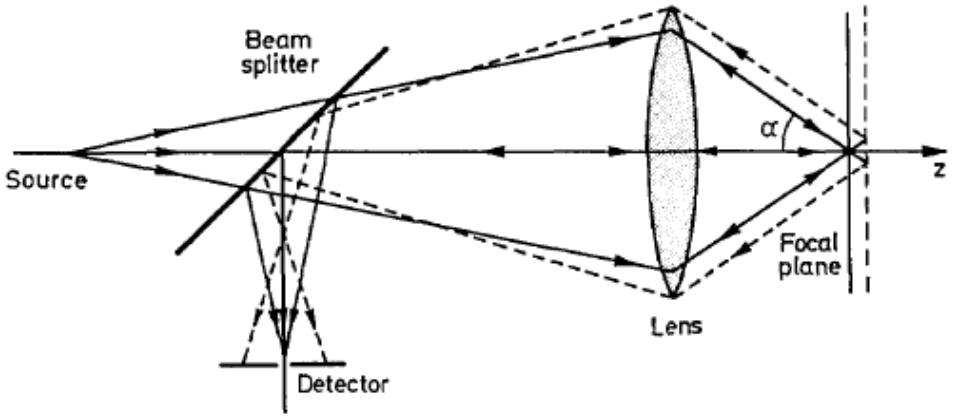

Fig 1. Simple confocal schematic showing the light path of a confocal microscope [23].

High-resolution confocal reflectance and fluorescence images of tissue are collected by placing a pinhole in front of the detector in a conjugate image plane of the focus to reject light coming from out of focus planes within the sample. In order to create a two dimensional image, the point source is scanned across the sample using a scanning technique. Fast scanning allows images to be seen in near real-time. In contrast to wide-field microscopy, the sample is illuminated a single point at a time. Moving the sample in the third axial dimension builds a three-dimensional tomographic image.

The resolution of a confocal microscope indicates the microscope's capability to separate two closely spaced points. The point spread function (PSF) of a system characterizes a system's response to a point source of light. When light is focused to a point, an Airy pattern is formed by diffraction as light passes through the circular aperture of the lens. The lateral resolution, using the PSF in the lateral plane, is defined as the radius of the first dark ring around the Airy Disk and is given by Equation 1 [3],

$$r_{Airy} = \frac{0.61\lambda}{NA_{obj}} \tag{1}$$

where λ represents the wavelength of the illumination source and NA_{obj} is the numerical aperture of the microscope objective. Lateral resolution of a confocal microscope is improved by decreasing the size of the pinhole, but there is a tradeoff when choosing the optimal pinhole size. A smaller pinhole will provide better resolution, but decrease the amount of signal detected. A larger pinhole sacrifices resolution in order to detect more signal.

The axial resolution is defined as the full width half maximum of the PSF in the axial direction and is given by Equation 2 [24],

$$z_{axial} = \frac{1.4 \cdot \lambda \cdot n}{\left(NA_{obj}\right)^2} \tag{2}$$

where n represents the index of refraction of the object medium used.

A study was performed to determine the optimal pinhole size without having to sacrifice signal or resolution [23]. This method is applicable to many optical imaging systems by converting the axial resolution equation and pinhole radius to dimensionless

optical units. The optimal pinhole size can be determined based on the wavelength of light and numerical aperture of the objective used. Equation 3 represents the normalized pinhole radius, v_p as a function of the pinhole diameter, d_p, wavelength, λ, numerical aperture of the objective, NA_{obj}, and the total system magnification, M_T.

$$v_p = \frac{\pi d_p}{\lambda} \cdot \frac{NA_{obj}}{M_T} . \tag{3}$$

Equation 4 represents the normalized axial position, u, as a function of the axial position, z, and the quarter angle of the NA instead of the half angle,

$$u = \frac{8\pi}{\lambda}\left[n \sin\left(\frac{\alpha}{2}\right)\right]^2 z . \tag{4}$$

Fig 2 demonstrates the half-width of the image, $v_{1/2}$, as a function of the normalized detector pinhole radius, v_p. This plot represents the lateral resolution of a system. For large v_p, the lateral resolution is comparable to traditional microscopy. As v_p is decreased below a value of 4, lateral resolution ($v_{1/2}$) is improved. For $v_p = 0$, no signal is permitted to the detector.

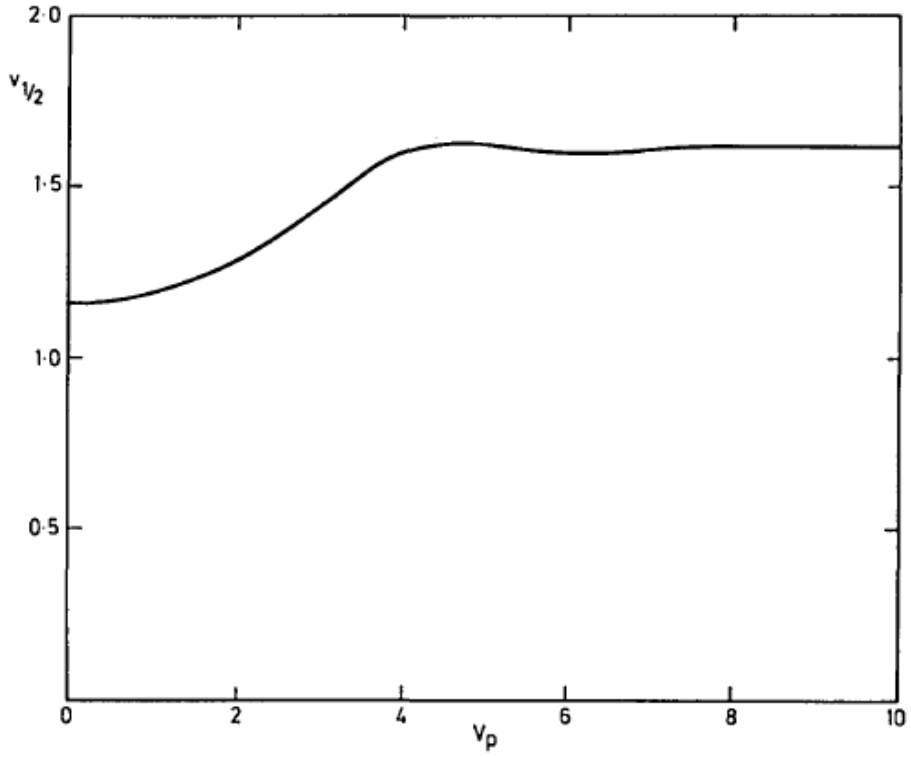

Fig 2. Half-width, $v_{1/2}$, as a function of detector pinhole size, v_p [23].

Fig 3 represents the axial resolution of an imaging system as a function of normalized pinhole radius. For v_p less than 2.5, the half-width is fairly constant; therefore a larger pinhole up to v_p = 2.5 will allow more signal to reach the detector without sacrificing axial resolution. Ideally, a pinhole size, v_p, of less than or equal to 2.5 is chosen.

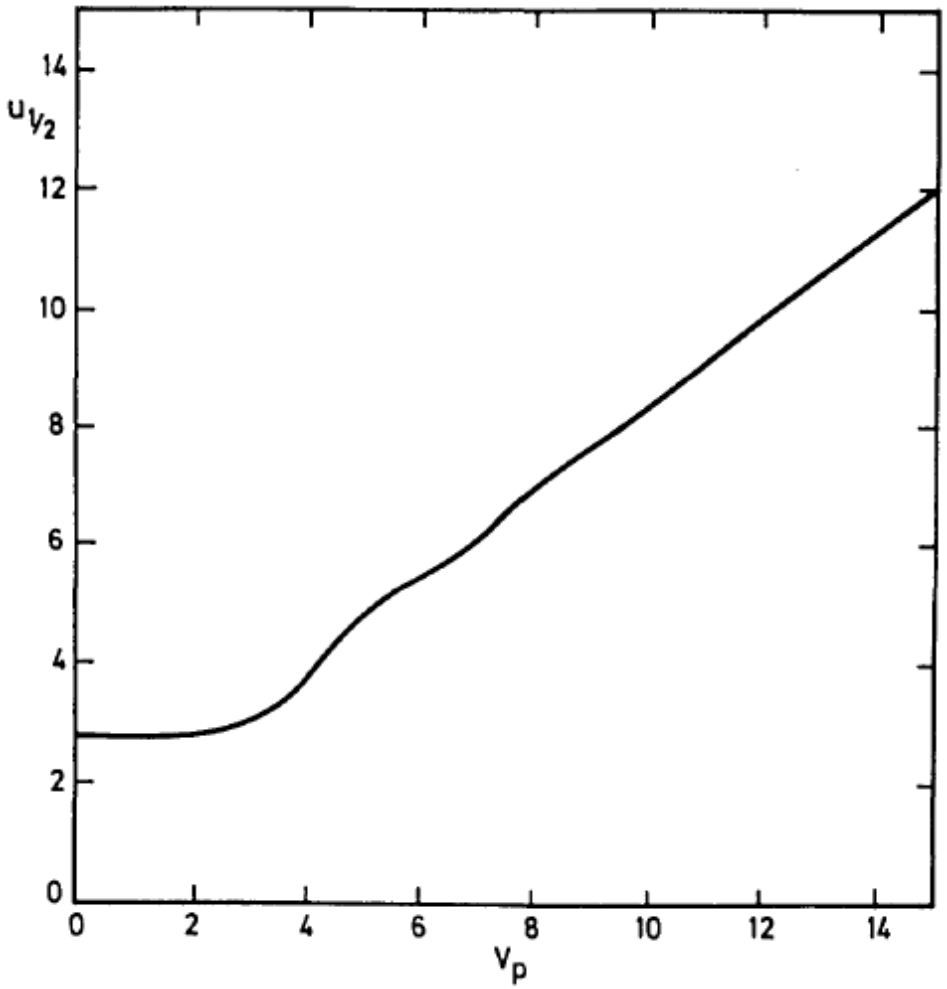

Fig 3. Half-width, $u_{1/2}$, as a function of detector pinhole size, v_p [23].

2.2.1 Medical Applications of Confocal Endomicroscopy

Early *in vivo* confocal imaging was first performed on the eye, mouth, and skin [25-28]. These accessible organs were used to demonstrate the *in vivo* cellular imaging capability of confocal imaging. However, standard microscope objective lenses, even on fiber coupled handheld probes, are incapable of imaging cavities within the body. With advancing technology endomicroscopic probes are sufficiently small in size to more

readily access areas within the body such as the gastrointestinal (GI) tract, bladder, cervix, ovary, oral cavity, and lung. Here, we present a selection of results from clinical studies of confocal endomicroscopy.

Confocal endomicroscopy has been most extensively applied to detection of diseases in the GI tract. The Optiscan/Pentax ISC-1000 has been used in numerous studies for *in vivo* imaging of cellular morphology of the mucosa in the upper and lower GI tract [29]. Cellular and subcellular structures, such as nuclei within the mucosa, colon crypts, stomach villi, and gastric pits are visible in the images. Squamous epithelium from the distal esophagus was also imaged. Fluorescent dyes are commonly used to provide contrast in fluorescence imaging of tissue. Acriflavine is administered topically to visualize nuclei, and fluorescein is administered intravenously to see the extracellular matrix and lamina propria. Fig 4 demonstrates the features visualized in the normal colon using these exogenous contrast agents. The Mauna Kea Cellvizio probe-based endomicroscopes have also been used in the upper and lower GI tract [11]. Olympus (Olympus Optical Co. Ltd., Tokyo, Japan) explored the development of a endomicroscope for use in the working channel of an endoscope to image mucosa in the GI tract [30]. Although exogenous contrast agents were not necessary to detect signal in reflectance confocal mode, the images had poor contrast and resolution, limiting resolution of nuclei within the tissue. Another confocal reflectance endomicroscopy study was performed on esophageal and stomach tissue using a prototype Mauna Kea reflectance confocal probe with improved contrast and resolution [31].

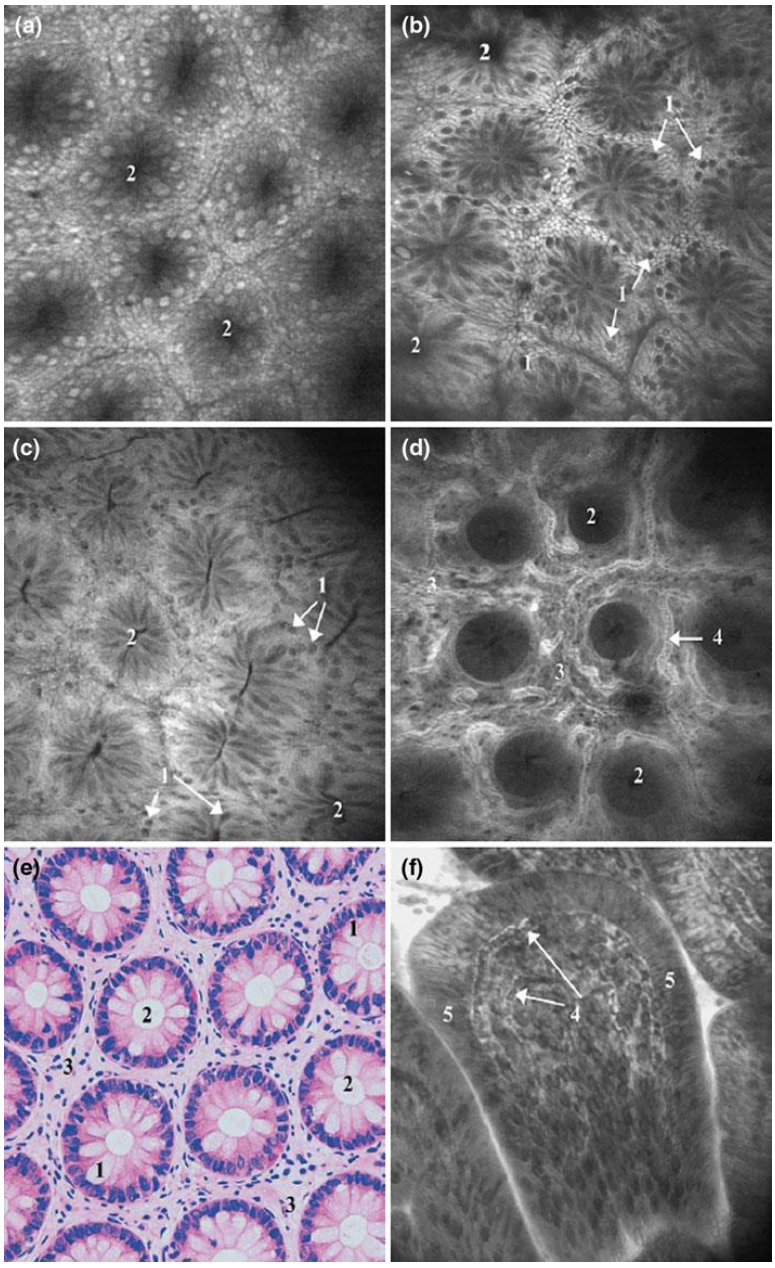

Fig 4. *In vivo* endomicroscopic imaging of the normal colon using Optiscan/Pentax. (a) First prototype with 6 mm outer diameter and (b–d, f) second prototype with 5 mm outer diameter and integrated into the Pentax EC3870 K video-endoscope. Tissue stained with topical application of acriflavine (a, b) and intravenous fluorescein (c, d). (a) Rectal mucosa; (b) descending colon mucosa; (c) cecum; (d) deeper layers of the lamina propria showing microvasculature in the descending colon; (f) terminal ileum. (e) Hematoxylin and eosin stained tissue section cut parallel to the tissue surface for comparison to en face confocal images. 500 × 500 μm field of view for all images [29].

Patients with acid reflux may develop Barrett's esophagus as a result of irritation of the epithelial lining of the esophagus from stomach acid. These patients are at a higher risk of incidence of adenocarcinoma in the esophagus. The first endomicroscopy study of Barrett's esophagus was conducted with promising results [32]. A method for classification of confocal images based on vasculature and cellular architecture was developed and presented with example images for prediction of histopathology of normal gastric epithelium, Barrett's epithelium, and neoplasia. Based on this classification system, Barrett's esophagus was predicted with 98.1% sensitivity and 94.1% specificity. Furthermore, Barrett's- associated neoplasia was predicted with 92.9% sensitivity and 98.4% specificity. The current technique for monitoring neoplastic development in Barrett's esophagus is four-quadrant biopsy, which is susceptible to sampling error. Using the Mauna Kea probe-based endomicroscope, a prospective study has shown that *in vivo* confocal imaging is ''non-inferior'' to the standard quadrant biopsy [33]. Although, the technique has potential to exclude neoplasia, it may not replace histology for surveillance of Barrett's esophagus. However, endomicroscopy may improve diagnostic yield by guiding biopsy to the area with the highest risk of neoplasia.

Celiac disease causes damage to the villi of the small intestine prohibiting vital nutrients from being absorbed into the bloodstream. This disease causes the stomach to be intolerable to gluten, which is common in many foods. Confocal laser endomicroscopy has shown potential to diagnose celiac disease [34,35]. After imaging the duodenum in six patients followed with biopsies of the interrogated tissue, confocal laser endomicroscopy successfully aided a pathological diagnosis of four normal and two

positive for celiac disease [35]. Another study supports diagnosis of celiac disease with sensitivity of 94% and specificity of 92% using confocal endomicroscopy and suggests that abnormalities not seen in histology could possibly be detected [34].

Patients with inflammatory bowel disease, including ulcerative colitis and Crohn's disease, have an increased risk of developing colorectal cancer and are recommended to begin colonoscopy screening at an earlier age. Random or step biopsy may be recommended for surveillance in ulcerative colitis, which is prone to sampling error. Confocal endomicroscopy is being evaluated as a tool to target regions suspicious for neoplasia to guide biopsy in patients with ulcerative colitis. Differences can be seen between endomicroscopic images of normal tissue and non-active or active ulcerative colitis [36]. Normal colon mucosa has crypts that are small and regularly arranged within the tissue. Non-active ulcerative colitis also displays small crypts, but in an irregular arrangement, while active ulcerative colitis has an unidentifiable structure with large crypt lumens. In future research, it will be important to determine whether low-grade dysplasia can be differentiated from benign lesions with inflammation.

The colon and rectum are in the top five sites for cancer incidence in the United States, with an age adjusted incidence approaching 50 per 100,000 people [37]. Additionally, colorectal cancer has a low 5-year relative survival rate of 64%. Patients with high risk for colorectal cancer based on personal or family history are recommended to have periodic colonoscopy screening. Colorectal cancers primarily originate in adenomatous polyps, which are typically removed during endoscopic evaluation, whether they are neoplastic or not. Some lesions develop from flat or depressed lesions that are

difficult to detect by traditional white light endoscopy, and would also be difficult to detect with confocal endomicroscopy based on the small field of view (FOV). Kiesslich et al. published the first results on the diagnostic capability of confocal endomicroscopy in colorectal intraepithelial neoplasia and cancer in 2004 [38]. The goal was to predict histology while patients were undergoing a colonoscopy screening for colorectal cancer. Neoplastic changes within the tissue were predicted with high accuracy, including a sensitivity of 97.4% and specificity of 99.4%. The classification of confocal images was based on patterns in the vessel and crypt architecture. As mentioned previously, normal crypts are regularly arranged in a hexagonal pattern, while neoplastic tissue is distorted and irregular. This method would allow for faster diagnosis of endoscopically observable neoplasia and would potentially limit the number of unnecessary biopsies. In contrast to intraepithelial neoplasia and cancer, hyperplastic polyps are considered to be nonneoplastic tissue and are not required to be removed. A recent prospective study from another group to differentiate adenomas from non-neoplastic polyps using a basic classification system reported a sensitivity of 93.9% and a specificity of 95.9% compared with histology [39]. Meining et al. reported similar results using the probe-based endomicroscopy with a sensitivity of 92.3% and specificity of 91.3% [11].

Gastric cancer is speculated to be a multistep progression that is initially triggered by an infection of Helicobacter pylori (H. pylori), which progresses to intestinal metaplasia, chronic gastritis, intraepithelial neoplasia, and then cancer. With the aid of confocal endomicroscopy, H. pylori may be diagnosed in the gastric epithelium *in vivo* [40]. Confocal images of gastric mucosa demonstrate similarities with histology images

for fundic gland mucosa, pyloric gland mucosa, and adenocarcinoma of the stomach [41]. While confocal imaging in the GI tract has predominantly been performed in fluorescence mode using exogenous contrast agents, reflectance confocal endomicroscopy was also evaluated for the diagnosis of gastroesophageal cancer in its early stages [31]. Features of the normal esophagus show high reflectivity from nuclei and cellular honeycomb-like structure. Cancer in the esophagus appeared to have an increase in nuclear to cytoplasmic ratio, and the reflectivity from cell membranes was not seen. Normal gastric mucosa exhibits crypt cells arranged in a flower pattern around the gastric pit. Within differentiated adenocarcinoma, cell membranes were not apparent and glandular structures were disorganized.

Confocal laser endomicroscopy was performed using the Cellvizio instrument by Mauna Kea Technologies to image the human bladder *in vivo* [42]. Fluorescein was administered intravesically and/or intravenously following the standard white light cystoscopy procedure. Fluorescein provided contrast allowing for differentiation between normal bladder mucosa and low- and high-grade bladder tumors. Large umbrella cells near the surface with smaller cells nearing the lamina propria were visible in the bladder mucosa. Tumors classified as low grade had normal appearing small cells that were densely packed. In contrast, high-grade bladder tumors had an irregular architecture. A paper published from the same group sought to develop criteria for diagnosing benign and neoplastic mucosa along the urinary tract using confocal endomicroscopy [13]. Here, the Cellvizio system was used in conjunction with white light cytoscopy for faster diagnosis of urinary tract conditions such as bladder cancer. Confocal

images taken along the urinary tract are seen in Fig 5 with fluorescein as a contrast agent [13]. Regions located on the lower part of the urinary tract were taken *in vivo*, and those along the upper regions were acquired *ex vivo*. Comparable features, such as intermediate cells within the urothelium, were seen in the ureter and bladder. With the availability of smaller diameter probes, imaging of the upper urinary tract *in vivo* will likely be possible in the near future.

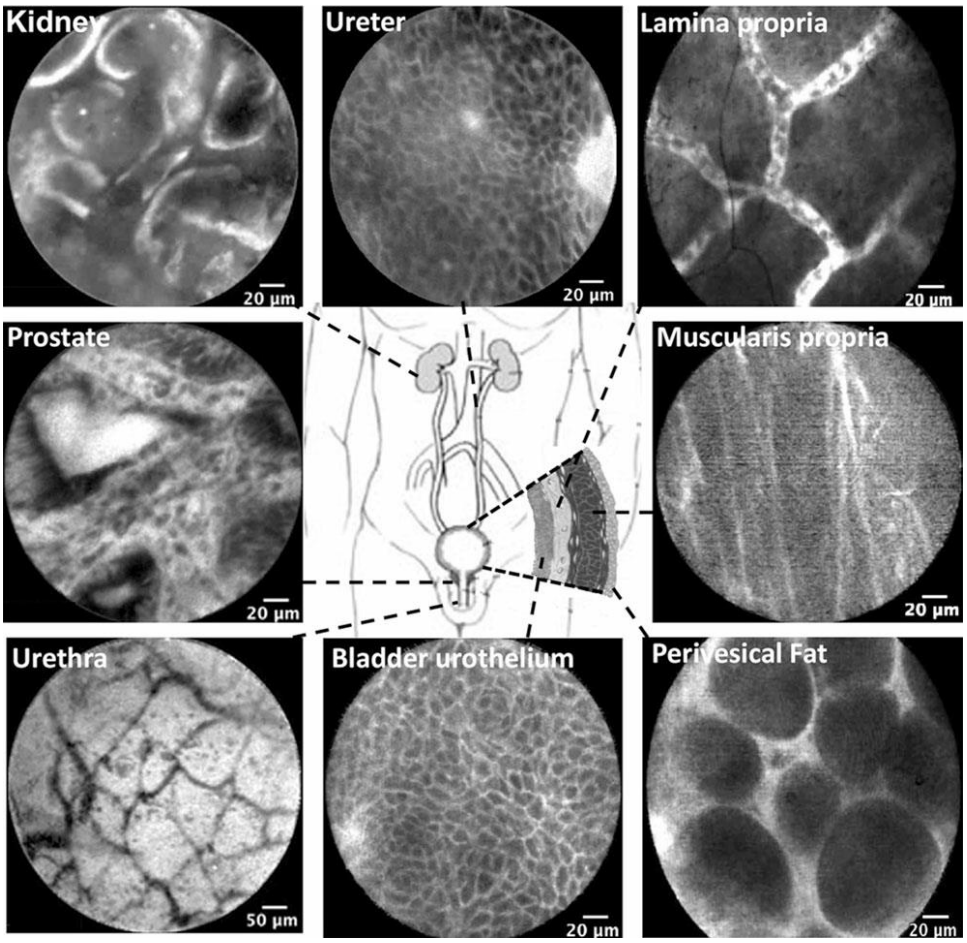

Fig 5. Confocal laser endomicroscopy images of the normal urinary tract using the Cellvizio system (Mauna Kea Technologies). Images of the lower urinary tract were acquired *in vivo*: lamina propria, prostate, muscularis propria, urethra, bladder urothelium, and perivesical fat. Images of the upper urinary tract were acquired *ex vivo*: kidney and ureter. All scale bars: 20 µm with exception of urethra, 50 µm [13].

Cervical intraepithelial neoplasia (CIN) may progress to cervical cancer, the second leading cause of cancer in women in the world after breast cancer. 3–5% acetic acid is commonly used on the cervix during colposcopy to visualize regions with increased nuclear density suspected to be CIN. This effect, termed acetowhitening because of the whitening of the lesions, also provides contrast in reflectance confocal microscopy of epithelial tissue, so that nuclei throughout the epithelium can be visualized and nuclear to cytoplasmic ratio can be quantified [43]. Reflectance confocal endomicroscopy with colposcopic guidance has been explored to detect CIN [44]. In confocal images of normal epithelium, the nuclear to cytoplasmic ratio increases from the differentiated superficial epithelium to the dense basal epithelium; whereas, in high-grade CIN, the nuclear to cytoplasmic ratio is high near the surface and deeper in the epithelium [45]. Fluorescence confocal imaging of the cervix using the Optiscan F900e confocal system coupled with a rigid endomicroscope probe was performed to evaluate assessment of CIN quantitatively and qualitatively [46]. Normal and abnormal locations within the cervix were imaged after application of 5% acetic acid and topical application of acriflavine. Similar to reflectance imaging, CIN was characterized by an increase in nuclear density, size, and cellular disorganization.

Ovarian cancer has an exceptionally low 5-year relative survival rate, below 45% [37]. Screening is critical for high risk populations, but is complicated by limited access to the ovaries. A multispectral fluorescence confocal microlaparoscope using proximal line scanning was used in a study to evaluate *in vivo* confocal imaging of the ovary to potentially aid diagnosis of ovarian cancer [18]. Images are acquired

following staining the ovary with fluorescein sodium *in vivo* and acridine orange following ovary extraction. Imaging was performed on patients undergoing oophorectomy. The surgeon located an ovary and isolated it in an endobag to protect the patient from the imaging dye. The confocal images of the normal epithelial surface of the ovary have a homogenous pattern of cells with bright nuclei. Cancerous tissue appears irregular at the surface and heterogeneous. Acridine orange provided superior contrast; although it is not yet approved for *in vivo* imaging of the ovary, the safety is being evaluated for clinical use.

The oral cavity consists of a diverse range of epithelial tissue, including the lips, buccal mucosa, dorsal and ventral tongue, hard and soft palate, gingiva, salivary glands, and floor of the mouth. The site with the highest oral cancer incidence is the tongue. Most oral cancers are carcinomas, tumors occurring in the stratified squamous epithelium that develop from the uncontrolled growth of cells. In the United States, the age-adjusted incidence rate for cancers of the oral cavity and pharynx was over 10 per 100,000 persons and the 5-year relative survival rate was 60% in the period from 2004 to 2008 [37]. There are many detection and treatment methods that are being developed and improved to achieve more efficient detection and diagnosis of oral cancer, such as confocal endomicroscopy [47]. By optical sectioning and visualization of cellular structure, malignant lesions may be able to be differentiated from benign lesions and normal mucosa. In reflectance confocal endomicroscopy, contrast is provided by differences in refractive index. Addition of vinegar or acetic acid (3–6%) enhances backscattering from the nuclei in epithelial tissue, improving contrast in confocal imaging

[43]. A miniaturized fiber reflectance confocal endomicroscope was used to image 20 sites in the oral cavity on eight patients that were undergoing surgery for squamous cell carcinoma [16]. Nuclear morphology was distinctly different for normal, Fig 6a – 6b and abnormal oral tissue Fig 6(d, e). The normal tissue had an organized structure, while dysplastic tissue appeared disrupted with overlapping nuclei within the images. The cancerous tissue also exhibited severe disorganization. Nuclei were not always visible and if so, they were not distributed evenly. Acetic acid was used to enhance contrast within the confocal images. *In vivo* fluorescence confocal endomicroscopy of the human oropharynx after intravenous injection of fluorescein was recently reported as a novel means to differentiate various locations of the oropharyngeal mucosa [48]. Following injection of fluorescein, capillary networks and cell borders have fluorescence contrast. Cell nuclei are not visible because the cell membrane is not permeable to fluorescein. Confocal images of invasive carcinoma on the floor of the mouth show increased signal due to neoangiogenesis and leaky blood vessels. *In vivo* imaging of vocal cords is being explored by confocal endomicroscopy with potential to expand understanding of pediatric laryngeal development, currently limited by insufficient availability of pediatric laryngeal specimens [19]. Preliminary imaging results with spectrally encoded confocal microscopy in porcine tissue demonstrate the potential for endomicroscopic imaging of the vocal folds. Images portraying epithelial cells, the basement membrane, and the lamina propria were obtained down to 375 μm deep in the tissue. Imaging and characterization of lesions is another potential application of confocal endomicroscopy of the vocal fold, where unnecessary removal of tissue should be minimized for voice preservation [49].

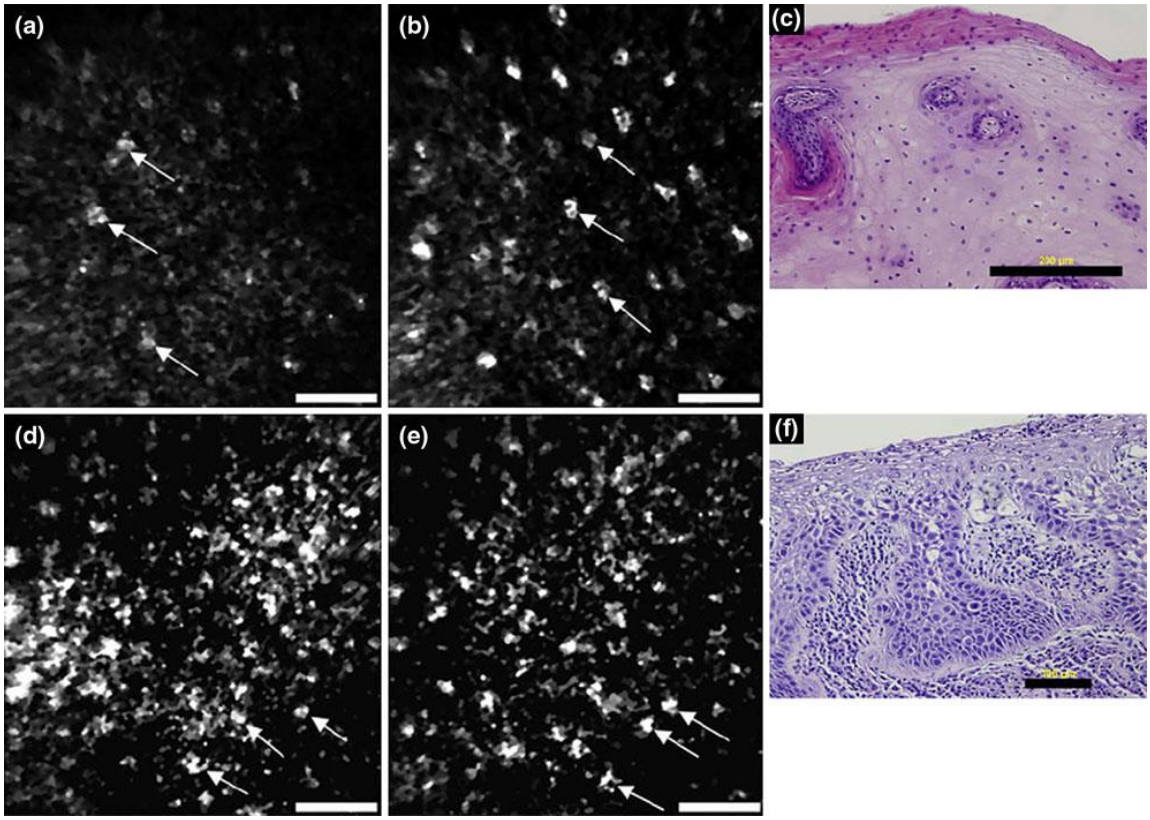

Fig 6. *In vivo* reflectance confocal endomicroscopy of normal oral mucosa. From the ventral tongue (a, b) and moderate dysplasia on the floor of the mouth (d, e) with corresponding histology images (c, f). Scale bars: (a, b, d, e) 50 μm, (c) 200 μm, (f) 100 μm [16].

A confocal fluorescence endomicroscope with spectral detection was used to image bronchial mucosa during a bronchoscopy procedure allowing a depth of focus of 50 μm below the surface [50]. Twenty-nine high risk patients for lung cancer had *in vivo* imaging and spectral analysis. The tracheobronchial tree was imaged and distinct patterns of the subepithelial fiber network were visible. All specimens diagnosed as histologically normal exhibited a similar pattern. In precancerous tissue, a decrease in intensity was seen as well as a disorganized fiber network within the bronchial wall. Contained within the instrument channel of an endoscope, a confocal endomicroscope has the potential to

distinguish normal bronchial epithelium from pre-neoplastic lesions *in vivo* [51]. Cresyl violet was used as a contrast agent. Due to its acidic nature, which may be fatal to humans if administered in the lungs, the contrast agent was used with an altered pH for imaging of bronchial mucosa. Two bronchoscopes were used for the bronchoscopy and confocal endomicroscopy procedures, with the second one able to house a channel for the confocal endomicroscope. Normal epithelium exhibited uniformly distributed cells, while mild to moderate dysplasia displayed heterogeneous tissue architecture. Distal lung imaging is being explored via broncho-alveoscopy procedures [52]. This is the first technique capable of imaging lobular and alveolar structures within the human lung.

2.2.2 Contrast Agents for Confocal Endomicroscopy

In order to achieve good imaging contrast within fluorescence confocal images, it is common to apply an exogenous contrast agent to the tissue. Currently, only a few contrast agents are frequently reported in the literature for *in vivo* use in humans for endomicroscopy: acetic acid, fluorescein sodium, acriflavine hydrocholoride, and cresyl violet [51,53]. Contrast agents approved for *in vivo* use for optical imaging by the United States Food and Drug Administration are acetic acid, fluorescein sodium, and indocyanine green [54,55].

Intravenous fluorescein sodium is most commonly used in the colon, esophagus, and stomach. Twenty seconds after injection of fluorescein, the agent is distributed throughout the tissue and can last 30 min allowing for imaging of 250 μm below the surface. It provides contrast in the connective tissue and, due to its intravenous administration and binding to serum albumin, contrast of the local microvasculature.

Disruption to the vasculature, or leaky blood vessels, results in an increase in the overall fluorescence signal which may be indicative of disease. Fluorescein helps to visualize pit patterns in the colon, surface epithelial cells, connective tissue within the lamina propria, blood vessels, and red blood cells [56]. Acriflavine hydrochloride, which is topically applied, is most commonly used in the stomach and colon. Acriflavine provides contrast between the nuclei and cytoplasm in the superficial epithelium for imaging of surface mucosa up to 100 μm. The combination of imaging modalities is common as information garnered with one modality may compliment another. However, it is desirable to limit the number of contrast agents needed for multi-modal imaging. Cresyl violet has proven to predict histology as a single topically applied contrast agent for *in vivo* confocal laser endomicroscopy and chromoendoscopy of the lower GI tract [57].

In addition to these non-specific contrast agents, targeted molecular specific contrast agents have recently been developed for potential use *in vivo* to target biomarkers associated with certain diseases, such as cancer. For example, tumors can express unique receptors at a high rate. By targeting these biomarkers with high affinity ligands, it is possible to locate areas where carcinogenesis, angiogenesis, or metastasis is taking place [58]. Both antibodies and peptides conjugated with exogenous dyes have been successfully used as specific binding contrast agents for optical imaging. Cyanine dyes conjugated to peptides have shown a three-fold increase in tumor contrast over normal tissue [59]. Fluorescent signal is enhanced at the plasma membrane of the cells with increased receptor expression. A study using a targeted heptapeptide for colonic dysplasia was performed *in vivo* on patients undergoing colonoscopy [60]. Confocal

microendoscopy of the colon using the Cellvizio system by Mauna Kea Technologies exhibits images showing significant contrast at borders between normal and dysplastic crypts, Fig 7. Areas with dysplastic colonocytes show a higher fluorescent signal due to peptide binding in contrast to normal colonocytes.

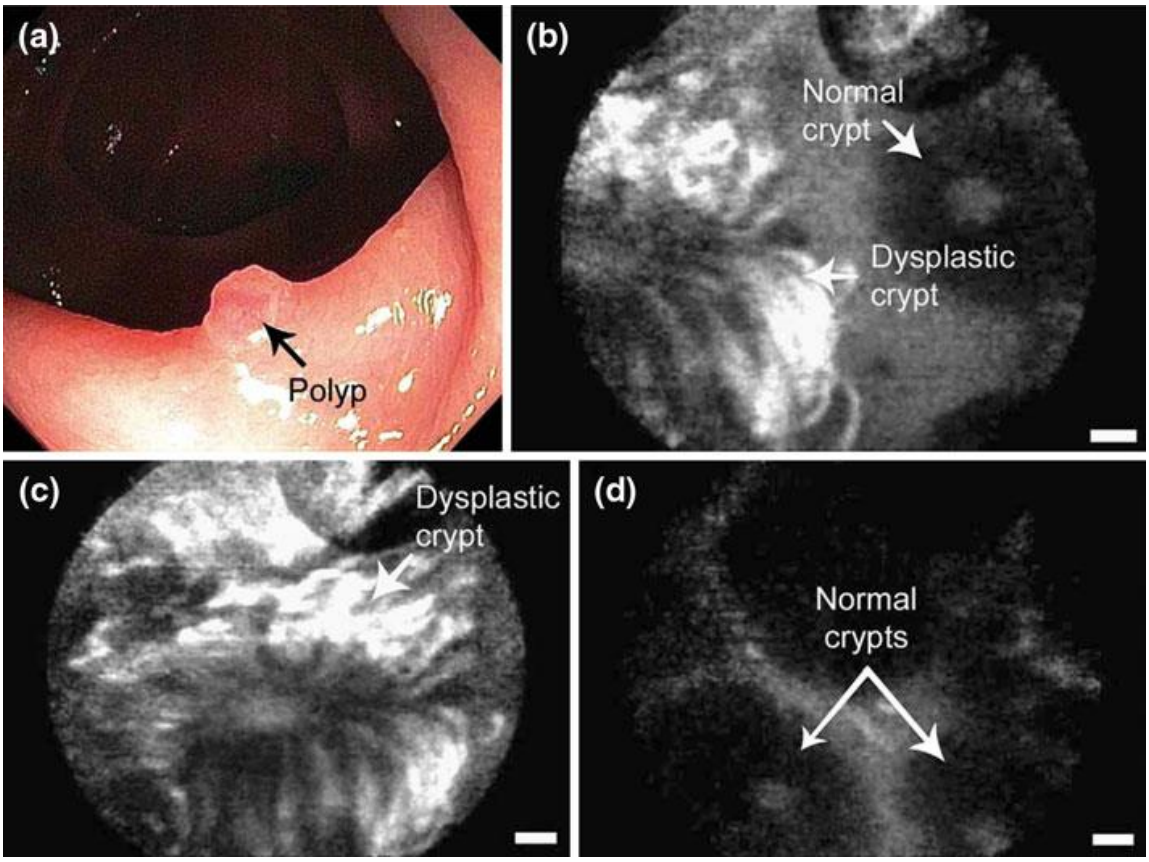

Fig 7. *In vivo* confocal fluorescence images of the border between colonic adenoma and normal mucosa, showing peptide binding to dysplastic colonocytes. (a) Endoscopic view, (b) border, (c) dysplastic crypt, and (d) adjacent mucosa. Scale bars: 20 μm [60].

Antibodies have been used to target the epidermal growth factor receptor (EGFR), a cell surface receptor that is over-expressed in many cancers. To aid early detection of oral neoplasia, oral biopsies were exposed to a monoclonal antibody specifically targeting EGFR [61]. Abundant fluorescence signal was noted throughout

abnormal mucosa. EGFR has also been targeted for imaging colorectal cancer in a mouse model [62]. Two different human colorectal cancer cell lines were grown as tumors in mice. Using the Optiscan instrument by Pentax, the colon tumors were imaged *in vivo* after an injection of fluorescently labeled EGFR antibodies. Tumors with human cell lines expressing high levels of EGFR showed a distinctly higher signal when compared to tumors expressing low levels of EGFR. By targeting EGFR with fluorescently labeled antibodies, it was possible to differentiate between two types of human colorectal cancer tumors. To show the potential for *in vivo* use in humans, a similar study was performed on excised human tissue and the results indicated that it was possible to differentiate neoplastic from non-neoplastic tissues.

2.3 Imaging Epithelial Tissues Using Confocal Microscopy

2.3.1 Mouse Colon

Fluorescence confocal microscopy reveals morphological changes in colonic tissue by utilizing fluorescent stains. Acridine orange (AO) is a nucleic stain that is excited at 488 nm and emits at 530 nm. Studies have shown that this fluorophore sufficiently stains the nuclei surrounding colon crypts [63]. Colon crypts appear as black holes in confocal images. In normal rat colon tissue, epithelial cells surrounding colon crypts are clearly resolved, but after 3 days of DSS treatment, morphological changes in the colon crypts are seen. The crypts exhibit a wider spacing and there is epithelial cell loss at the surface of the tissue. After 5 days of DSS treatment, there is a loss in fluorescent signal as the number of epithelial cells at the surface is further reduced. At day 7 of treatment, crypt distortion is noted along with the loss of colon crypts in some areas.

Additionally, fluorescence confocal microscopy has the potential to image biochemical changes in the tissue using endogenous fluorophores such as collagen, elastin, flavin adenine dinucleotide (FAD) and nicotinamide adenine dinucleotide (NADH) [64,65].

2.3.2 Porcine Buccal Mucosa

After applying 6% acetic acid for aceto-whitening of tissue, the nuclei appear much brighter in reflectance confocal imaging than autofluorescence imaging, and this method provides enough contrast for a quantitative study of features within epithelial tissue [66]. Studies have shown that reflectance confocal microscopy is capable of differentiating normal and dysplastic cervical tissue *ex vivo* [67]. A quantitative review was performed by determining the nuclear to cytoplasmic ratio and a qualitative study done using untrained observers to diagnosis the biopsies.

3. DESIGN, CONSTRUCTION, AND CHARACTERIZATION OF THE DUAL-MODE CONFOCAL MICROSCOPE*

3.1 Introduction

I designed and constructed a fluorescence and reflectance confocal microscope for imaging epithelial tissues for preclinical studies. In addition to working in two imaging modes, the system also scans in two modes producing extended images in one axis. Design requirements were selected based on the application for each imaging mode. Imaging the full epithelial layer is important because, if precancer is detected in an early stage, the chance of developing cancer can be greatly reduced. One of the tradeoffs for having better resolution is typically a smaller field of view. By custom designing a benchtop confocal microscope with a large field of view, more information about the interrogated tissue is acquired at a much faster speed without the need for post-processing techniques such as mosaicing.

3.2 System Design

3.2.1 Fluorescence Mode

Fig 8 shows a schematic of the constructed confocal fluorescence microscope, Fig 8(a), and a photo of the setup, Fig 8(b). The upright confocal microscope has a 40 mW, 488 nm, continuous wave, externally doubled diode laser (PC14717

* Part of this section is reprinted with permission from Imaging inflammation in mouse colon using a rapid stage-scanning confocal fluorescence microscope by Saldua, Meagan A., Cory A. Olsovsky, Evelyn S. Callaway, Robert S. Chapkin, and Kristen C. Maitland, 2012. Journal of Biomedical Optics, 17(1), 0160061-0160067, Copyright 2012 by SPIE.

Excelsior, Newport, Spectra-Physics, Santa Clara, CA) for fluorescence imaging. Power is controlled by passing the continuous wave laser through variable absorptive neutral density filters. This allows for varied incident power at the sample. The laser beam passes through a spatial filter, which also serves as a beam expander, and reflects off of a dichroic mirror (z488rdc, Chroma Technology Corporation, Rockingham, VT) to the fluorescence arm for imaging. A custom-designed polygon scanner (Lincoln Laser, Phoenix, AZ) with 14 facets, a scan angle of 24°, and a maximum speed of 37,500 rotations per minute (RPM). The polygon has a variable line scan rate of 2.34 to 8.75 kHz. The illumination source is imaged onto the galvanometer scanner (6220H M40B, Cambridge Technology, Inc., Bedford, MA) by a Keplerian telescope system with 75 mm effective focal length (EFL) (49-389, Edmund Optics, Barrington, NJ). The galvanometer scanner provides the frame scan for image acquisition in traditional raster scanning mode, has a scan rate up to 15 frames per second (fps), and produces "square" two dimensional images. The scanning mirrors are driven by a data acquisition (DAQ) board (NI PCI-6251, National Instruments, Austin, TX) controlled by LabVIEW software. A second Keplerian telescope system with 75 mm and 100 mm EFL (49-389, 49-390, Edmund Optics, Barrington, NJ) expands the beam to fill the back aperture of a 40×, 0.8 numerical aperture (NA), 3.5 mm working distance, water immersion microscope objective lens (MRD07420, Nikon). The sample is positioned on an XYZ motorized stage with 0.05 micron resolution, 100 mm of travel in any axis, and 7 mm/sec maximum speed (KT-LSM100A, Zaber Technologies Inc, Vancouver, British Columbia, Canada). Fluorescence is excited in the sample, collected by the objective, passed back through the telescope system, and descanned by the scanning

mirrors. A long pass filter (FF662-FDi01-25x36, Semrock) deflects the fluorescence signal to its own detection arm. A removable emission filter (HHQ495LP, Chroma Technology Corporation, Rockingham, VT) is placed after the dichroic to prevent any unwanted laser light from reaching the detector. The signal is focused onto the confocal detection pinhole using a lens with 50 mm EFL (NT49-792, Edmund Optics, Barrington, NJ) and then refocused onto a photomultiplier tube (PMT) detector (H9433-03MOD, Hamamatsu, Bridgewater, NJ) with another lens with 50 mm EFL (NT49-792, Edmund Optics, Barrington, NJ).

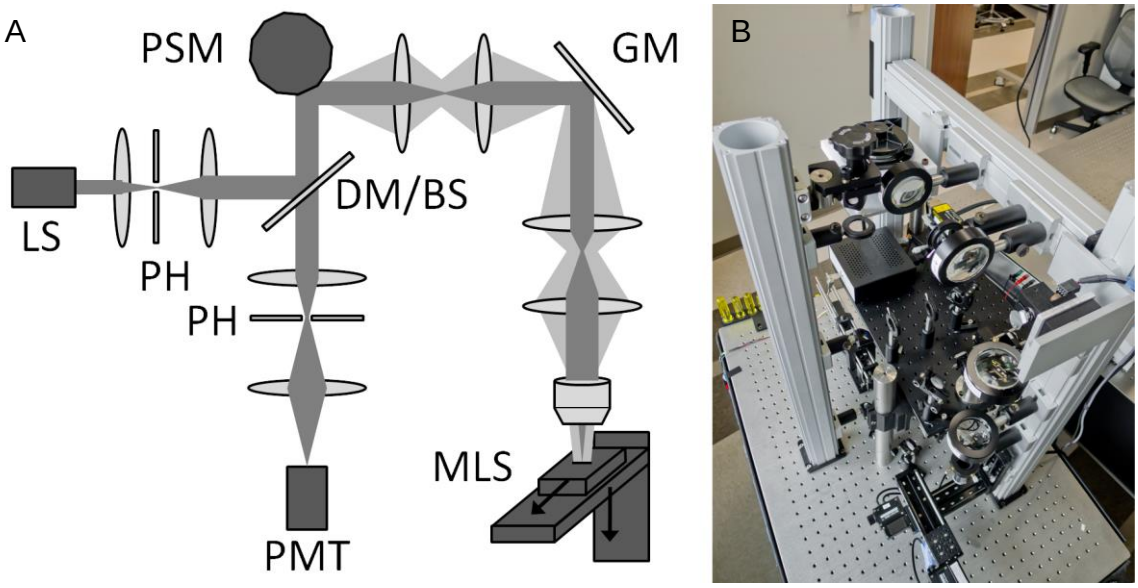

Fig 8. Confocal fluorescence and reflectance microscope system. (A) Schematic and (B) photograph of the system. LS: laser source, PH: pinhole, DM: dichroic mirror, BS: beam splitter, PSM: polygon scanning mirror, GM: galvanometer scanning mirror, MLS: motorized linear stage, PMT: photomultiplier tube.

A group of detector pinholes with varying diameters were selected from Thorlabs: 5, 10, 15, 25, 50, and 100 μm. To maximize signal throughput and maintain

sufficient axial sectioning, the size of the detection pinhole was selected to be approximately equal to the projected Airy disk, 10 μm for fluorescence confocal microscopy imaging. The intensity distribution as a function of normalized radial optical coordinate, v, for a single fluorescent point object in focus is given by

$$\mathrm{I}(v) = \left\{ 4\left[\frac{J_1(v)}{v} \cdot \frac{J_1(v/\beta)}{v/\beta} \right] \right\}^2, \tag{5}$$

where J_1 is a first order Bessel function of the first kind and β is the ratio of the emission wavelength to excitation wavelength [68]. The first minimum of the lateral response in Equation 5 occurs at $v_o = 3.83$. Using Equation 6,

$$d = \frac{v_o}{\pi} \lambda \frac{M_T}{NA_{obj}}, \tag{6}$$

the diameter of the projected central disk can be calculated to be 9.9 μm for our system with excitation wavelength $\lambda = 488$ nm, total system magnification $M_T = 13.33$, and objective lens numerical aperture $NA_{obj} = 0.8$. Therefore, a 10 μm diameter pinhole was used in the confocal detection spatial filter, corresponding to a normalized pinhole radius $v_p = 3.86$, from Equation 3. The theoretical lateral resolution as defined by the Rayleigh criterion can be calculated by converting the normalized pinhole radius to real radial distance in the object, r = 0.4 μm. To evaluate the optical sectioning capability, we use the plot of the half width, $u_{1/2}$, of the axial response of a planar fluorescent object translated through the focus as a function of v_p and β [68]. For $v_p = 3.86$ and $\beta = 1.08$, the normalized half-width of the axial point spread function is $u_{1/2} = 5.6$. Converting to the half width half maximum in spatial dimensions using

$$z_{1/2} = u_{1/2} \frac{\lambda}{2\pi} \cdot \frac{n}{NA^2}, \tag{7}$$

yields a full width half maximum (FWHM) axial resolution of 1.8 μm.

The scanning microscope can be operated in two modes: raster-scanning or stage-scanning. In either mode, the polygon scanner provides the fast axis scan, or line scan, at a scan rate of 8.33 kHz. In raster-scanning mode, the slow axis scan, or frame scan, is provided by the galvanometer scanning mirror, generating 1×1 mm^2 FOV images at 8 frames per second.

To increase FOV and data acquisition speed, lateral resolution is sacrificed by under-sampling with a 1 μm pixel size, which is significantly larger than the 0.4 μm theoretical lateral resolution. The system lateral resolution was measured by capturing an image of a reflective Ronchi grating (Edmund Optics) with 40 line pairs/mm. A line profile was plotted across several grating edges. The distance between the 10% and 90% intensity values was recorded for five edges and then averaged. The measured lateral resolution is approximately 1 μm. To measure axial resolution, a reflective silver mirror was translated through the focal plane. Intensity values were recorded from the PMT and plotted. The measured full width half maximum axial resolution is less than 2 μm. Table 1 summarizes the imaging parameters for the fluorescence confocal microscope system in raster-scanning and stage-scanning modes.

3.2.2 Reflectance Mode

Similar to the fluorescence confocal microscope setup, Fig 8, the reflectance mode differs in the wavelength of the laser source, the requirement of a beam

splitter and half-wave plate combination, and a pinhole lens with a larger focal length. When imaging in reflectance mode, resolution is sacrificed for penetration depth due to the longer NIR wavelength. A 120 mW, 811 nm (DL808-120-O, CrystaLaser, Reno, NV) diode-pumped solid state laser was used for reflectance imaging. The laser beam passes through a spatial filter as and is expanded. A polarizing beam splitter (PBS252, Thorlabs, Newton, NJ) and half-wave plate (AHWP05M-980, Thorlabs, Newton, NJ) efficiently reflect the polarized 811 nm laser source to the scanning arm for reflectance imaging. To make up for this loss in resolution, a 60× 1 NA water immersion microscope objective (LUMPLFLN 60XW, Olympus) with 2 mm working distance is used to focus the beam on the sample. A faster stage with 29 mm/sec maximum speed replaced the stage in the third axis (KT-LSM100B, Zaber Technologies Inc, Vancouver, British Columbia, Canada). The reflectance signal is collected by the water immersion objective, passed back through the telescope system, and then descanned by the scanning mirror combination. A 25 μm pinhole diameter was selected for optical resolution and signal throughput by matching it to the size of the projected Airy disk. The diffraction limited spot size, D, was calculated from Equation 8 to be 27 μm,

$$D = \frac{\lambda \cdot f}{r} \tag{8}$$

where λ is wavelength, f is the focal length of the pinhole lens, and r is the radius of the illumination beam at the back aperture of the microscope objective. Placing a 75 mm rather than 35 mm lens in front of the PMT as the pinhole lens produces an increased system magnification, M_T = 33.33. A higher system magnification decreases the normalized pinhole radius value and also improves the theoretical lateral and axial resolutions to

account for the higher wavelength source. Using Equation 3, the normalized pinhole radius is $v_p = 2.91$, corresponding to a theoretical lateral resolution of r = 0.4 μm from Equation 9,

$$r = \frac{v_p}{2\pi} \cdot \frac{\lambda}{NA_{obj}} \tag{9}$$

where v_p is the normalized pinhole radius, λ is the illumination wavelength, and NA_{obj} is the numerical aperture of the microscope objective. The theoretical axial resolution, or FWHM, calculated from Equation 7 is 1.3 μm.

3.3 Image Formation

3.3.1 Raster Scanning

To form a 2D image using a point-scanning confocal microscope, the beam must be scanned in two dimensions using scanning mirrors. Both of the scanning mirrors and the stage are controlled by LabVIEW software (National Instruments), and the mirrors are driven by a data acquisition (DAQ) board (NI PCI-6251, National Instruments). The PMT detector records a voltage signal from each point which is assigned to a certain intensity value. The gain was set to 10^4 and frequency bandwidth of 10 MHz. A framegrabber (NI PCI 1410, National Instruments, Austin, TX) digitizes the voltage signal with a 29 MHz pixel and a collection of these points creates a 2D image of the focal plane within the sample so that it may be displayed on a computer monitor in near-real time.

The framegrabber requires three inputs: the signal from the PMT, a horizontal synchronization (HSYNC) input, and a vertical synchronization (VSYNC) input. The HSYNC and VSYNC are synchronization signals that correspond to the

polygon and galvanometer scanning mirror positions. The synchronization signals are generated in LabVIEW using counter signals.

3.3.2 Stage Scanning

Confocal mosaicing has recently been used to acquire a large field of view image by capturing individual small field images using scanning mirrors, stepping the sample using a translation stage to scan a larger area, and post-processing the images to reconstruct the large field image [69]. With advancing technology, motorized stages are able to move at faster speeds with high precision and accuracy. A faster way of acquiring an extended image is to use the motorized stage as the frame scan instead of the galvanometer scanning mirror. Combining this imaging method with an automated program to acquire multiple images will help achieve reconstruction of the entire mouse colon much faster than current methods as well as provide a high resolution confocal image with an extended wide-field of view. Images longer than 2 cm can be acquired, but are currently limited by our framegrabber.

In the custom confocal microscope system setup, the sample is positioned on an XYZ motorized stage (KT-LSM100A, Zaber Technologies Inc., Vancouver, British Columbia, Canada) with 0.05 μm resolution, 100 mm of travel in each axis, and 7 mm/sec maximum speed. The galvanometer scanning mirror is positioned in the center of its scan range (center of FOV), and the motorized linear stage translates the sample in the second axis. The image acquisition speed, FOV, and digital image size, are limited by the stage speed, stage travel range, and frame grabber memory, respectively. Acquisition of a single 60 megapixel image of 1×60 mm^2 FOV takes approximately 10 sec. Acquisition of a stack

of 60 frames with a 1×60 mm^2 FOV and a 10 μm axial step interval between consecutive images over an axial range of 600 μm takes approximately 20 min. The 600 μm axial range was necessary to capture the topography of the sample and to accommodate a minor incline of the translation stage over the 100 mm of travel. The XYZ motorized translation stage has three independently mounted axes; re-positioning the stage may reduce the required axial range and, consequently, increase the three dimensional image acquisition rate.

3.4 Measured Performance

A United States Air Force (AF) resolution target and Ronchi grating with 40 line pairs per mm were imaged in both fluorescence and reflectance mode using 488 nm and 811 nm wavelengths, respectively. Fig 9 and Fig 10 below show the resulting images. The fluorescent AF target can be seen in Fig 9(A) and the reflective AF target in Fig 10(A). The reflective Ronchi grating is shown in Fig 9(B) and Fig 10(B), where the signal in Fig 9(B) is from leakage through the dichroic mirror. The system and imaging theoretical and measured parameters for the dual-mode fluorescence and reflectance confocal microscope are shown in Table 1.

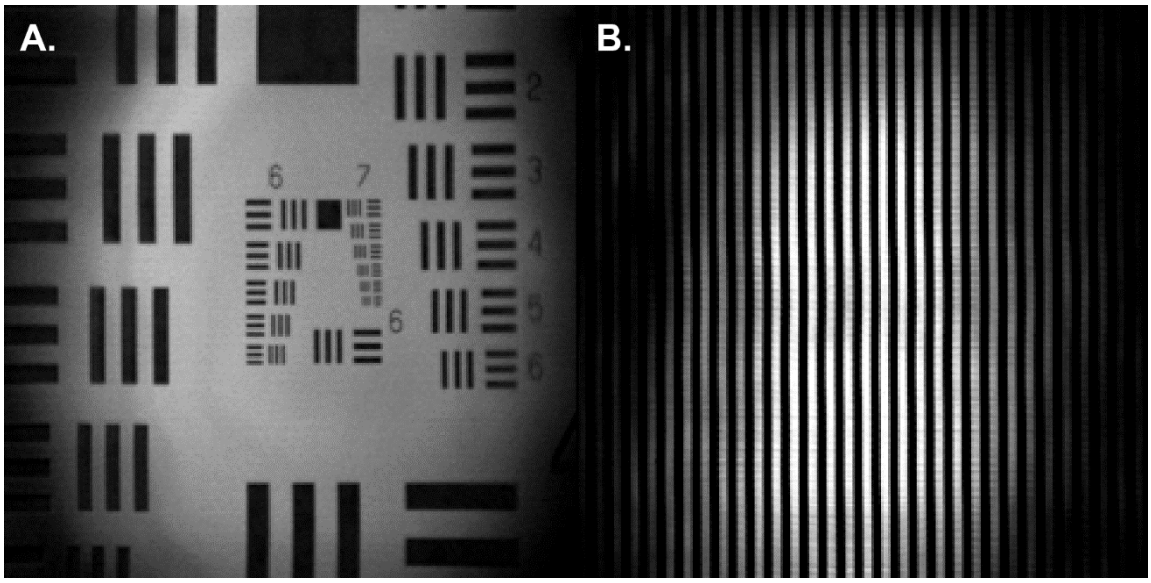

Fig 9. Lateral resolution and field of view at 488 nm. (A) Fluorescent AF target and (B) Reflective Ronchi grating.

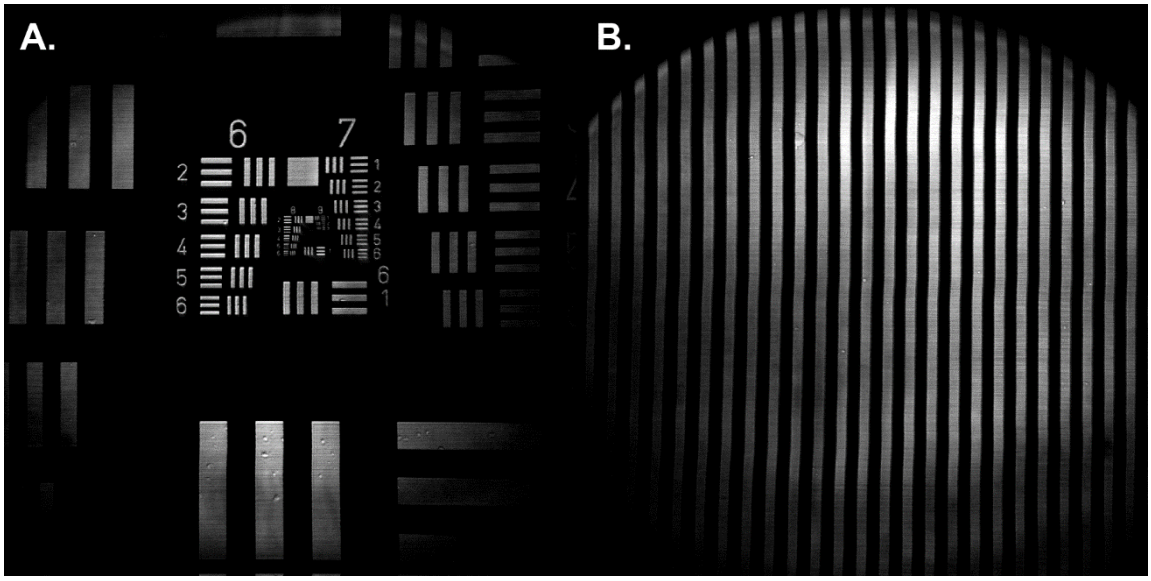

Fig 10. Lateral resolution and field of view at 811 nm. (A) Reflective AF target and (B) Reflective Ronchi grating.

Fig 11 below shows the capability of image size with a FOV of 1 mm × 60 mm in stage-scanning mode. The object imaged is a reflective Ronchi grating with 40 line pairs per mm. The yellow box shows a zoomed in section, see in Fig 12.

Fig 11. Extended field of view, 1 mm × 60 mm.

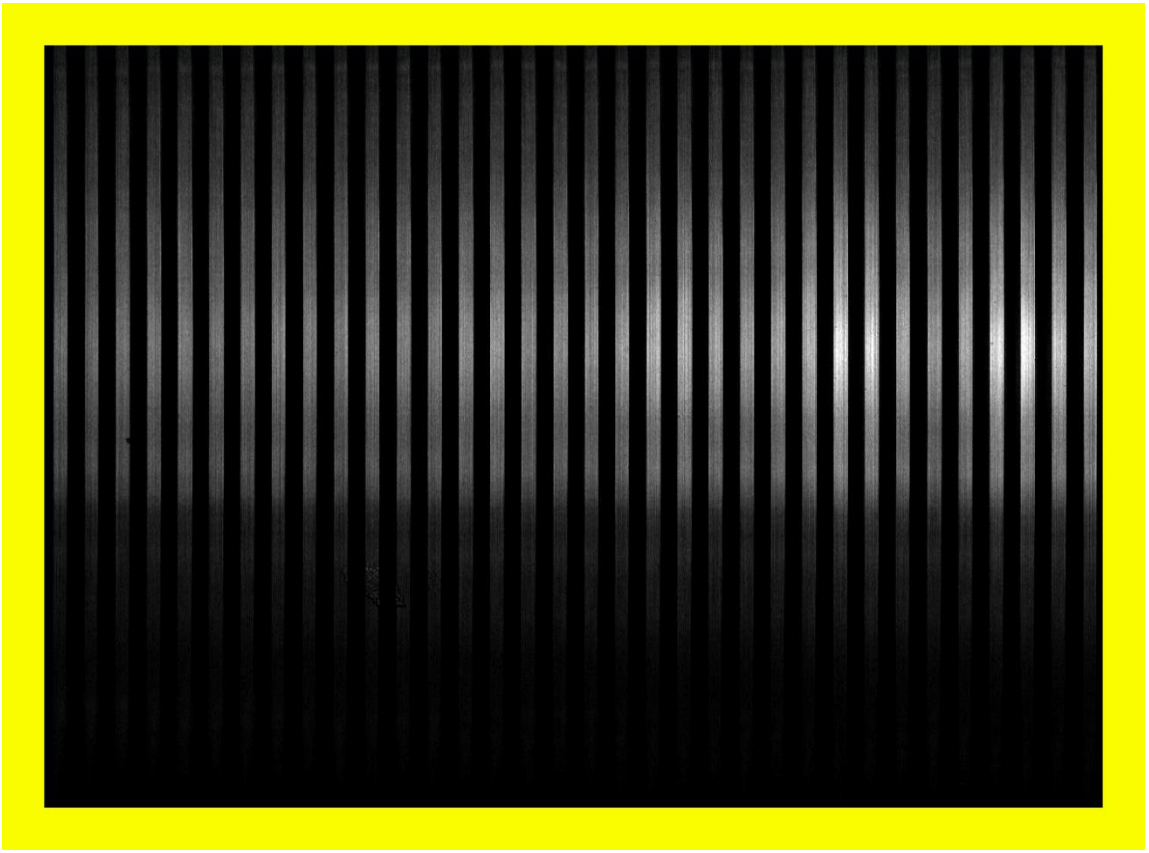

Fig 12. Cropped section of Ronchi grating from Fig 10. The Ronchi grating has 40 line pairs per mm.

3.5 Comparison to Commercial System

The custom dual-mode fluorescence and reflectance confocal microscope is compared to the commercial Caliber Imaging and Diagnostics, Inc. VivaScope2500 in Table 1 below.

Table 1. Custom and commercial confocal system comparison.

	Custom				**Commercial**	
Mode	**Fluorescence**		**Reflectance**		**Fluorescence**	**Reflectance**
Illumination wavelength	488 nm		811 nm		488, 658 nm	830 nm
	Theoretical	**Measured**	**Theoretical**	**Measured**	**Measured**	
Lateral resolution	0.4 µm	1 µm	0.3 µm	1 µm	< 2 µm	
Axial resolution	1.8 µm	2 µm	1.8 µm	2 µm	< 5 µm	
Line scan speed	2.34 – 8.75 kHz				N/A	
	Raster-scanning mode					
	Fluorescence		**Reflectance**		**Measured**	
Field of view	1 mm × 1 mm		750 × 750 µm		750 × 750 µm	
Frame scan speed	3 - 15 frames per second				9 frames per second	
	Stage-scanning mode					
	Fluorescence		**Reflectance**			
Field of view	1 mm × ≤ 60 mm		750 µm × ≤ 60 mm		N/A	
Frame scan speed	2.3 – 7 mm/sec				N/A	

4. IMAGING INFLAMMATION IN MOUSE COLON USING A RAPID STAGE-SCANNING CONFOCAL FLUORESCENCE MICROSCOPE*

4.1 Introduction

Large area confocal microscopy may provide fast, high resolution image acquisition for evaluation of tissue in preclinical studies with reduced tissue processing in comparison to histology. We present a rapid beam and stage scanning confocal fluorescence microscope to image cellular and tissue features along the length of the entire excised mouse colon. The beam is scanned at 8,333 lines/sec by a polygon scanning mirror while the specimen is scanned in the orthogonal axis by a motorized translation stage with a maximum speed of 7 mm/sec. A single 1×60 mm^2 field of view image spanning the length of the mouse colon is acquired in 10 seconds. Z-projection images generated from axial image stacks allow high resolution imaging of the surface of non-flat specimens. In contrast to the uniform size, shape, and distribution of colon crypts in confocal images of normal colon, confocal images of chronic bowel inflammation exhibit heterogeneous tissue structure with localized severe crypt distortion.

4.1.1 Bowel Inflammation

Autoimmune and chronic inflammatory diseases are a global health problem. With respect to the burden of inflammatory bowel diseases (IBD), approximately

---

* Reprinted with permission from Imaging inflammation in mouse colon using a rapid stage-scanning confocal fluorescence microscope by Saldua, Meagan A., Cory A. Olsovsky, Evelyn S. Callaway, Robert S. Chapkin, and Kristen C. Maitland, 2012. Journal of Biomedical Optics, 17(1), 0160061-0160067, Copyright 2012 by SPIE.

1.5 million Americans exhibit chronic debilitating inflammatory conditions of the intestinal tract, leading to distressing symptoms and an impaired quality of life (estimated annual cost exceeding $2 billion) [70]. Patients experiencing IBD often report symptoms such as abdominal pain, diarrhea, rectal bleeding, weight loss, fever, and fatigue. Ulcerative colitis and Crohn's disease are two distinct forms of IBD [71]. In ulcerative colitis, inflammation is typically restricted to the mucosa in the colon. In Crohn's disease, any area within the entire gastrointestinal tract may be susceptible to inflammation.

One in 19 Americans are at risk of developing colorectal cancer in their lifetime. Detection and removal of precancerous polyps has reduced the incidence and mortality of this disease [72]. Patients with IBD have an increased risk for developing colorectal cancer; after seven years of inflammation, the risk of developing cancer increases by 0.5-1% every year [73]. Although studies have shown this direct relationship between inflammation and colon cancer, early cancer detection remains a challenge, even for this high risk population [74]. Currently, high risk patients are recommended to begin colonoscopy cancer screening at an earlier age than healthy adults [75].

Epidemiologic studies have shown that diet is also a major risk factor for colorectal cancer [72]. For example, high consumption of red or processed meats increases the risk of colorectal cancer by 28% and 20%, respectively [72,76]. Recent studies indicate that bioactive food components containing n-3 polyunsaturated fatty acids (PUFA) may have antitumorigenic effects by reducing inflammation in an animal model of colitis-associated cancer [77,78]. Data has revealed a "protective effect" of n-3 PUFA (fish oil) on colon cancer and in contrast, n-6 PUFA (vegetable oil) has been shown to amplify the

formation of colon tumors. This may suggest that IBD patients could moderate cancer development by modifying their diet [79].

Colon crypt and tissue structural changes in preclinical studies are typically characterized using histopathology. Histology provides images of cellular and tissue structure after animal sacrifice, colon removal, washing and staining of the tissue. This is a time sensitive process that can introduce artifacts during tissue preparation. In histological images of normal colon tissue, the cylindrical crypt openings are aligned parallel to one another and exhibit a uniform hexagonal pattern when observed from an en face view [80]. This pattern is characteristic of normal colonic tissue with only slight variation in colon size and arrangement. Inflamed tissue varies in morphological structure compared to normal colon tissue. Crypt structure may be lost and tissue architecture is replaced by a disordered crypt arrangement with heterogeneous crypt size and shape, which can be seen both in histology and confocal endomicroscopy [81,82]. Due to the heterogeneity of inflamed tissue, examination of a small tissue sample by histology may not be indicative of the most severe disease state elsewhere in the colon. The 'Swiss roll' technique may be used to visualize histological features along the length of the colon, but provides only a thin section through the tissue [83]. With transition from inflammation to neoplasia, dysplasia or cancer can affect any part of the colon, with various magnitudes at different locations, complicating localization and characterization of disease by histopathology in preclinical studies [74].

Rapid imaging of bulk tissue along the length of freshly excised colon could provide sufficient information on crypt structure throughout the colon to

characterize tissue in preclinical studies. Reduced tissue processing, fast image acquisition, and evaluation over a larger field could increase throughput and quantification in preclinical studies of IBD. Our custom-designed confocal microscope can achieve a single 1×60 mm^2 field of view image in 10 seconds. Compared to other confocal imaging systems, this system is capable of producing large area images in a short period of time. Here, we present stage scanning confocal microscopy as a technique to rapidly image the length of the colon with minimal tissue processing.

4.1.2 Confocal Microscopy

Confocal microscopy can provide high resolution images of bulk tissue with minimal tissue processing and fast image acquisition. In contrast to the physical sectioning and two dimensional imaging of traditional histology, confocal imaging allows "optical sectioning" of bulk tissue, enabling acquisition of three dimensional images of intact tissue [3,84]. This technique has been translated to the clinical setting where *in vivo* confocal microendoscopy is currently being explored for guiding biopsy in the gastrointestinal tract [85]. However, even with mosaicing to expand the imaging field, FOV still remains limited.

The high resolution of confocal microscopy is achieved by placing a pinhole in front of the detector in a conjugate image plane of the focal spot in the sample. Out of focus light is significantly rejected by the pinhole. Two and three dimensional images can be generated by scanning the beam or the sample [86-88]. Although, historically, stage-scanning has been used quite extensively, [89] the speed of translation stages has limited the speed of image acquisition. Modern confocal microscopes typically

use some form of beam-scanning to maximize image acquisition speed, [90] but the FOV is typically limited to less than 500×500 μm^2 [22]. A larger FOV can be achieved by stitching images together using a mosaicing technique [91].

FOV and image acquisition speed can be increased by combining beam and stage scanning. Recently, beam and stage scanning used with mosaicing has been implemented to increase acquisition speed of large FOV reflectance confocal images for dermatological applications [6]. A 10×10 mm^2 strip mosaic was acquired in three minutes. Similarly, spectral encoding in one axis to scan 180 μm and stage scanning in both lateral axes with mosaicing has been used to image large esophageal biopsy specimens [92]. Axial scanning of the objective lens using a piezoelectric transducer allowed three dimensional images over a 120 to 150 μm depth range. Fields of view ranging from 2×1 mm^2 to 5×3.6 mm^2 were acquired in 2.5 to 15 minutes. Large FOV fluorescence confocal imaging of the mouse colon and other organs *in vivo* through a gradient index (GRIN) side-viewing microprobe was recently achieved by versatile multidimensional scanning [93]. The 250×250 μm^2 raster-scanned FOV is extended by mosaicing frames captured at 30 frames per second while rotationally scanning the microprobe and/or translating the sample or animal to scan along the length of a lumen. The focal depth position in the sample is adjusted by altering the focal position at the proximal face of the GRIN relay lens. 60,000 frames acquired in over 30 minutes from a 12 mm length of mouse colon after intravenous injection of fluorescent dye are reconstructed into beautiful images of the vasculature in two and three dimensions and with multiple scales.

We exploit a polygon mirror beam scanner and a fast motorized translation stage to rapidly acquire confocal images with an extended FOV in one axis. We have acquired a single high aspect ratio 60 megapixel 1×60 mm^2 image in 10 seconds, extending image size in one axis and increasing acquisition speed over previously reported systems. Translation of the sample in the third dimension allows three dimensional imaging and two dimensional projections of tissue to accommodate specimens with an uneven surface. This high aspect ratio imaging is ideal for imaging tissue structure along the gastrointestinal tract. We present the use of combined beam and stage scanning in confocal microscopy to extend the FOV to image and evaluate freshly excised mouse colon to provide qualitative information on crypt structure along the length of the colon.

4.2 Materials and Methods

4.2.1 System Design

The fluorescence confocal microscopy system setup is described in detail in the previous chapter and shown in Fig 8. The measured lateral resolution is 1 μm. For this application, imaging tissue and crypt structure in the mouse colon, lateral resolution is less important than the field of view, speed of image acquisition, and file size. We can resolve 2 μm according to the Nyquist Theorem, therefore, the sampling is sufficient to resolve individual cell nuclei, which are approximately 5 to 10 μm in diameter, and crypt lumen, ranging from 40 to 70 μm in diameter in normal mouse colon tissue. Table 2 summarizes the imaging parameters for the confocal fluorescence microscope system in raster-scanning and stage-scanning modes.

Table 2. System and imaging parameters.

System/Imaging parameters	
Excitation wavelength	488 nm
Detection wavelength	>495 nm
Lateral resolution	1 μm
Axial resolution	2 μm
Line scan speed	8333 lines/sec
Raster-scanning mode	
Field of view	1 mm × 1 mm
Frame scan speed	8 frames/sec
Stage-scanning mode	
Field of view	1 mm × ≤ 60 mm
Frame scan speed	7 mm/sec

4.2.2 Sample Preparation and Imaging

Human colitis can be modeled in healthy rodents by treatment with dextran sulfate sodium (DSS) added to their drinking water [94]. An increase in disease duration results in an increased rate of neoplastic development. When used in conjunction with azoxymethane (a colon-specific carcinogen), the mice can develop colon cancer [95].

Black C57BL/6 mice were used for this study. The animal protocol was reviewed and approved by the Texas A&M University Institutional Animal Care and Use Committee. To induce chronic inflammation, a mouse was treated with 2.5% DSS (MP Biomedicals) for five days followed by a 17 day recovery period. On day 22, the treatment

and recovery periods were repeated. Finally, the mouse was treated with 2% DSS for four days. Termination occurred on day 57.

Following colon resection, the normal and inflamed mouse colons were opened longitudinally along a fatty tissue line. The tissue was rinsed in two phosphate buffered solution (PBS) washes to remove any fecal matter. The colons were stained with 1 mg/mL of acridine orange (Sigma-Aldrich) for two minutes and then rinsed in PBS for one minute. Each mouse colon was placed flat in a Petri dish with the inside of the colon facing up. A microscope slide was placed on top of the colon to flatten and immobilize the tissue during imaging.

When imaging a mouse colon, the tissue is positioned in the focal plane of the microscope using raster-scanning mode. In order to evaluate tissue features along the length of the colon, extended FOV confocal images are acquired using stage-scanning mode. The long axis of the FOV is specified based on the length of the mouse colon. The topography of a mouse colon varies along its length; therefore it was necessary to acquire vertical stacks of extended confocal images to capture information at different focal planes. The number of images in a stack or the depth of imaging is determined by the topography and the penetration of light into the tissue. The long stacks were used to build a Z-projection image that reconstructs the surface profile of the mouse colon tissue while maintaining high resolution features. For the images presented in this paper, 70 extended confocal images, approximately 1×56 mm^2, of normal mouse colon tissue and 50 images, approximately 1×60 mm^2, of chronic inflamed colon were acquired with a 10 µm step interval between consecutive frames in the axial direction.

Following confocal imaging, tissue samples from proximal, middle, and distal regions of the colon were prepared for histological processing. In contrast to the standard transverse slicing, the tissue was oriented to generate tissue slices parallel to the surface of the tissue to enable a comparison to the en face confocal images. The tissue sections were stained with hematoxylin and eosin (H&E).

4.2.3 Image Analysis

Images stacks were processed into two dimensional projections and videos using Photoshop (Adobe Systems Inc., San Jose, CA) and ImageJ (National Institutes of Health, http://rsbweb.nih.gov/ij). Each image stack was reduced to a two dimensional maximum intensity Z-projection image. The maximum intensity projection command in ImageJ selects the maximum pixel value for a single pixel location within a stack of images and generates an image using the maximum values for all pixel locations. Because the colon tissue topography varies significantly within this large field of view and confocal sectioning yields a thin optical slice through the tissue, the Z-projection allows visualization of the colon crypts near the surface along the length of the colon. It was determined that the image quality of Z-projections was improved by using every other image in the stack, resulting in 20 μm axial separation between images in the stack. Fig 13 demonstrates the maximum intensity Z-projection and three dimensional reconstruction for a stack of confocal images. Fig 13a – 13d shows four confocal images of a 1×2 mm^2 region separated by 20 μm in depth taken from the image stack. Fig 13(e) is a zoomed-in section depicted by the white box in Fig 13(a) exhibiting bright nuclei surrounding colon crypts. The corresponding maximum intensity Z-projection is shown

in Fig 13(f) to demonstrate the effect of the projection image, and the three dimensional reconstruction is shown in Fig 13(g) for comparison. Due to tissue absorption and scattering, the maximum imaging depth in colon tissue stained with acridine orange is approximately 60 μm.

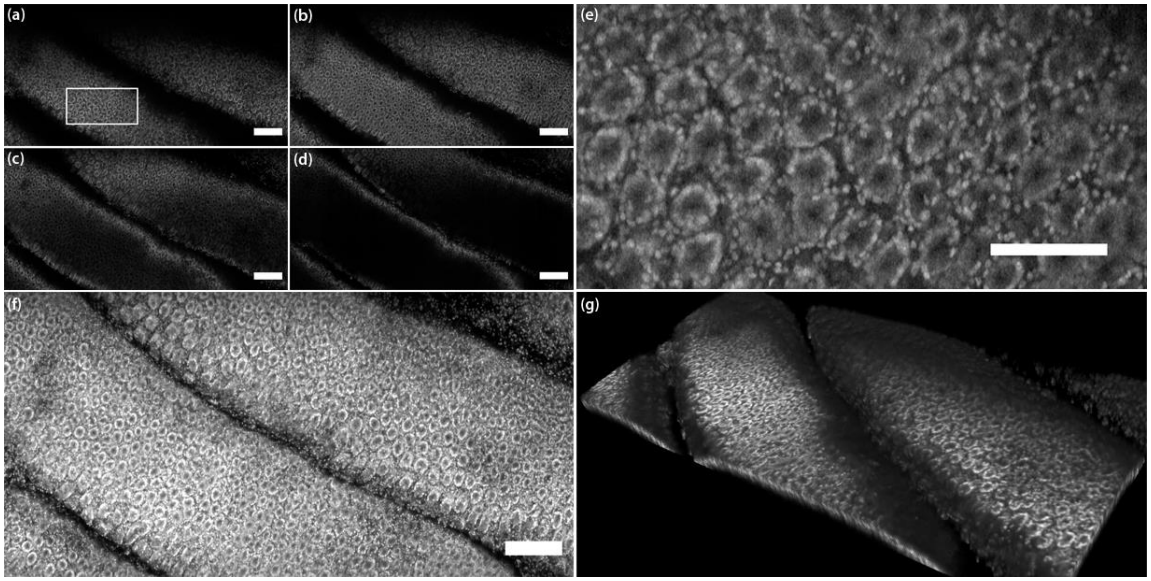

Fig 13. Selected confocal frames from an image stack for a single region, 1 × 2mm^2 field of view. (a) Near the surface and (b) 20 μm, (c) 40 μm, and (d) 60 μm deep. (e) Zoomed-in section of (a) denoted by white box. (f) 2D maximum intensity Z-projection of the entire image stack with 20 μm between successive frames. (g) 3D reconstruction of image stack. Scale bars: (a)–(d), (f) 200 μm, (e) 100 μm.

Images were cropped to 1×42 mm^2 to more easily visualize tissue features along the length of the colons, and 1×2 mm^2 regions were selected and cropped to zoom in on the diverse crypt features in the colon tissue. Additionally, the images were resized to correct for non-square pixels. While the vertical pixel size is 1 μm, the horizontal pixel size is 0.78 μm when the stage is scanning at maximum speed. The images were skewed

to achieve 1 μm^2 pixel size. The image contrast was enhanced and normalized for improved print viewing. To better illustrate the size of the extended FOV images and for comparison of crypt features in normal and inflamed colons, the Z-projection images of normal and inflamed tissue were combined in a video file (S1 Video). Adobe Premiere Pro CS5 software was used to generate the video.

4.3 Results

Fig 14(a) shows 1×42 mm^2 of a Z-projection extended FOV image of normal mouse colon. The image is oriented with the proximal end, or ascending colon, to the left and the distal end, or sigmoid colon, to the right. Sample regions of interest from the length of the colon were selected, cropped to 1×2 mm^2, and enlarged to more clearly show cellular and crypt features in the image. These regions are depicted by white rectangles in Fig 14(a). Fig 14(b) and Fig 14(c) are cropped regions of Fig 14(a) from the proximal region of the mouse colon. Fig 14(d) is a 5× microscope image of a histology slide prepared from a section of tissue at the proximal end of the colon. In the histological process, the tissue was oriented parallel to the mucosal surface such that the histology image would emulate the en face confocal image, to provide a direct comparison to confocal images. Similarly, confocal and histology images are shown for middle, Fig 14e – 14g, and distal, Fig 14h – 14j, regions of the colon. The 1×2 mm^2 confocal images and the 1×1.8 mm^2 histology images are shown on the same scale to enable comparison of crypt features. The extended FOV confocal image, Fig 14(a) is 1000×42,000 pixels. Fig 14(b), 14(c), 14(e), 14(f), 14(h), and 14(i) are 1,000×2,000 pixels.

The crypts shown in the confocal images of normal colon are uniform in size and distribution along the length of the colon, Fig 14(b), 14(c), 14(e), 14(f), 14(h), and 14(i). The lumen size within the histology images, Fig 14(d), 14(g), and 14(j), correlate with the confocal images and confirm the homogeneity of the colon. There is not a significant change in lumen size, shape, or distribution along the mouse colon tissue surface.

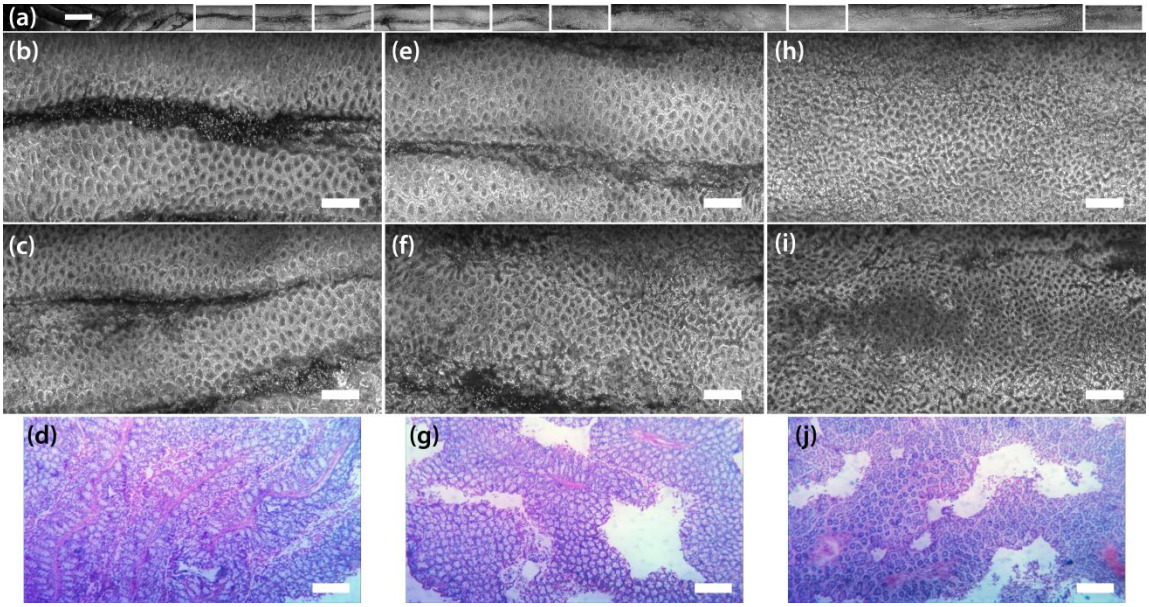

Fig 14. Extended confocal microscopy and histology images of normal mouse colon. (a) 1 × 42 mm^2 Z-projection (S1 Video, MPG4, 7.42 MB). Proximal side of colon is on the left. Scale bar: 1 mm. Fig 14(b), 14(c), 14(e), 14(f), 14(h), and 14(i) are sequential regions, 1 × 2 mm^2, of (a) designated by white boxes, from proximal [(b) and (c)], middle [(e) and (f)], and distal [(h) and (i)] regions. Scale bars: 200 μm. Fig 14(d), 14(g), and 14(j) are histology images, 1 × 1.8 mm^2, from proximal, middle, and distal regions, respectively. Scale bar: 200 μm.

Fig 15(a) is a 1×42 mm^2 section of a Z-projection extended FOV image of chronic inflammation in the mouse colon. The white rectangles indicate the positions of Fig 15(b) and Fig 15(c) in the proximal region, Fig 15(e) and Fig 15 (f) in the middle region, and Fig 15(h) and Fig 15 (i) in the distal region, moving left to right in the image. Fig 15(d), Fig 15(g), and Fig 15(j) are the corresponding en face histology images from the proximal, middle, and distal regions, respectively. The 1×2 mm^2 image locations were selected to highlight the diversity of tissue structure along the length of the inflamed colon.

In some areas within the confocal images of inflamed colon, the crypts appear uniform in size and shape, for example in Fig 15(b), Fig 15(c), and parts of Fig 15(f). While in other locations, such as Fig 15(e), parts of Fig 15(f), Fig 15(h), and Fig 15(i), the crypts are spaced further apart or exhibit large lumen that are not circular in shape. As compared to the normal mouse colon, the inflamed tissue has a loss of architecture with non-uniform crypts that are not evenly distributed across the tissue surface. The histology images of the mouse colon tissue with chronic inflammation show heterogeneity of the tissue as the lumen size varies from one location to another, Fig 15(d), Fig 15(g), and Fig 15(j).

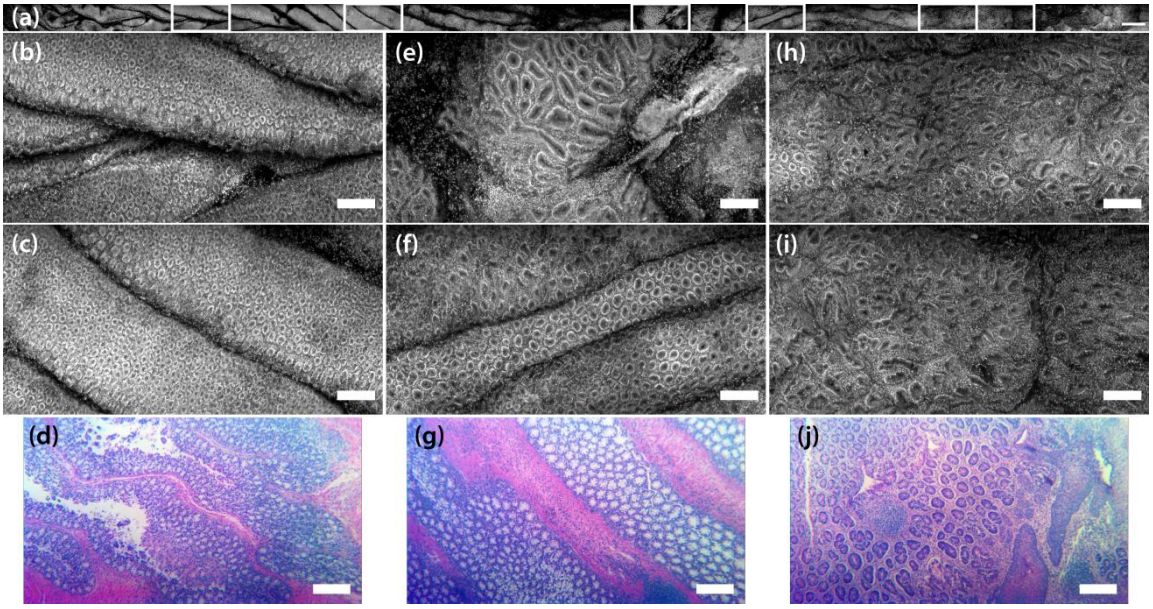

Fig 15. Extended confocal microscopy and histology images of mouse colon with chronic inflammation. (a) 1 × 42 mm^2 Z-projection (S1 Video, MPG4, 7.42 MB). Proximal side of colon is on the left. Scale bar: 1 mm. Fig 15(b), 15(c), 15(e), 15(f), 15(h), and 15(i) are sequential regions, 1 × 2 mm^2, of (a) designated by white boxes from proximal [(b) and (c)], middle [(e) and (f)], and distal [(h) and (i)] locations of mouse colon. Scale bars: 200 μm. Figures 15(d), 15(g), and 15(j) are histology images, 1 × 1.8 mm^2, from proximal, middle, and distal regions, respectively. Scale bar: 200 μm.

4.4 Discussion

We have constructed a confocal microscope combining beam scanning and rapid stage scanning at 7 mm/sec to rapidly acquire high aspect ratio images. We demonstrate this technique on excised mouse colon to enable evaluation of tissue features along the length of the colon. Extended FOV images of normal mouse colon show the homogeneous distribution of colon crypts along the entire length of the colon. In contrast, the extended FOV images of inflamed tissue show a wide range of crypt size, shape, and distribution. Some regions appear quite normal; whereas, other regions show extremely distorted crypt structure. For example, if we compare the confocal image with the most severe crypt distortion in the inflamed colon, Fig 15(e), to an image taken near the same location in the

normal colon, Fig 14(f), the average area and standard deviation of the crypts defined by the bright ring of colonocyte nuclei is 4231 ± 2226 μm^2 for the inflamed tissue and 1076 ± 332 μm^2 for the normal tissue. Furthermore, the average eccentricity and standard deviation decreases from 0.80 ± 0.14 to 0.73 ± 0.13 from inflamed to normal tissue, where a circle has an eccentricity of 0 and a line has an eccentricity of 1. Rapid confocal imaging and image processing could provide a quantitative map of crypt area and eccentricity to measure severity of tissue distortion with inflammation. It may also be used for fast identification of focal changes such as aberrant crypt foci, which are small groups of crypts with altered size and shape thought to be precursor lesions to colon cancer [96].

We have presented confocal images that show potential for classifying an inflammatory region within the colon based on crypt lumen size, shape, and distribution. The homogeneity of normal mouse colon tissue compared to the heterogeneous nature of tissue exhibiting chronic inflammation is clearly evident within regions of the colon. Some regions within the inflamed colon, Fig 15(b) and 15(c) for example, may be considered "normal"; therefore, a rapid stage scanning image technique to evaluate the entire organ to identify regions of interest may be valuable. We are able to acquire data along the entire length of the mouse colon in a relatively short period of time.

5. PULSE COUPLE NEURAL NETWORK ALGORITHM FOR QUANTITATIVE ANALYSIS OF EPITHELIAL NUCLEI*

5.1 Introduction

There is a need for automated cell nuclei segmentation to provide rapid image analysis of reflectance confocal microscopy and endomicroscopy images of epithelial tissue; however, the low contrast, non-uniform images confound the development of accurate segmentation algorithms [97,98]. Quantitative data may be obtained by tedious manual segmentation of nuclei. Although this method introduces inter- and intra-observer variability, it remains the gold standard for evaluation of segmentation accuracy.

5.1.1 Challenges of Automated Nuclear Segmentation

Both fluorescence and reflectance confocal microscopy and endomicroscopy have been developed for tissue imaging [4]. While fluorescence confocal microscopy can provide high contrast images of cellular features, it requires administration of exogenous fluorescent dyes either topically or systemically to provide contrast. Reflectance confocal microscopy (RCM) exploits endogenous reflectance contrast produced by natural variations in the refractive index of cellular and tissue components [28,99]. Low concentration acetic acid (vinegar) may be applied to enhance

* Reprinted with permission from A Pulse Coupled Neural Network Segmentation Algorithm for Reflectance Confocal Images of Epithelial Tissue by Harris, Meagan A., Andrew N. Van, Bilal H. Malik, Joey M. Jabbour, and Kristen C. Maitland, 2015. PloS One, 10(3), 1 – 20, Copyright 2015 by Harris, et al.

contrast of cell nuclei and is already approved and routinely used in humans [43,66]. Use of near-infrared illumination in RCM allows deeper tissue penetration over one-photon fluorescence confocal, extending through the full thickness of the epithelium [28].

Segmentation of cell nuclei and quantification of NCR and nuclear size in RCM images of epithelial tissue can enable objective evaluation of tissue features for precancer detection [67,100]. If this data were provided rapidly or in real-time, the technique could be used to guide biopsy site selection and improve diagnostic yield. However, nuclear to background contrast can be low in RCM images, particularly in comparison to fluorescence confocal imaging with dye-based contrast agents. Furthermore, reflectance signal from the epithelium is not specific to cell nuclei. Cell borders, intracellular organelles such as the endoplasmic reticulum and mitochondria, melanin, and keratin all contribute to detected backscattered signal [28].

5.1.2 Automated Nuclear Segmentation Methods

Thresholding, a simple and commonly used segmentation algorithm, has proven to be useful in medical image processing [101]. This method relies on the pixel intensity of a region of interest and isolates the region based on whether a pixel is above a certain threshold value. Variations in region intensity are compensated for by calculating the optimal threshold for each individual image, known as Otsu's method [102]. Otsu's method is an algorithm that determines the threshold that minimizes the intra-class variance in an image, assuming that the image contains only two classes of pixels. However, the technique suffers when trying to segment regions of non-uniform intensity, a factor prevalent in confocal reflectance images. For instance, a free open-source software

package, CellProfiler.org, is available for object segmentation using Otsu's method; however, manual control of threshold values complicates rapid evaluation of images with varying contrast across a single image or images at multiple depths.

Other common segmentation techniques include the edge detection and watershed algorithms. Edge detection is a technique that attempts to identify features in the image through differentiation [103]. These features are identified through different filtering methods such as those by Canny, Sobel, or Prewitt [104-106]. However, attempts to identify and separate features are often confounded by image noise and regions of non-uniform intensity. The watershed segmentation algorithm has been successfully used in some confocal images [107], and is based on modeling the image as a topographical relief. The algorithm requires the use of markers to prevent over-segmentation of the image, which can be difficult to obtain automatically and may require manual methods.

Most segmentation algorithms reported in the literature were designed to segment higher contrast confocal images with fluorescently stained tissue [107-111]. Previous work done by Luck et al. introduced a segmentation algorithm by use of Gaussian Markov random fields (GMRF) for reflectance confocal endomicroscopy images of epithelial tissue [112]. The GMRF technique utilizes local pixels to estimate the actual grayscale value of a pixel. This generates regions of uniform intensity that can be segmented by morphological features such as size and eccentricity. The algorithm has been shown to be successful, detecting 90% of nuclei in a frame at a 14% error rate [112]. However, the algorithm suffers from over-segmentation in some images, resulting in a

number of false-positives. Additionally, it is difficult to determine the number of fields required to make a good segmentation of each image.

Pulse coupled neural networks (PCNN) are derived from research on the mammalian visual cortex done by Eckhorn [113]. The network provides a useful biologically inspired tool for image processing. Each neuron represents a pixel on the image and is affected by the initial state of the pixel in the image, and the states of the surrounding neurons. The output of the network generates a series of temporal pulses, which can be used in many different image processing applications such as image segmentation or image fusion [114]. While the original PCNN model is strictly based on the neuron model created by Eckhorn, there are other networks specifically designed for image processing methods such as the intersecting cortical model or spiking cortical model (SCM) [115].

The algorithm introduced below utilizes a PCNN, specifically the SCM, to fully automate the segmentation process. The algorithm is able to efficiently segment epithelial nuclei over varying depth below the tissue surface and output valuable quantitative information such as the nuclear-to-cytoplasmic ratio, number of objects segmented, average nuclear area, and standard deviations where appropriate.

5.2 Materials and Methods

5.2.1 Sample Preparation and Image Acquisition

5.2.1.1 Imaging of Porcine Oral Mucosa

Normal porcine cheek tissue was acquired through the tissue sharing program at Texas A&M University (TAMU) which is designed to reduce the

number of animals needed to accomplish research goals. Because the tissue was transferred from another study approved by the TAMU Institutional Animal Care and Use Committee (IACUC) after the animal was terminated, review of this work by the TAMU IACUC is not required. Following excision from the oral cavity, the buccal tissue was transported to the lab for imaging. Prior to confocal reflectance imaging, the sample was submerged in acetic acid for 1 minute to enhance nuclear contrast. The bulk sample was rinsed in a phosphate buffered solution and then placed on the inverted confocal imaging system with the buccal mucosal surface facing down towards the microscope objective.

Confocal reflectance images of the porcine buccal mucosa were acquired with 830 nm illumination using the VivaScope 2500 (Caliber I.D., Rochester, NY). This instrument is an inverted RCM designed to image unsectioned excised surgical specimens. Individual frame size provides a FOV of 750 × 750 μm^2 at a rate of 9 frames per second. Optical resolutions are 1.5 μm and 5 μm for lateral and axial planes, respectively. Images were acquired down to approximately 160 μm below the tissue surface using an infinity corrected, 0.85 NA, water immersion objective lens. At this depth, reflectance signal is still detectable and the bases of rete ridges are prevalent; however, nuclei are no longer resolvable due to tissue scattering. A 3 × 3 array of images was captured at each depth to increase the total area imaged. To evaluate segmentation capability in images of different contrast and tissue features, images at four depths, approximately 8, 24, 40, and 64 μm below the surface, were analyzed. Images were cropped to a circular region with a diameter of 450 μm in order to reduce the range of focal plane depth due to field curvature. Nuclear objects were manually segmented by a

single observer via visual recognition by applying nuclear masks to nuclei in a given frame. This manual segmentation was used as the gold standard in evaluation of the automatic segmentation algorithm. The objects' size, distribution, and contrast were also used to create an image model.

5.2.1.2 Imaging of Human Oral Mucosa

In order to demonstrate that the applicability of our approach is relatively independent of imaging system characteristics and epithelial tissue type, we applied the segmentation algorithm to images of excised human oral tissue acquired using a different RCM system [116]. Briefly, the illumination light, emitting at 811 nm, was raster scanned and focused through a water immersion microscope objective (40×, 0.8 NA). Light backscattered from the tissue was focused onto a pinhole before being detected by a photomultiplier tube detector. The field of view was measured to be ~625 μm diameter at the sample, with lateral and axial resolutions of 0.65 μm and 5 μm, respectively. Oral tissue collection and imaging protocols were approved by the Institutional Review Boards at Texas A&M University and TAMU – Baylor College of Dentistry, and written consent was obtained from study participants. The images presented here were obtained from a human tissue biopsy that was clinically diagnosed as inflammation and histopathologically diagnosed as gingival hyperplasia. RCM imaging was performed within 30 minutes following biopsy. Gauze soaked in acetic acid was applied for 1 minute prior to imaging. In comparison to porcine mucosa, we were able to image and observe discernable features relatively deeper (>300 μm) within the human oral tissue.

5.2.2 Image Model of Epithelial Tissue

An image model was created in MATLAB to closely represent confocal images of epithelial tissue. Parameters such as nuclear size, density, and contrast were obtained directly from manually segmented confocal reflectance images of porcine buccal mucosa at various locations and depths. 750 circular objects with an area of 90 px^2 (corresponding to ~8 μm diameter nuclei) are randomly distributed without overlap in a set of six 1000 × 1000 px^2 images. The ratio of average nuclear intensity to average background intensity (nuclear to background contrast ratio) was varied from 2.6 to 1.6 by decreasing the signal from the nuclear objects and increasing the signal from the background to simulate the loss of contrast with increasing imaging depth in tissue. Each object is modeled with a Gaussian spatial distribution of pixel intensity to adequately represent the nuclear appearance. Each object's peak signal was determined using a histogram of intensities of manually segmented nuclei from depths with comparable nuclear to background contrast ratio. The background signal was modeled as Gaussian white noise with mean and variance based on intensity variation in cytoplasmic signal bordering nuclei in manually segmented images at depths with comparable nuclear to background contrast ratio. The background of the image model did not include tissue features such as cell borders and areas of high keratinization.

5.2.3 Spiking Cortical Model Algorithm

The automated PCNN based algorithm was written in MATLAB (The MathWorks, Inc., Natick, Massachusetts, United States) and is available at the online

Zenodo database (https://zenodo.org/record/12804) [117]. The nuclear-to-cytoplasmic ratio, area of segmented nuclei, and the total number of objects segmented were recorded and compared to manual segmentation. Object- and pixel-based sensitivity and pixel-based specificity were calculated using the manually segmented images as the gold standard. For object-based sensitivity, an object was considered a true positive if any of the pixels within an object were correctly classified. All other missed objects were considered false negatives. For pixel-based specificity, the number of true negative pixels was counted as the active FOV less the total number of true positive, false positive, and false negative pixels. The flow chart for the SCM algorithm can be seen in Fig 16. The main steps shown in the chart are described in detail below. Fig 17 illustrates various steps in the algorithm during the segmentation process of an example confocal image Fig 17(A). The SCM algorithm takes approximately 20 seconds to process a single confocal image, performed on a laptop computer with 2.3 GHz processing speed and 16 GB of RAM.

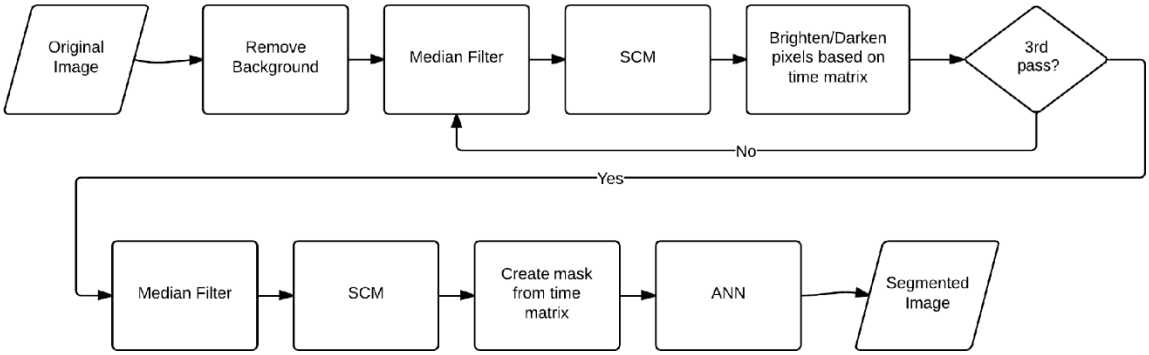

Fig 16. Flowchart of main steps of the automated SCM segmentation algorithm for segmenting nuclei in RCM images of epithelial tissue.

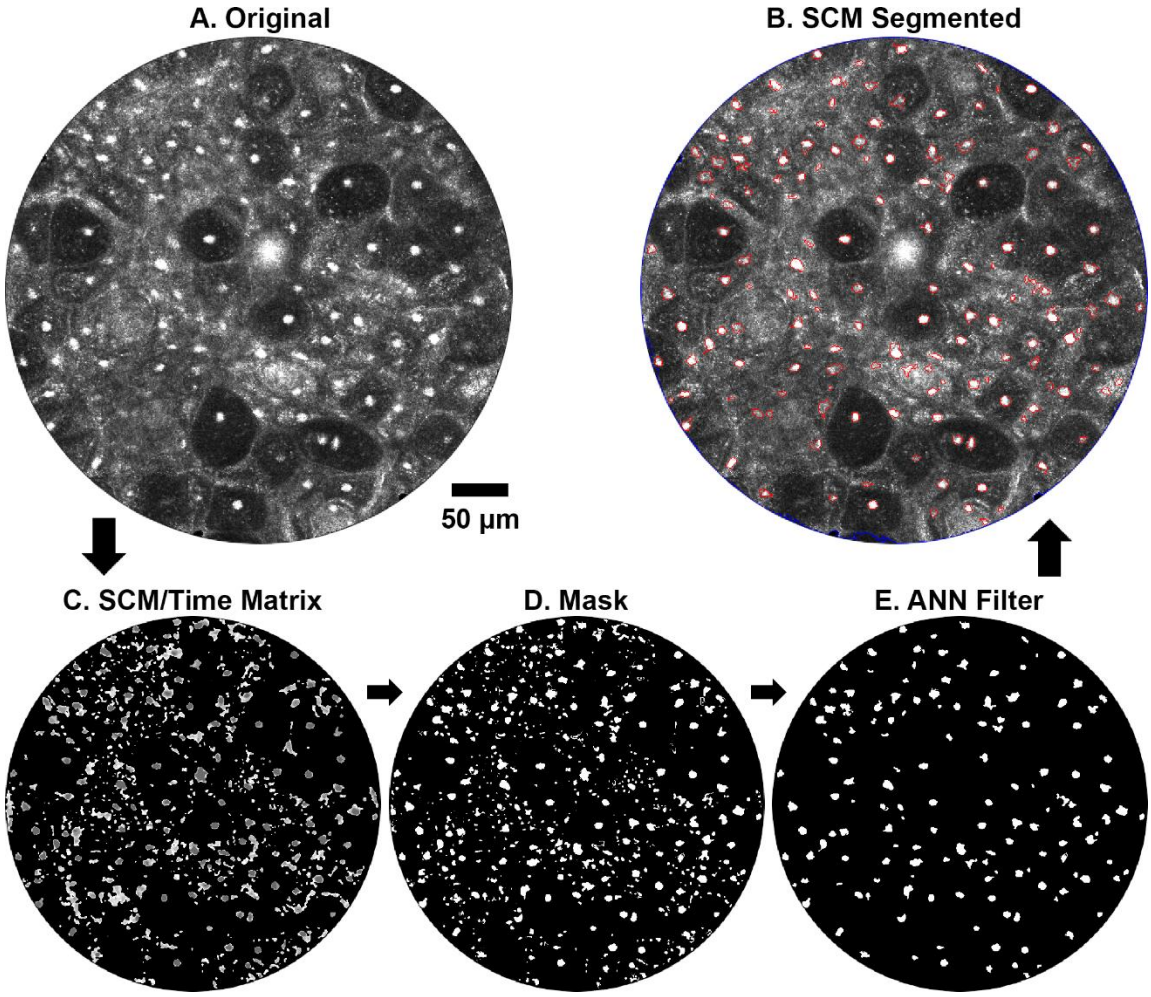

Fig 17. Image steps of SCM segmentation algorithm. (A) Original confocal image of porcine buccal mucosa showing range of nuclear to background contrast. (B) SCM segmentation of (A). (C) Output of final SCM filter showing time matrix of pulse outputs. (D) Segmentation mask obtained from the time matrix. (E) Output of the ANN classifier defining the segmented objects in (B).

5.2.3.1 Background Removal

Occasionally, the tissue may not fill the entire imaging FOV. If the active FOV is not well-defined, NCR calculations using the entire FOV may be erroneously low. A threshold algorithm is utilized to remove the background of the image

leaving the active FOV. This was accomplished by assuming the background is composed of a large contiguous area of dark pixels distinct from the foreground (i.e. the tissue). A scaled threshold for the background was calculated using Otsu's method [102], which provides an optimal division between the foreground and background of each image. Subsequently, an area filter was applied to remove the background from the image. After removal of the background pixels, the area of the foreground was calculated for use in the NCR calculation.

5.2.3.2 Pulse Couple Neural Network

Image filtering and segmentation is carried out by the SCM developed by Zhan, et al [118], which models pixels in an image as neurons in an interconnected neural network. The SCM is a biomimetic algorithm and a simplified variant of the original PCNN visual cortex model. The model itself is composed of three equations: an internal activity function, a neural output function, and a dynamic threshold function. The matrix created by the output function is the only result that is examined. The threshold and internal activity functions are hidden and only used to calculate the output. Finally, a time matrix is a single composite image created by these outputs that records the pulse time of each neuron run through the SCM. The functions compose an abstract representation of a biological visual model that separates various "features" of an image into different outputs separated temporally. Here, we define a feature as a set of pixels of similar intensity grouped spatially. Image filtering is done by reducing the amount of features present within the image, while the features of interest (i.e. nuclei) are isolated in

segmentation. The extracted features depend on a number of parameters, *f*, *g*, *W*, and *h*, as described below and in Chen, et al. [119].

A neuron in the SCM model is defined as these three equations applied to a single pixel within the image. The variables *i* and *j* denote the position of the neuron of interest in the image, while *k* and *l* define the positions of the neighboring neurons relative to the current neuron. The internal activity function takes an input image and forwards it into the neuron layer:

$$U_{ij}(n) = fU_{ij}(n-1) + S_{ij}\sum_{kl} W_{ijkl}Y_{kl}(n-1) + S_{ij} \qquad (10)$$

where S_{ij} is the input image, U_{ij} is the internal activity of the neuron, Y_{kl} is the neuronal output of the neighboring neuron, and *n* defines the current iteration of the network. The parameter *f* is the decay coefficient for the internal activity function, which affects the temporal spacing of features. The parameter W_{ijkl} is the weight matrix determines the connections between neurons, or the association strength of neighboring pixels within a feature [119].

The neural output function compares the internal activity of the neuron to its current threshold:

$$Y_{ij}(n) = \begin{cases} 1, U_{ij}(n) > E_{ij}(n) \\ 0, otherwise \end{cases} \qquad (11)$$

where Y_{ij} is the neuronal output and E_{ij} is the dynamic threshold of the neuron as defined in Equation 12. The threshold function is calculated by addition of the previous threshold with the neuronal output:

$$E_{ij}(n) = gE_{ij}(n-1) + hY_{ij}(n) \tag{12}$$

The parameters *g* and *h* are defined as the decay coefficient and amplitude for the threshold function, respectively. Both parameters determine the precision of intensities for each feature [119].

Through trial and error, *f*, *g*, and *h* were set to 0.928, 1.078, and 1.4, respectively. The parameter W_{ijkl} was set to [0.0125, 0.025, 0.0125; 0.025, 0, 0.025; 0.0125, 0.025, 0.0125]. Once these tunable parameters were optimized using training data from porcine buccal mucosa, they were kept constant for segmentation of all porcine and human tissue images. While automated methods exists for setting PCNN parameters [119], manually setting the parameter values for the network provided more desirable results, such as maximizing true positives while reducing false positives. The final values were chosen so that the algorithm was tuned to provide an optimized output for both sensitivity and specificity. The parameters could be modified to prioritize sensitivity over specificity, for example, if a specific application warranted it. However, all tunable parameters depend on each other and affect output results, complicating this parameter tuning.

5.2.3.3 Time Matrix

The network was modified such that each neuron representing a pixel could only output once. Each successive neuronal output was labeled by iteration number, generating a time matrix as seen in Fig 17(C). The time matrix is a composite image that combines the pulse outputs of the SCM, and organizes the pixels in the image

based on similar intensity [118]. Since brighter elements of the image (e.g. bright pixels, nuclei, etc.) are stored in earlier iterations and darker elements (e.g. background, dim artifacts, out of focus objects etc.) are stored later, the time matrix can label the image according to the pulsing order. Here, we use the time matrix to 1) filter and 2) obtain the segmentation mask, Fig 17(D).

Since darker elements of the image are stored in later iterations of the network, only the first 6 output iterations of the network are analyzed. The size and eccentricity values were measured for each object within each output iteration. Using this information, the pixel intensity values in the original image were brightened or darkened with gamma corrections. For the earlier iterations, large areas were lowered in intensity to darken the intensity of large saturated areas. For later iterations, small, round areas were raised in intensity to brighten darker nucleus shaped objects.

Following successive PCNN filtering, a final time matrix was generated to produce a segmentation mask. An initial mask was first created by taking the regional minima of the time matrix. This process captures the central area of each nucleus, but leaves out the periphery. By "growing" the initial mask by adding successive iterations, a segmentation mask was obtained. Each iteration was added to the segmentation mask until the object passed a set area and eccentricity limit.

5.2.3.4 Artificial Neural Network Classifier

Following the segmentation done by the PCNN, an artificial neural network (ANN) classifier was made using the built-in MATLAB Neural Network Toolbox™. By inputting a set of examples to this classifier, we train the classifier to

remove objects that are more likely to be false positive nuclei based on a set of features. Using a database of objects created by manual segmentation, the network was trained by an 8-dimensional feature vector which included area, eccentricity, extent, solidity, foreground intensity and standard deviation, and background intensity and standard deviation. Out of the 36 total images, two images were randomly selected at each depth with no overlapping lateral position for all depths. The database of approximately 1800 objects in these 8 images was randomly divided into three sets: 70% as a training set, 15% to validate that the network is generalizing and to stop training before overfitting, and 15% as an independent set to test for network generalization. After creating the neural network classifier with these 8 images, it was applied to the remaining 28 images. All reported results and images in this paper are from the 28-image dataset and do not include the 8-image training data. For the image in Fig 17(A), a finalized segmentation output of nuclear objects, Fig 17(B), was obtained after removal of the ANN classified objects from Fig 17(E).

5.2.3.5 MATLAB Output and User Interface

The MATLAB regionprops function to measure properties of image regions was applied to the image mask in order to generate information about nuclear area, NCR, and the number of objects detected in the image. The mean and standard deviation for nuclear area was calculated for the image. The NCR was calculated by taking the total area of the objects present in the image and dividing by the remaining area in the FOV. Fig 17(B) shows an image output generated by the SCM algorithm which

includes a blue border designating the segmented active FOV and red borders around each segmented object.

The MATLAB GUIDE tool was used to build a user interface for the algorithm. The interface enables the quick processing of multiple images, as well as preview and batch save capabilities. In addition, the interface enables the export of the information generated for each image as a Microsoft Excel spreadsheet file and lists the data accordingly for each analyzed image.

5.3 Results

5.3.1 Image Model

The SCM automated segmentation algorithm, including the ANN classifier trained on objects in confocal images of epithelium, was first applied to the image model of epithelial tissue to evaluate the limitations of the algorithm. The segmentation performance was assessed based on sensitivity (true positive rate) and specificity (true negative rate) for each contrast value or nuclear to background ratio. Sensitivity was calculated using both object and pixel based methods. Specificity was calculated by pixel based method only due to the inability to quantify true negative objects. SCM analysis of the image model is shown in Fig 18. Contrast decreases from 2.6 to 1.6 moving down each column. The original simulated images shown in the first column are 1000×1000 px^2 FOV containing 750 objects distributed randomly without overlap. The yellow box indicates the location of the zoomed in 250×250 px^2 FOV regions featured in the second column. The third column shows the SCM segmentation of the zoom in area. The fourth column is a sensitivity map depicting the accuracy of the SCM algorithm to detect

simulated nuclear objects with varying contrast. Green pixels on the sensitivity map indicate true positives, blue pixels are false negatives, and red pixels are false positives.

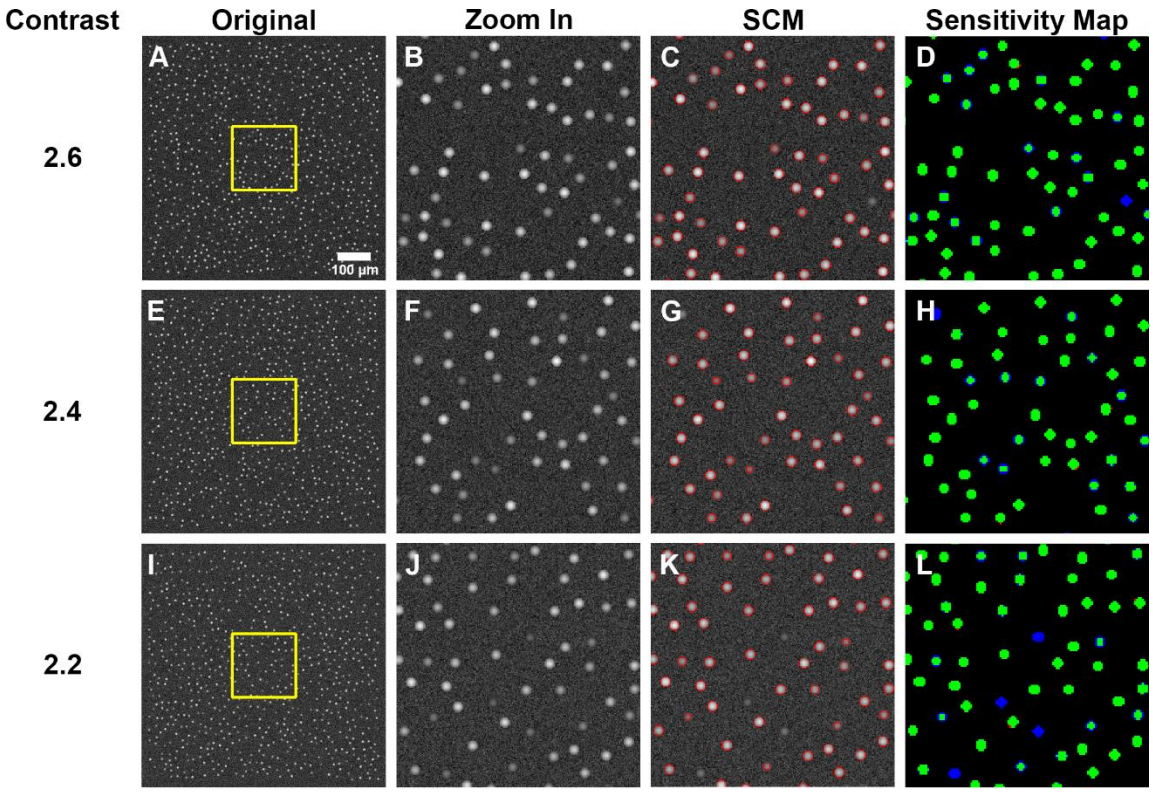

Fig 18. SCM segmentation of confocal image model with sensitivity evaluation. 750 × 750 µm^2 field of view confocal image model with nuclear to background contrast, (A) 2.6, (E) 2.4, (I) 2.2, (M) 2.0, (Q) 1.8, and (U) 1.6. (B), (F), (J), (N), (R), (V) 190 × 190 µm^2 field of view zoom in of yellow box from (A), (E), (I), (M), (Q), and (U), respectively, showing nuclear object detail. (C), (G), (K), (O), (S), and (W) SCM segmentation and sensitivity map comparison to objects in the original model images of (B), (F), (J), (N), (R), and (V), respectively. Green pixels (true positives), blue pixels (false negatives), and red pixels (false positives).

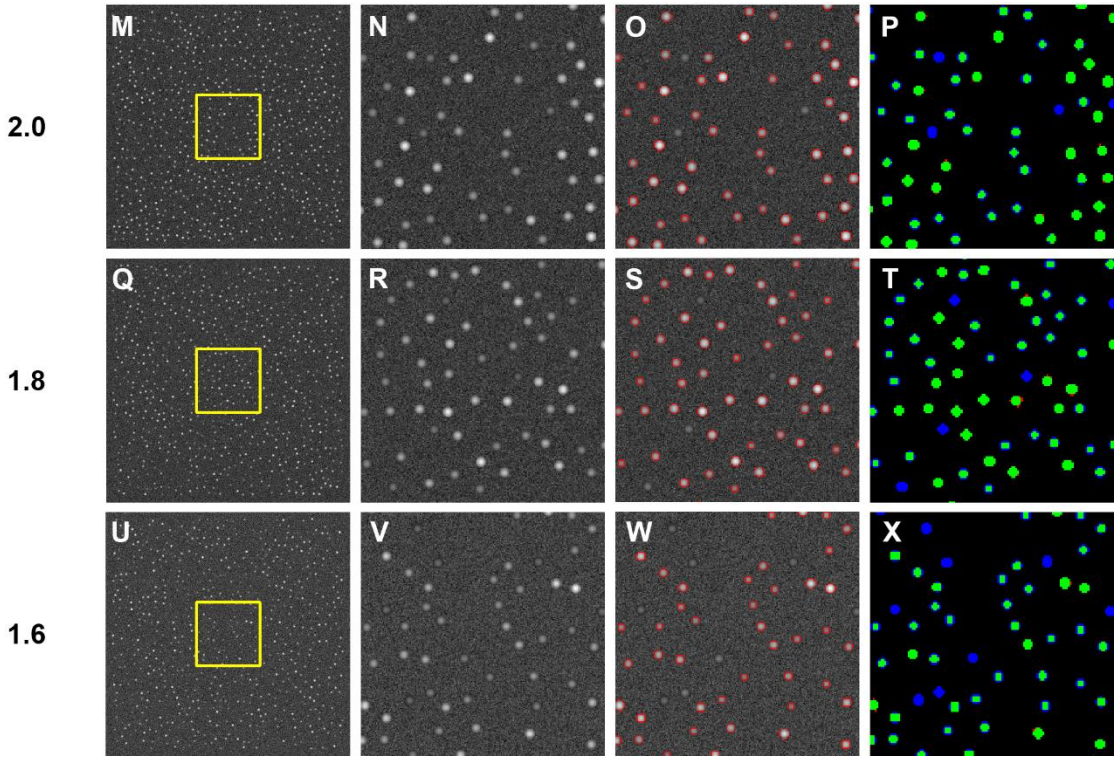

Fig 18. Continued.

5.3.2 Porcine Buccal Mucosa Images

Automated segmentation analysis was performed on 28 confocal images of excised porcine buccal mucosa at four depths spanning the surface to 60 µm in depth. Example SCM segmentation results for two images are shown in Fig 19. The image in Fig 19(A), obtained approximately 20 µm below the tissue surface, represents a high contrast, easily segmented image from the superficial layer in the epithelium. The image has 79 manually segmented objects and an average object to background contrast of 2.26. The image in Fig 19(C), obtained approximately 60 µm below the surface, demonstrates relative difficulty in segmenting low contrast images. This image has 259 manually segmented objects and an average contrast of 1.51. SCM segmentation is shown in Fig

19(B) and 19(D). The high contrast image in Fig 19(A) had the highest SCM segmentation sensitivity, with an object based sensitivity of 94%, pixel based sensitivity of 84%, and pixel based specificity of 99%. For the low contrast image in Fig 19(C), SCM segmentation had object based sensitivity of 70%, pixel based sensitivity of 61%, and pixel based specificity of 98%.

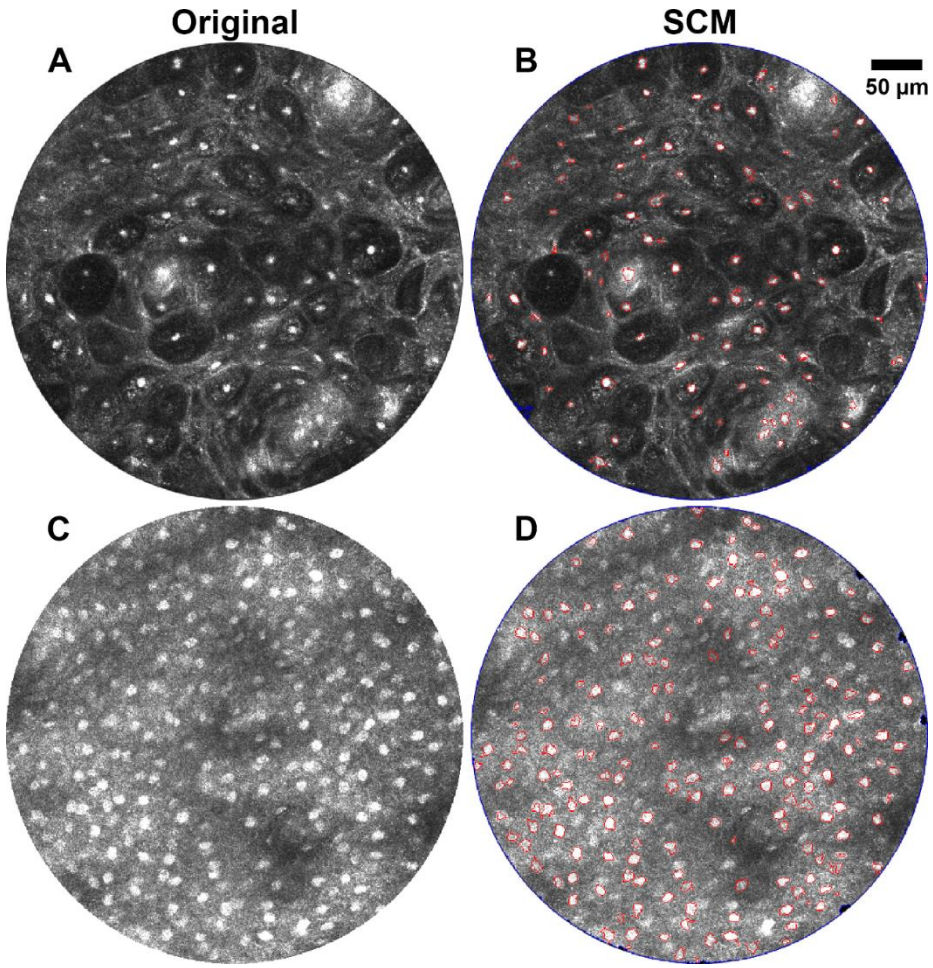

Fig 19. Comparison of SCM segmentation algorithms on confocal images of oral mucosa with high and low contrast. Original confocal images of porcine buccal mucosa with (A) high and (C) low nuclear to background contrast. (B) and (D) SCM segmentation of (A) and (C), respectively.

The plot in Fig 20 illustrates the SCM segmentation results of the confocal image model and the porcine buccal mucosa tissues with respect to image contrast. With increasing image contrast, both object-based and pixel-based sensitivities improve. Because the image model simulates only nuclear objects and not other cellular features that scatter light, there were very few false positive pixels and numerous true negatives. Therefore, the specificity for all confocal image model figures is practically 100%. The highest object-based sensitivity measured for the confocal image model was 97% for a nuclear to background contrast of 2.6. Whereas, the highest object-based sensitivity measured for the porcine tissues was 89% with an image contrast of 2.06. Pixel-based sensitivity is less than object-based sensitivity primarily due to undersegmentation of objects yielding more misclassified pixels within detected objects. The specificity does not vary significantly due to the disproportionately large number of pixels in the active FOV in comparison to the false positive pixels.

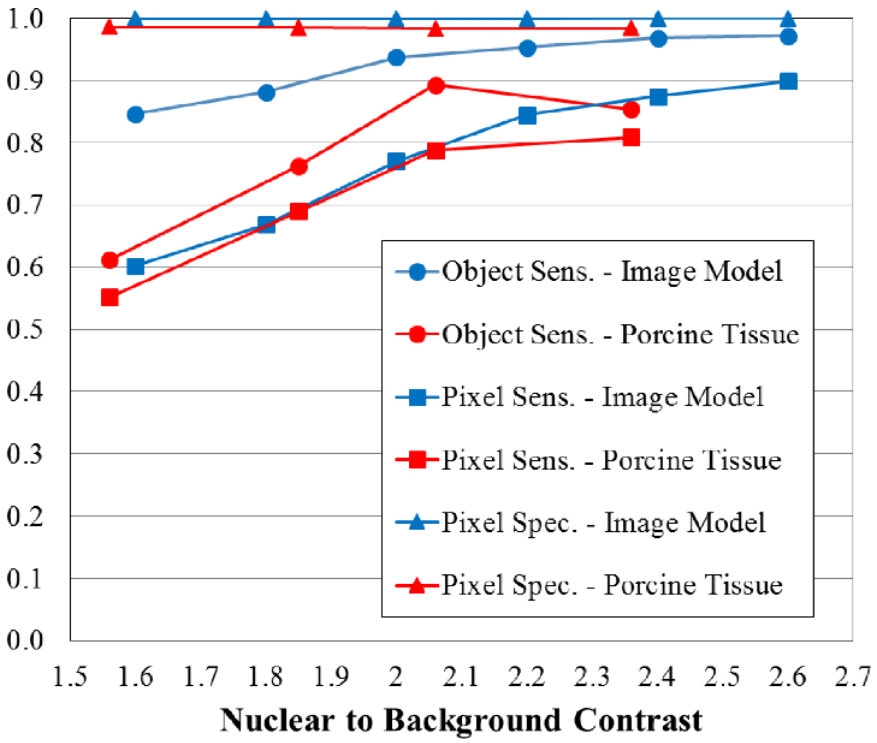

Fig 20. Effect of nuclear to background contrast on accuracy of SCM segmentation. Object-based sensitivity (Object Sens.), pixel-based sensitivity (Pixel Sens.), and pixel-based specificity (Pixel Spec.) are plotted for SCM segmentation of the simulated image model and captured images of porcine buccal mucosa as a function of contrast. Increasing depth below the surface of mucosal tissue corresponds to decreased contrast.

Table 3 summarizes the performance of the SCM segmentation algorithm over 28 images of porcine tissue. A total of seven adjacent images were analyzed at each of four depths. The table includes image properties such as average object to background contrast and total number of manually segmented objects at each depth below the tissue surface. The number of true positive (TP) and false positive (FP) objects, and percent error are presented for SCM segmentation. A pixel-based F-measure value, where $F1 = \frac{2 \times sensitivity \times specificity}{(sensitivity + specificity)}$, is also reported as a means to evaluate accuracy of the segmentation algorithm based on both sensitivity and specificity [120].

Table 3. SCM segmentation of confocal images of porcine tissue.

Image Properties			SCM				
Depth [μm]	Contrast	# Objects	True Positives	False Positives	% Error Sensitivity (object)	% Error Sensitivity (pixel)	F-Measure
7.93	2.36	554	473	271	14.62%	19.14%	0.89
23.78	2.06	749	669	193	10.68%	21.22%	0.87
39.63	1.85	1167	889	63	23.82%	31.01%	0.81
63.40	1.56	1479	902	42	39.01%	44.86%	0.71

To further compare segmentation by SCM to manual segmentation, normalized line profiles through two nuclei from the image in Fig 19(A) are shown in Fig 21 as well as a line profile through an image model object. The original image of an object from an image model figure is shown in Fig 21(A). A line profile though the object is shown in Fig 21(D) where the green lines represent the SCM segmentation, Fig 21(C), which overlaps on the designated object border as seen in Fig 21(B). The original images of a bright, well-resolved nucleus and a dim nucleus that is not easily resolved are shown in Fig 21(E) and 21(I), respectively. Segmentation of the well-resolved nucleus, Fig 21(H), illustrates that SCM segmentation tends to have a tight fit around nuclei, similar to manual segmentation. The intensity plot for a nucleus that is not as well-resolved is shown in Fig 21(L). Here, the green lines represent both SCM and manual segmentation, which overlap for this orientation of the line profile of the nucleus. As seen in these plots, manual segmentation and SCM segment nuclei around the half maximum point.

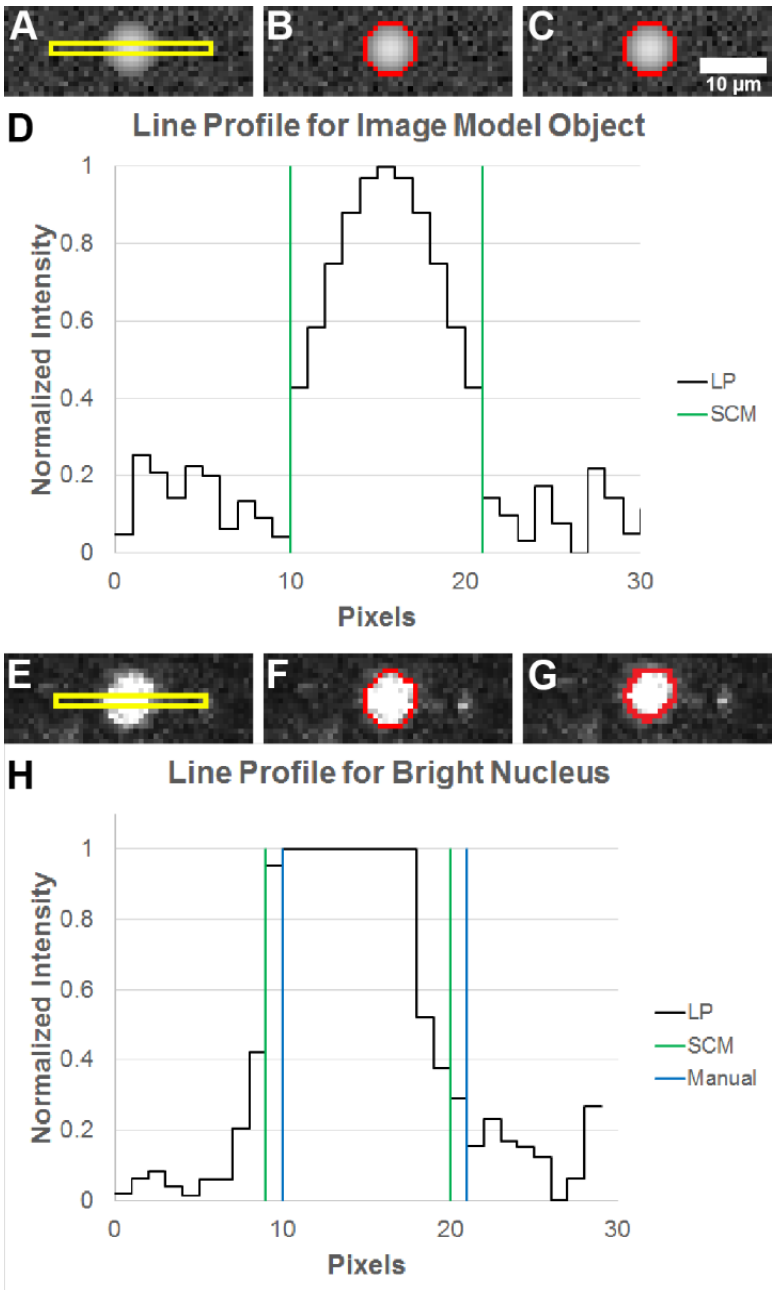

Fig 21. Line profile plots to compare SCM and manual segmentation. (A) Representative image model object, (B) SCM segmentation of selected object, and (C) actual object border. (D) Normalized line profile (LP) plot for line indicated by the yellow box in (A). (E) Bright and (I) dim nuclei, (F) and (J) SCM segmentation, and (G) and (K) manual segmentation. (H) and (L) Normalized LPs with segmentation borders identified for SCM and manual segmentation. Note in (L) that SCM and manual segmentation overlap.

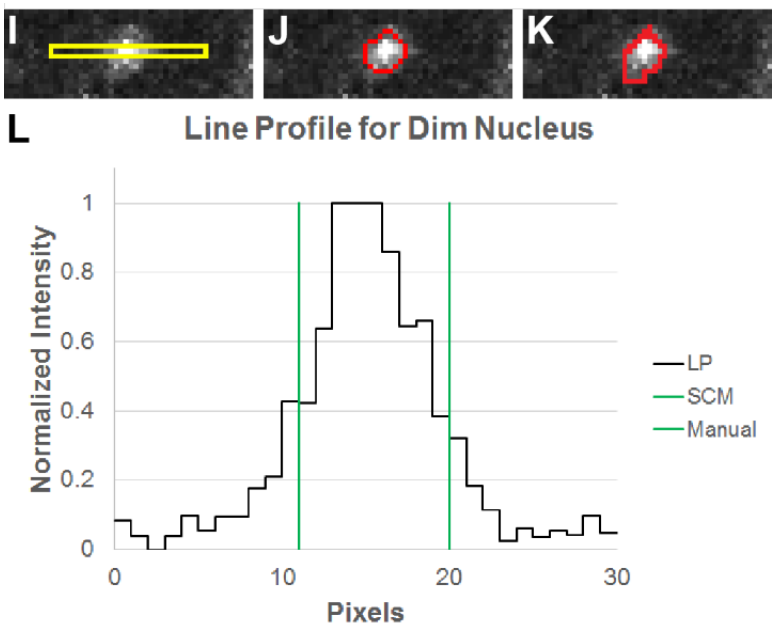

Fig 21. Continued.

Table 4 summarizes SCM segmentation of confocal images of epithelial tissue in comparison to manual segmentation. The total number of objects segmented is listed per depth. The greater number of objects segmented near the surface by SCM may be attributed to false positives from non-nuclear image features. Average NCR, nuclear area, and nuclear diameters are also shown by depth below tissue surface. Because of the irregular shape of nuclear objects, average diameter is calculated from the average area. As expected for epithelial tissue, the number of segmented objects increases with image depth; however, the number of objects segmented with SCM does not increase at the same rate as manual segmentation. This reduced sensitivity, due to low nuclear to background contrast, results in underestimation of NCR with depth.

Table 4. Comparison of SCM to manual segmentation of objects.

Image Properties		SCM				Manual			
Depth [μm]	**Contrast**	**# Objects**	**NCR**	**Nuclear Area [μm^2]**	**Diameter [μm]**	**# Objects**	**NCR**	**Nuclear Area [μm^2]**	**Diameter [μm]**
7.93	2.36	744	0.0345	49.11	7.91	554	0.0223	43.53	7.44
23.78	2.06	862	0.0452	54.44	8.33	749	0.0354	49.07	7.90
39.63	1.85	952	0.0556	60.06	8.74	1167	0.0597	52.11	8.15
63.40	1.56	944	0.0623	68.28	9.32	1479	0.0912	61.03	8.82

To illustrate the performance of SCM segmentation of individual nuclei, Fig 22 depicts examples of various segmentation scenarios that affect quantitative output of the algorithm. The confocal image from Fig 19(A) is seen in Fig 22(A) with a sensitivity mask overlaid on top. Green areas indicate a true positive match to the manual segmentation. Blue indicates a false negative, a nuclear object that was not segmented by SCM but was manually segmented. Red areas are designated as false positive, or objects that SCM detected but were not segmented manually. Fig 22(A) is labeled with the locations of the nuclei detailed here and shown in Fig 22B – 22G. Fig 22H – 22M are the SCM segmentation corresponding to the sensitivity maps of Fig 22B – 22G, respectively.

Fig 22N – 22S are the corresponding manual segmentation. The sensitivity map, Fig 22(B), shows an example of excellent segmentation by SCM as compared to manual segmentation. Fig 22(C) is an example of over-segmentation by SCM or excessive nuclei splitting due to low pixel intensities. The object was manually segmented as a single object because it is unlikely, but possible, that two nuclei would be positioned so close together within this superficial epithelial layer. Another example of over-segmentation also likely caused by low pixel intensities is shown in Fig 22(D), where the SCM algorithm segmented the object larger than the manual segmentation. It is possible that some nuclei may not be as well resolved due to their depth position relative to the focal plane, resulting in reduced intensity. Fig 22(E), a false negative, demonstrates this, showing the limitations of SCM segmentation. False positives can occur for many reasons such as tissue and image artifacts and, possibly, nuclei missed by manual segmentation. Fig 22(F) is an example of a false positive from a rete ridge or keratin pearl in the oral epithelial tissue. Fig 22(G) shows an object that was segmented by SCM, but not by manual segmentation. It appears to be the appropriate size of a nucleus, but was not manually segmented because of its location within the tissue.

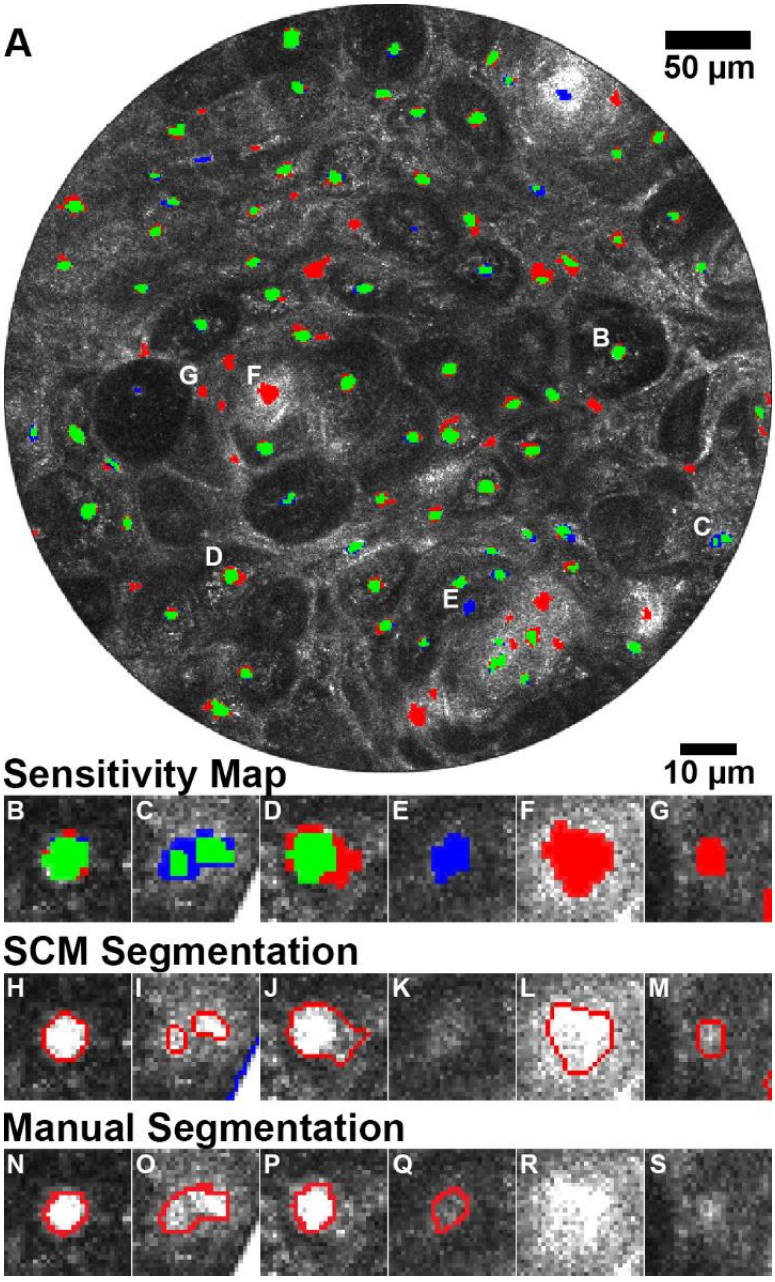

Fig 22. Evaluation of SCM segmentation performance. (A) Sensitivity map demonstrating true positives (green), false negatives (blue), and false positives (red). Objects of interest are labeled (B-G). Zoom-in of example nuclei demonstrating (B) excellent segmentation, (C) and (D) oversegmentation, (E) false positive, (F) image artifact false positive, and (G) false positive potentially missed by manual segmentation. (H-M) SCM and (N-S) manual segmentation of (B-G).

5.3.3 Human Oral Mucosa Images

To demonstrate the ease of applicability of the SCM nuclear segmentation algorithm to images acquired from other tissue types and using different RCM systems, human oral mucosal tissue was imaged with a different RCM system [116]. A total of 9 confocal images spanning a range of depth from 60 µm to 300 µm within the human oral tissue were selected for validation of the SCM algorithm. These images were taken from a tissue biopsy suspected of inflammation and later classified by histopathology as gingival hyperplasia, a benign lesion. Fig 23 shows sections of the representative original and the corresponding segmented images from varying depths within the tissue. Note that in comparison to the porcine oral mucosa, overall slightly lower level of contrast was observed across the human oral epithelium. The object-based and pixel-based sensitivity values varied from ~50% to 73% and ~40% to 62%, respectively, and unlike images of porcine mucosa, without any correlation to the depth of imaging. The pixel-based specificity did not vary significantly and was over 98% in all instances.

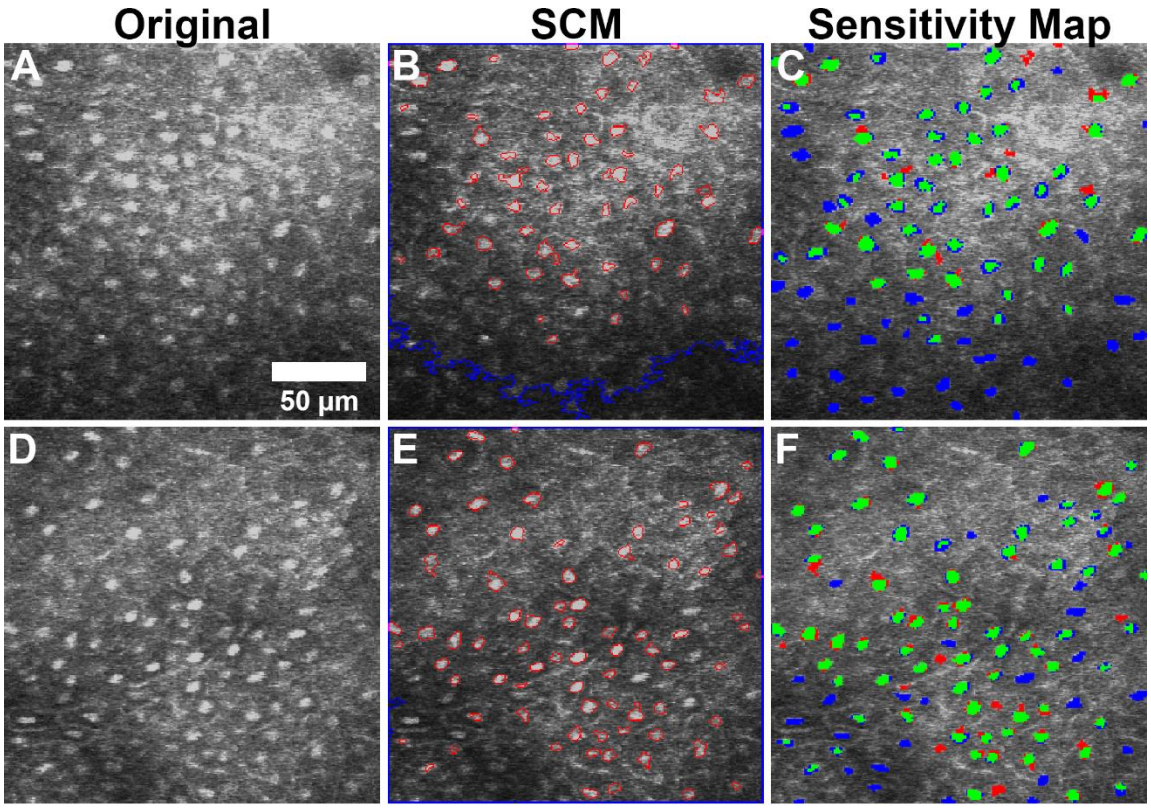

Fig 23. SCM segmentation of confocal images of oral mucosa at various depths. Original confocal images and SCM segmented images of inflamed human buccal mucosa at approximately (A, B) 90, (D, E) 180, and (G, H) 270 µm below tissue surface. True positives (TP), false negatives (FN), and false positives (FP) quantified for these depths were (C) 54 TP, 34 FN, 3 FP; (F) 72 TP, 26 FN, 7 FP; (I) 80 TP, 53 FN, 1 FP. Histology image (J) shows full epithelium. Images have been cropped from media file to restrict depth.

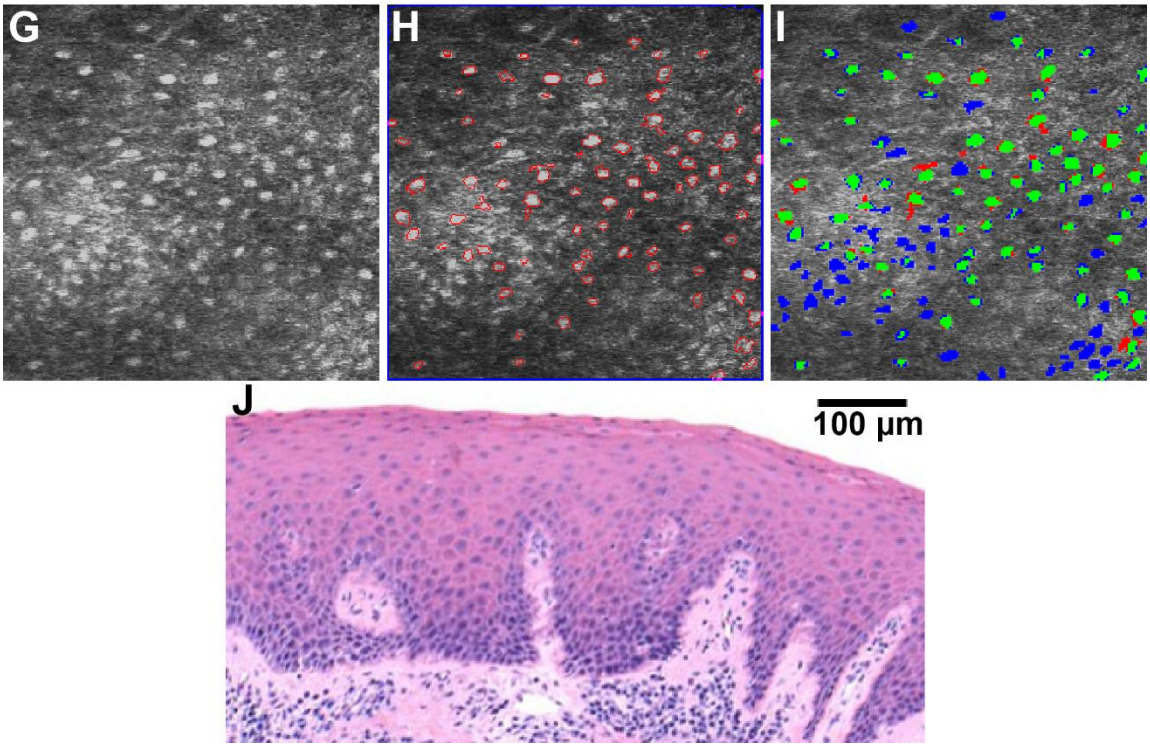

Fig 23. Continued.

It is worth noting that, in general, the values of sensitivity were lower in comparison to that of porcine tissue. This can be attributed to a number of reasons. The histology corresponding to the tissue biopsy was interpreted as hyperplasia which is typically marked by a benign proliferation of cells. This can be observed in the images throughout Fig 23 wherein the nuclear density is higher than that of Fig 19(A) and somewhat similar to that of Fig 19(C) (which is near the basement layer in porcine mucosa). Such nuclear crowding can result in a decrease in forward scattered light, as predicted by the theory of light scattering by densely packed structures [121]. A direct consequence of this is loss of contrast in the corresponding regions within the images. In addition, as can be seen in the histology section in Fig 23(J), the epithelial thickness varies

from less than 100 μm (in the areas of rete ridges) to over 300 μm, and islands of inflammatory cells are observed to penetrate into the epithelium. Both the interface of rete ridges and of these islands manifest as significant heterogeneities within the refractive index of the medium and may result in an increase in the backscattered light, as can be noticed in the lower left quadrant of Fig 23(E). Such variation in both contrast and levels of backscattered light across a single image presents a limitation of our SCM algorithm, and results in a decrease in the number of segmented objects and, consequently, more false negatives.

Another possible factor towards explanation of such behavior is that in order to image visibly at the depths of >300 μm within tissue, the optical power at the sample was kept relatively high and constant, and hence less optimal for more superficial layers of the tissue. This effect can be seen in the accompanying media file (S2 Video) wherein areas within the images from approximately the top one-third of the epithelium are saturated, the middle one-third exhibit better segmentation, and the lower one-third thickness shows loss of contrast simply due to imaging at greater depths within tissue. Accordingly, the sensitivity values in the images from the middle one-third of the tissue are the highest and monotonically drop off towards either side.

It is worth noting that although manual segmentation results were considered as a benchmark for quantifying SCM algorithm performance, such a benchmark itself is prone to both intra-observer and inter-observer variation. For instance, differences in display output settings (hue, contrast, brightness, etc.) vary between display screens (monitors and television) of different makes and models, and can potentially affect

the ability of a reader to segment the same image consistently. Inter-observer variation in manual image segmentation can have an even more profound impact since the training and understanding of the reader as to what area constitutes a cell nucleus is rather subjective. In order to quantify this effect, the pig tissue images were segmented by multiple readers. In comparison to the "expert" reader, the average area of segmented nuclei was underestimated by approximately 9% by one reader and overestimated by approximately 11% by another reader, highlighting the impact of inter-observer variation. Thus, such limitations should be kept under consideration when estimating the accuracy of any image segmentation algorithm. A potential alternative approach for establishing a gold standard would be to use a nuclear stain, such as DAPI, in fluorescence confocal microscopy to identify nuclei in *ex vivo* tissue samples. One-photon fluorescence has better resolution and reduced penetration depth in comparison to RCM; however, this would be an effective method for localization of nuclei in superficial epithelium. Although using exogenous contrast agents in humans is still limited for *in vivo* imaging, the use of fluorescent agents to enhance contrast in epithelial tissues has shown many benefits [4].

5.4 Discussion

Segmentation of nuclei in RCM images with low nuclear to background contrast is a challenge, particularly for fully automated algorithms. We have presented an automated PCNN nuclear segmentation algorithm based on the spiking cortical model. The segmentation accuracy was evaluated using an image model and confocal images of porcine oral epithelial tissue with varying nuclear to background contrast. The algorithm was further validated on RCM images obtained from human oral tissue using a custom-

built imaging system. Although segmentation accuracy degrades with reduced contrast and increasing image depth in tissue, automated segmentation of nuclei is significantly faster than manual segmentation, enabling rapid evaluation of tissue properties such as NCR and nuclear size.

6. EFFECTS OF AXIAL RESOLUTION ON EPITHELIAL NUCLEAR-TO-CYTOPLASMIC RATIO MEASURED WITH REFLECTANCE CONFOCAL MICROSCOPY

6.1 Introduction

Extensive cytological studies have been performed for characterization of morphological features of epithelial tissues, monitoring changes, and classification of tissue state. Many of these studies include quantitative data to assess nuclear and cellular diameters and areas. In some cases, the nuclear area is unchanging, and studies pursued cytoplasmic area, leading to a comparison of the NCR in various tissue states. It is common to compare NCR values when conducting similar studies, but in fact, there are many differences between the experiments and the state of the specimen in study.

To make a quantitative measurement like the NCR, the cell must exhibit contrast between the nucleus and cytoplasm. Contrast in reflectance confocal microscopy of epithelium is permitted from reflection and scattering from the nuclei, allowing for a quantitative comparison of normal and neoplastic changes in tissues by the NCR [122].

Addition of vinegar or acetic acid (3-6%) to the mucosal surface enhances backscattering from cell nuclei in reflectance confocal microscopy, which improves contrast [43].

6.1.1 Nuclear-to-Cytoplasmic Ratio of Cervical Epithelium

Sung conducted a study that measured the average nuclear area and NCR of cervical squamous epithelium *in vivo* using a fiber optic confocal reflectance microscope [123]. Another study done previously by Collier using a non-fibered confocal reflectance microscope measured the NCR of cervical tissue *ex vivo* [67]. A quantitative comparison, shown in Fig 24, shows that the *ex vivo* results exhibit higher NCR. Greater average nuclear area from *ex vivo* results was attributed to possible shrinkage after biopsy. A third set of data obtained by Walker is also shown from a NCR study conducted on histology sections [124]. One possibility stated as a reason for differences in NCR between the *in vivo* and *ex vivo* confocal microscopy experiments is tissue shrinkage; however, this has not yet been validated.

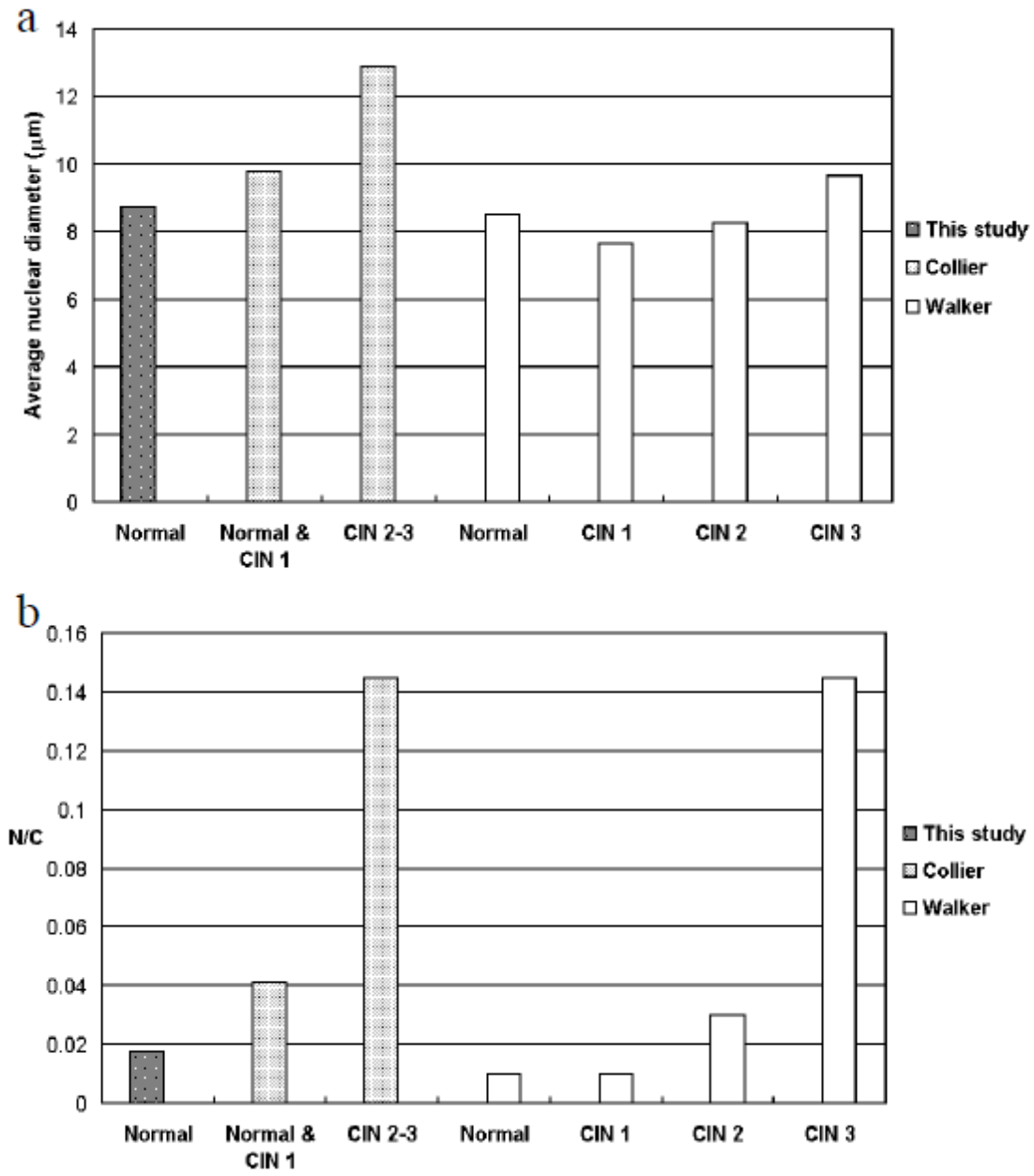

Fig 24. A comparison of the (a) average nuclear diameter and (b) NCR for confocal images acquired *in vivo* [123] and *ex vivo* [67], and histology [124].

There are significant functional differences in the confocal system design of the two aforementioned NCR experiments. Some of the notable differences potentially affecting a valid comparison of NCR values include the illumination source used, which

directly affects the lateral and axial resolutions. Also, the experiment conducted by Sung was performed *in vivo* versus an *ex vivo* study performed by Collier. Sung's experimental system used a 1064 nm wavelength illumination source, a 30,000 optical element fiber bundle, with a lateral resolution of 1.6 μm and an axial resolution of 3-10 μm. Collier's setup had a 810 nm laser with a 25× 0.8 NA water immersion objective. This system achieved a lateral resolution of 0.8 μm and an axial resolution of 2-3 μm. Additionally, the data acquired in Collier's *ex vivo* study was taken at least 6 hours after excision. Based on these differences, it may be complicated to directly compare the measured NCR from the experiments, particularly if the NCR results are used to identify a cutoff threshold for differentiating normal from precancerous tissue. In Chapter 6, I evaluate the effect of axial resolution on epithelial images and NCR measurements. In Chapter 7, I detail experimental results that investigate the effects of tissue sample size and tissue degradation on the NCR measurements.

6.1.2 Nuclear-to-Cytoplasmic Ratio of Oral Epithelium

The epithelial NCR has a wide range of values depending on the study, the method of measurement, and the tissue site. Electron microscopy and stereological analysis were performed on normal buccal epithelial biopsies [125,126]. The epithelial thickness was reported as 0.48 mm, and stereological point counting techniques calculated a NCR of 0.03 for the granular layer or superficial area of the epithelium. Later, another study was done using punch biopsies, and similarly, the epithelial thickness was reported as 0.5 – 0.6 mm [126]. Another technique for measuring the NCR is to scrape the oral mucosa, smear the cells on a glass slide, and then stain the sample prior to imaging with

light microscopy [127]. The calculated NCR was reported as 0.023 in this study. These results along with results from other studies are summarized in Table 5, below.

Table 5. Summary of quantitative results from oral epithelial measurements.

Author (Ref)	Sample (Location)	Process	Epithelium Thickness	ND± SD	CD± SD	NA± SD	CA± SD	NCR ±SD
Landay [125]	Human cheek (granular layer)	Biopsies	0.48 mm					0.03
Landay [126]	Human buccal mucosa	Punch biopsies	0.5-0.6 mm					
Ogden [127]	Human buccal mucosa	Scrape, smear, stain				72.28 ±11.5	3098 ±766	0.023*
Jin [128]	Human cheek (spinous cells)	Histology sections				29.2 ±5.3		
	Human cheek (basal cells)					23.0 ±3.4		
White [129]	Human cheek (spinous cells)	Histology sections						0.12 ±0.02
	Human cheek (basal cells)							0.67 ±0.10
Ramaesh [130]	Human buccal mucosa	Scrape, smear, stain		8.36 ±0.49	51.78 ±0.11	54.89		0.026*
White [28]	Human lip (superficial layer)	*In vivo* confocal	242.9±30.2 µm					0.031 ±0.01
	Human lip	Histology sections	226.6±42.1 µm					0.049 ±0.021
De Arruda [131]	Human cheek	Scrape, smear, stain						0.03 ±0.01

Although spinous and basal cells are larger than granular cells, which lie in the superficial epithelium, their values for nuclear area and NCR are useful for comparison

when imaging deeper into the epithelium [128,129]. Some of the data reported in Table 5 is measured from histology slides. The extensive processing procedures for histology may alter the morphology of tissues, such as shrinkage, which may explain the higher measured values for NCR compared to *in vivo* measurements. *In vivo* confocal reflectance microscopy was performed on human oral lip mucosa [28]. A thorough table lists comparisons of NCR measured from confocal images versus histology sections. Measured from the superficial epithelium, the mean NCR and standard deviations from 25 readings are 0.031 ± 0.01 and 0.049 ± 0.021 for confocal and histology, respectively.

6.2 Materials and Methods

6.2.1 Custom System Design

In order to evaluate the effect of axial resolution on NCR, a custom reflectance confocal microscope system with variable NA was used [116]. Samples are illuminated by an 811 nm continuous wave laser (DL808-120-0, CrystaLaser, Reno, NV). The illumination light was raster scanned across the sample and focused through a 40×, 0.8 NA water immersion microscope objective (MRD07420, Nikon). Backscattered signal from the tissue was focused onto a pinhole placed in the conjugate image plane before being detected by a photomultiplier tube detector. System specifications include an approximate 625 μm diameter field of view, and lateral and axial resolution ranges of 0.65 – 2.2 μm and 4.5 - 17 μm, respectively.

6.2.2 Sample Preparation and Imaging

To compare the system effects on the NCR, human oral mucosa biopsies were imaged using a custom reflectance confocal microscope with variable axial

resolution [116]. Oral tissue collection and imaging protocols were approved by the Institutional Review Boards at Texas A&M University and TAMU – Baylor College of Dentistry, and written consent was obtained from study participants.

The axial resolution of the system was varied by changing the current setting to an electrically tunable lens. The current was set to a fixed value as vertical scans were performed for several current settings, 45, 50, 75, 90, 100, 113, 120, and 125 mA corresponding to 4.5, 5, 6, 8, 9, 9.5, 13, and 17 μm axial resolutions. Vertical image stacks of approximately 400 μm depth below the tissue surface were acquired with approximately a 2 - 4 μm step size from the same location for comparison of an increasing axial resolution, or thickening of the axial plane which may have an effect on the NCR. Four depths were selected (64 μm, 134 μm, 180 μm, and 232 μm) for NCR analysis at 5 different axial resolutions (4.5 μm, 6 μm, 9 μm, 13 μm, and 17 μm).

6.2.3 Image Analysis

Confocal image analysis was performed by the automated SCM algorithm developed in MATLAB that is capable of segmenting epithelial cell nuclei [117,132]. The images were analyzed post acquisition without any pre-processing with the exception of cropping images around areas of high segmentation, as necessary, in order to measure a more accurate NCR value. After analysis, the segmentation algorithm outputs an NCR value per image, object area for each object segmented, and the number of objects segmented per image. Image contrast was measured by taking the average mean intensity value for all segmented objects and dividing by the average background intensity value which accounts for pixels located 2 to 3 pixels outside SCM segmentation borders.

6.3 Results

As the axial resolution of the confocal reflectance microscope is increased, the optical sectioning thickness also increases. Cell layers within the epithelium have varying morphology where some cells are flatter than others. A larger optical section thickness is expected to allow for more cell layers to show up in the focal plane and increase the number of detected nuclei within a single confocal frame. More cell layers in the focal plane could increase the NCR per image frame depending on cell size, shape, and distribution throughout the epithelial layer. Although it was expected that NCR values would increase, the results from automated SCM segmentation do not show significant change with increasing axial resolution.

For the 64 μm and 134 μm imaging depths, NCR values exhibit an increase in value, then drop off significantly with increasing axial resolution at 13 μm and 17 μm. Due to poor image contrast, NCR measurements for 13 μm and 17 μm are not included in further analysis. The images analyzed at an axial resolution of 9 μm are where a change in NCR is expected.

The segmented objects average 8 µm in diameter. An axial resolution of 9 µm would possibly allow for more cell layers to enter the focal plane. With increasing axial resolution, it appears that NCR decreases from lack of segmentation due to poor image contrast. Similarly for increasing depth (180 µm and 232 µm), automated segmentation is not accurate at any axial resolution.

Fig 25 shows selected images of human tissue imaged at five different axial resolutions, 4.5 µm, 6 µm, 9 µm, 13 µm, and 17 µm. Specific imaging depths (64 µm, 134 µm, 180 µm, and 232 µm) were chosen to show how image quality degrades with increasing axial resolution and imaging depth. Fig 25(a), 25(b), 25(e), 25(f), 25(i), 25(j) have the most ideal contrast for automated nuclear segmentation with the SCM algorithm. Columns containing figures from 180 µm and 232 µm imaging depths did not provide any quantifiable information due to low contrast at increasing depths. The same is true for rows containing figures from 13 µm and 17 µm axial resolutions.

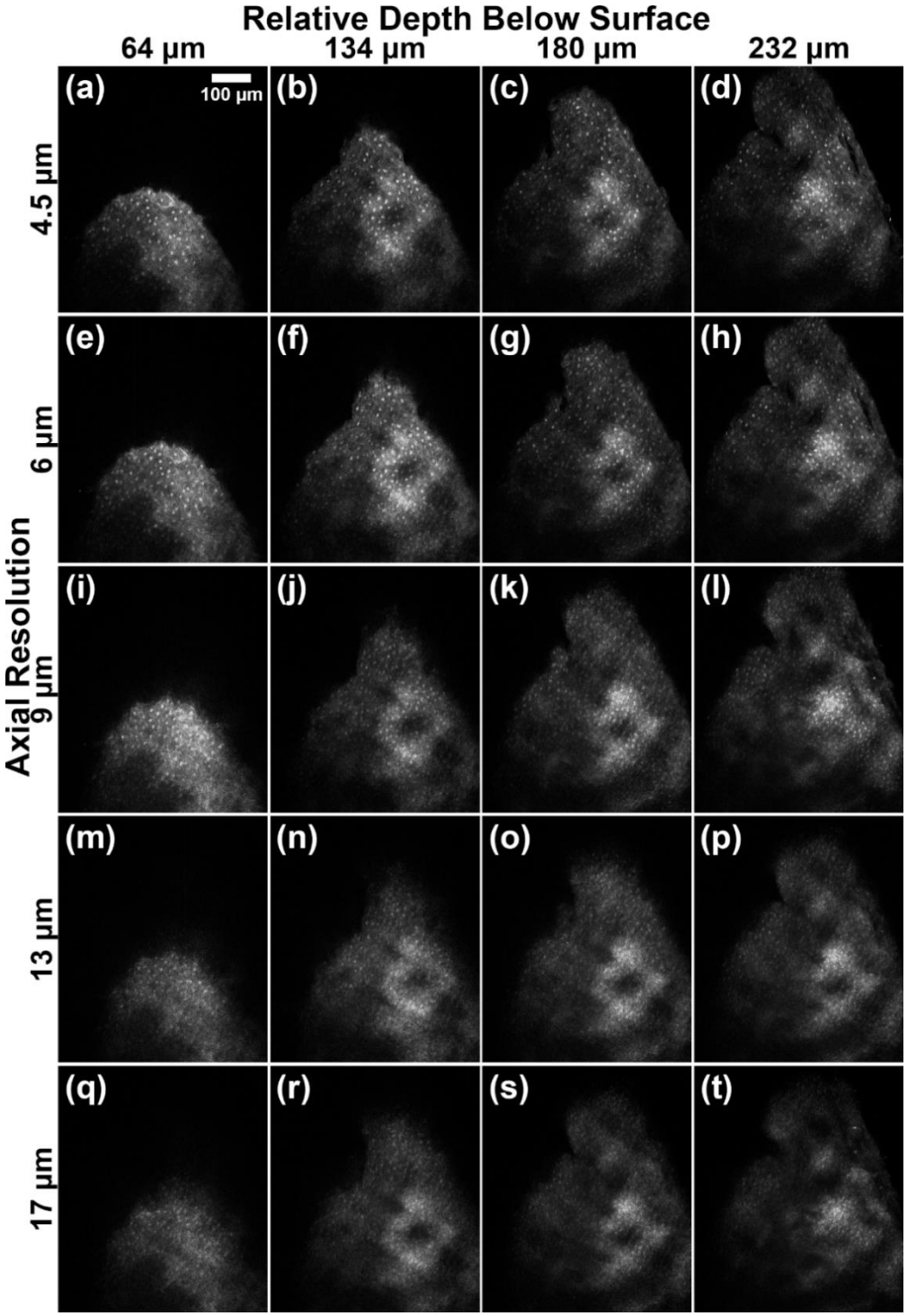

Fig 25. Comparison of selected image depths taken with varying axial resolution at the same location. Axial resolutions: (a – d) 4.5 µm, (e – h) 6 µm, (i – l) 9 µm, (m – p) 13 µm, and (q – t) 17 µm.

As axial resolution increases, more cell layers seem to enter the FOV as tissue approaches and passes through the focal plane, but contrast degradation makes it difficult to discern object borders. The images acquired at an axial resolution of 13 µm and 17 µm show significant contrast degradation making it difficult to accurately segment nuclei with an automated segmentation algorithm.

Fig 26 below, contains images from Fig 25(a), 25(e), 25(i), and 25(m) to show how significantly contrast varies between axial resolutions. All images are from approximately 64 µm below the tissue surface.

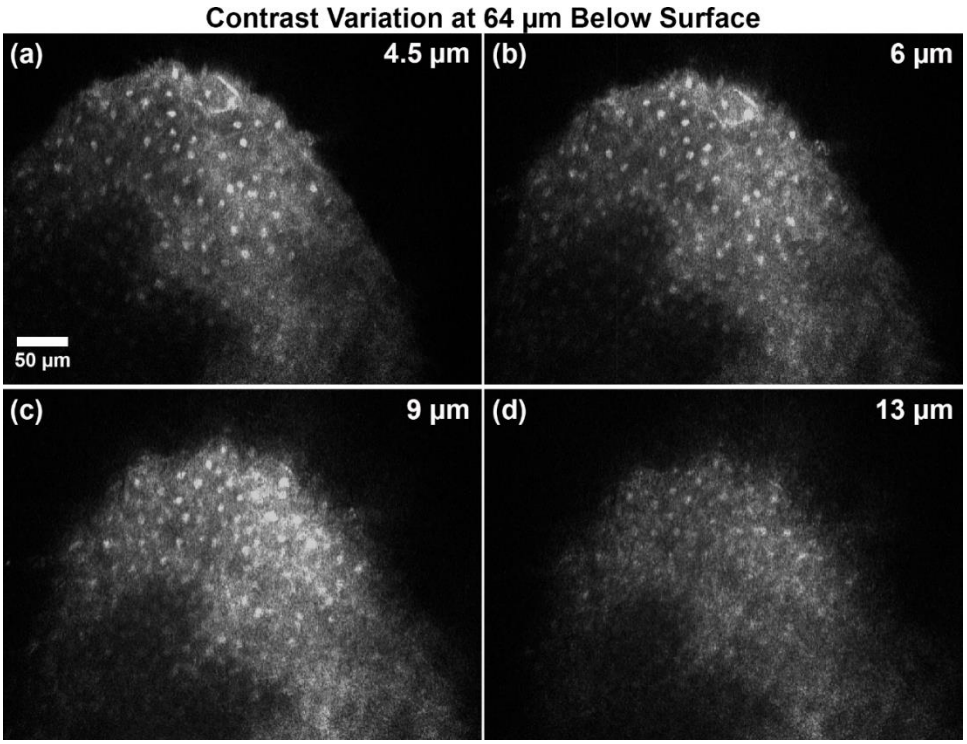

Fig 26. Comparison of contrast variation at 64 µm for various axial resolutions. Axial resolutions: (a) 4.5 µm, (b) 6 µm, (c) 9 µm, and (d) 13 µm.

Fig 26(a) and 26(b) look very similar and distinct features can be seen and correlated between both images, but Fig 26(b) shows an increased number of objects due to increased axial resolution. Fig 26(c) does appear brighter, but does not necessarily exhibit an increase in nuclear density. Although it is possible to visibly differentiate some nuclear objects in Fig 26(d), it is not possible to automatically segment this image due to poor contrast and loss of distinct object borders.

As shown in Table 6, as axial resolution increases, NCR increases at shallow depths (64µm and 134 µm). Contrast, measured for each area of segmented tissue, decreases as axial resolution increases. NCR was measured using an automated SCM algorithm with limitations in segmentation for images with contrast less than 1.85. Contrast values at axial resolutions of 9 µm and greater are significantly lower than the desired contrast for optical nuclear segmentation. Therefore, due to poor object segmentation at increased axial resolutions, NCR measurements do not effect quantitative results. Cell layers that are in focus are most likely segmented by the algorithm due to high contrast. Extra cell layers present due to increased axial resolution are not resolved and therefore are not segmented by the automated segmentation algorithm.

Table 6. Quantitative analysis for images in Fig 25.

Depth [µm]	Axial Res [µm]	Contrast	# Obj	NCR	Avg Area [µm]	Avg Diam [µm]
64	4.5	1.98	37	0.0574	47.51	7.78
	6	1.89	37	0.0629	48.08	7.82
	9	1.67	48	0.0595	43.79	7.47
134	4.5	2.06	58	0.0716	45.78	7.63
	6	1.87	85	0.0765	42.16	7.33
	9	1.71	23	0.0498	32.88	6.47
180	4.5	2.08	51	0.0048	36.88	6.85
	6	1.92	33	0.0032	37.17	6.88
	9	1.64	21	0.0015	28.22	5.99

6.4 Discussion

Axial resolution does not appear to have a significant effect on measured NCR. Image contrast directly effects SCM segmentation, which leads to a significantly lower NCR approximation due to lack of automated object detection for increased imaging depths and increased axial resolution. The automated SCM segmentation algorithm outputs an area value reported in microns per object detected. Using the average area of all objects in a single image, average object diameter was calculated which was less than 8 µm for all images. For an axial resolution of 9 µm, it is expected that this is where a change in NCR would most likely be observed. The measured NCR values remain fairly constant for axial resolutions of 4.5 µm, 6 µm, and 9 µm at 64 µm and 134 µm depths below the tissue surface.

7. EFFECTS OF TISSUE PROCESSING ON EPITHELIAL NUCLEAR-TO-CYTOPLASMIC RATIO MEASUREMENTS WITH REFLECTANCE CONFOCAL MICROSCOPY

7.1 Introduction

As described in 6.1, variations in NCR measurements and average area of nuclei are possibly attributed to tissue shrinkage after biopsy [123]. In this chapter are results that investigate the effects of the physical size of tissue samples and tissue degradation on the NCR measurements.

7.2 Materials and Methods

7.2.1 Commercial System Setup

To evaluate the effects of biopsy excision and autolysis on NCR, a commercial VivaScope 2500 inverted confocal microscope (Caliber I.D., Rochester, NY) was used to acquire large area images. Individual frame size provides a field of view (FOV) of 750 × 750 μm^2 at a rate of 9 frames per second, and automated image stacks and mosaicking allow easy expansion of the imaging area. With an 830 nm reflectance imaging wavelength, optical resolutions are 1.5 μm and 5 μm for lateral and axial planes, respectively.

7.2.2 Sample Preparation and Imaging

To compare the NCR of bulk porcine oral tissue to biopsy samples, porcine buccal mucosa was acquired via a tissue sharing program at Texas A&M University. Because the tissue was transferred from another study approved by the TAMU IACUC after the animal was terminated, review of this work by the TAMU IACUC is not required.

The porcine cheek tissue was harvested from a 4 month old piglet weighing 15 kilograms. After the buccal mucosa was excised from the oral cavity, it was transported to our research lab for imaging preparation. Prior to confocal reflectance imaging, the sample was submerged in acetic acid for 1 minute. The bulk sample was rinsed in PBS and then placed on the inverted confocal imaging system with the buccal mucosal surface facing down towards the microscope objective. A 7.5×7.5 mm^2 mosaic image was captured over a range of depth by imaging the bulk sample on the VivaScope 2500. The total imaging depth acquired was approximately 160 µm below the tissue surface with an 8 µm axial step size. A 0.5×0.5 mm^2 vertical stack was also acquired that has a total imaging depth of approximately 180 µm with a 5 µm axial step size. After imaging the bulk sample, three 3-mm biopsies were acquired from the oral tissue using a surgical punch. The biopsy locations cannot be correlated to the bulk tissue imaging location. The biopsies were imaged using manual laser power settings at each step on the VivaScope 2500 to avoid image saturation at biopsy edges. Square mosaics with areas of 4.5×4.5 mm^2 were acquired in sequence with a step size of approximately 8 µm up to a depth of 165 µm. Vertical stacks were also acquired of the biopsies with a field of view of 0.5×0.5 mm^2 up to approximately 180 µm below the tissue surface using a step size of 5 µm. A fourth biopsy was acquired using a scalpel and imaged with the same image acquisition parameters. In between biopsy excisions and imaging sessions, the bulk sample was stored in PBS in the fridge.

To study the effect of autolysis or cellular damage on NCR, buccal mucosa was acquired via another tissue sharing program at Texas A&M University. A previous

study was conducted to compare tissue preservation between PBS and Dulbecco's modified Eagle's medium (DMEM). Histopathological analysis determined that there was not a significant difference between the two types of media for short term tissue preservation. Edema was present in the first biopsies imaged with confocal microscopy, so it was determined that the next experiment would have a control sample and we would continue using PBS for sample preservation in between imaging sessions.

After euthanasia, the porcine buccal mucosa tissue was harvested. A large biopsy sample was removed from the cheek tissue and fixed immediately in formalin to serve as a control. This sample was not exposed to acetic acid or imaged using confocal microscopy. The remaining mucosal tissue was submerged in PBS and transported to the lab. Approximately 1.5 hours after euthanasia and 1 hour after tissue harvest, six porcine oral mucosa biopsies were removed from the bulk tissue sample and returned to the PBS solution to evaluate autolysis of biopsies over time. Prior to imaging, all samples were placed in 5% acetic acid for 30 seconds, followed by a PBS rinse. All samples were imaged using the VivaScope 2500 reflectance confocal microscope and then fixed in formalin for histology. The first biopsy sample taken in the lab is considered as Time 0. The other five samples were imaged consecutively every 30 minutes. Samples were stored in the fridge in between imaging sessions. Vertical stacks of each biopsy were acquired from 5 μm to 300 μm with an approximate step size of 5 μm. All biopsies were immediately stored in formalin after confocal imaging for fixation before histopathology analysis.

7.2.3 Image Analysis

Prior to analysis, the confocal reflectance images acquired with the commercial VivaScope 2500 were cropped to a circular region with a diameter of 450 μm in order to remove optical reflections at shallow depths. Cropping the outer edges of the confocal images would also help in automated analysis by ensuring the area of tissue analyzed is from a similar depth or image plane. Due to the field of curvature of the objective on the VivaScope 2500, the difference in tissue depth could vary as much as 25 μm from the center of the field of view to the corners of the image frame.

7.3 Results

7.3.1 Nuclear-to-Cytoplasmic Ratio Comparison of Bulk Tissue and Biopsy Measured with Reflectance Confocal Microscopy

Following automated nuclear segmentation using the SCM algorithm, all data from the imaged vertical stacks was organized into Table 7 below. The NCR and number of objects segmented at each depth are recorded for all samples imaged using reflectance confocal microscopy. A decrease in segmented objects in the deep layers may indicate loss of the capability of the segmentation algorithm to segment nuclei with reduced signal or nuclear to cytoplasmic contrast.

Table 7. Bulk and biopsy NCR and number of objects from SCM.

Sample	Bulk		Biopsy #1		Biopsy #2		Biopsy #3		Biopsy #4	
Depth [µm]	NCR	#Ob	NCR	#Ob	NCR	#Ob	NCR	#Ob	NCR	#Ob
0	0.0240	102	0.0179	57	0.0068	27	0.0031	14	0.0004	3
5	0.0235	101	0.0104	50	0.0070	28	0.0152	54	0.0103	31
10	0.0195	88	0.0128	58	0.0176	55	0.0238	72	0.0223	62
14	0.0190	76	0.0214	83	0.0180	57	0.0305	79	0.0400	89
19	0.0217	86	0.0203	65	0.0209	68	0.0281	82	0.0517	116
24	0.0164	68	0.0209	79	0.0242	72	0.0296	90	0.0467	105
29	0.0199	74	0.0206	77	0.0249	79	0.0395	108	0.0474	109
33	0.0222	78	0.0224	79	0.0215	79	0.0463	106	0.0370	84
38	0.0226	77	0.0247	81	0.0245	77	0.0383	97	0.0250	68
43	0.0274	87	0.0249	85	0.0245	73	0.0432	98	0.0337	79
48	0.0314	94	0.0313	95	0.0274	76	0.0454	100	0.0352	77
52	0.0349	93	0.0335	95	0.0260	74	0.0450	107	0.0360	80
57	0.0349	95	0.0377	109	0.0258	62	0.0429	89	0.0273	66
62	0.0340	91	0.0350	111	0.0241	55	0.0401	78	0.0336	79
65	0.0383	102	0.0363	106	0.0304	77	0.0336	72	0.0323	81
70	0.0403	107	0.0399	112	0.0256	57	0.0285	66	0.0303	75
75	0.0439	118	0.0451	124	0.0250	57	0.0326	66	0.0426	90
79	0.0433	109	0.0501	132	0.0224	46	0.0367	73	0.0436	91
82	0.0497	123	0.0516	138	0.0216	46	0.0302	60	0.0377	82
87	0.0498	114	0.0545	128	0.0202	41	0.0298	60	0.0339	80
92	0.0498	118	0.0547	133	0.0122	34	0.0236	50	0.0484	98
95	0.0552	122	0.0598	131	0.0099	26	0.0236	49	0.0477	103
100	0.0539	113	0.0682	142	0.0144	32	0.0229	45	0.0376	85
105	0.0502	108	0.0693	145	0.0138	31	0.0238	50	0.0301	71
108	0.0380	84	0.0660	132	0.0100	25	0.0217	44	0.0398	89
113	0.0286	65	0.0599	123	0.0070	16	0.0236	49	0.0245	60
117	0.0291	66	0.0599	118	0.0088	20	0.0184	42	0.0203	51
120	0.0227	54	0.0536	107	0.0085	20	0.0228	44	0.0306	66
125	0.0158	36	0.0420	90	0.0094	20	0.0219	45	0.0257	57
130	0.0130	29	0.0425	86	0.0054	10	0.0185	38	0.0180	47
135	0.0116	28	0.0339	69	0.0054	10	0.0185	39	0.0164	39
139	0.0101	23	0.0288	63	0.0052	12	0.0163	35	0.0111	31
144	0.0059	16	0.0212	43	0.0040	7	0.0136	27	0.0147	36
149	0.0061	14	0.0226	47	0.0057	11	0.0101	22	0.0145	36
154	0.0059	15	0.0167	36	0.0046	9	0.0104	22	0.0050	13
159	0.0054	12	0.0142	31	0.0027	5	0.0116	25	0.0051	15
163	0.0035	7	0.0104	21	0.0038	7	0.0048	11	0.0040	12
168	0.0029	9	0.0135	26	0.0024	5	0.0060	13	0.0027	7
173	0.0010	4	0.0081	17	0.0007	2	0.0092	18	0.0012	4
178	0.0013	3	0.0061	15	0.0000	0	0.0055	13	0.0006	2
182	0.0029	6	0.0052	13	0.0000	0	0.0021	5	0.0011	3

In order to illustrate any effect of tissue biopsy, the measured NCR is plotted with increasing imaging depth in Fig 27 below. The bulk sample imaged shows a positive NCR trend, but begins to decrease around 100 µm below the tissue surface, possibly due to reduced nuclear segmentation. The biopsy that most closely follows the NCR trend for the bulk sample is biopsy #1. At approximately 100 µm, there is a peak in NCR value for biopsy #1, followed by a decreasing trend. As seen in the table and the plot, biopsy #2 has significantly lower NCR values than the other samples. This is evident in the images where low contrast and high scattering from artifacts make it difficult to automatically segment the epithelial nuclei. Both biopsy #3 and #4 exhibit an increase in NCR at more shallow depths than the other samples; however, this may be attributed to inaccurate identification or positioning of the tissue surface during imaging. Vertical stack images from biopsy #3 show a rete ridge, which is highly reflective, causing the SCM segmentation algorithm to detect false positives. As depth increases, the contrast worsens more quickly for this sample than the others. Biopsy #4 was removed from the bulk tissue sample using a scalpel, rather than a punch biopsy tool. This piece of tissue was slightly larger than the others, but was removed last from the bulk sample and therefore imaged last leaving more time for possible tissue degradation. The data shows a peak in NCR at shallow depths. The confocal images are highly reflective at lower depths, possibly causing false positives to be segmented and increasing the size of the object detected. Larger object sizes correlate with an increase in NCR. Like all the other samples, the NCR drops significantly with increasing imaging depth below the tissue surface.

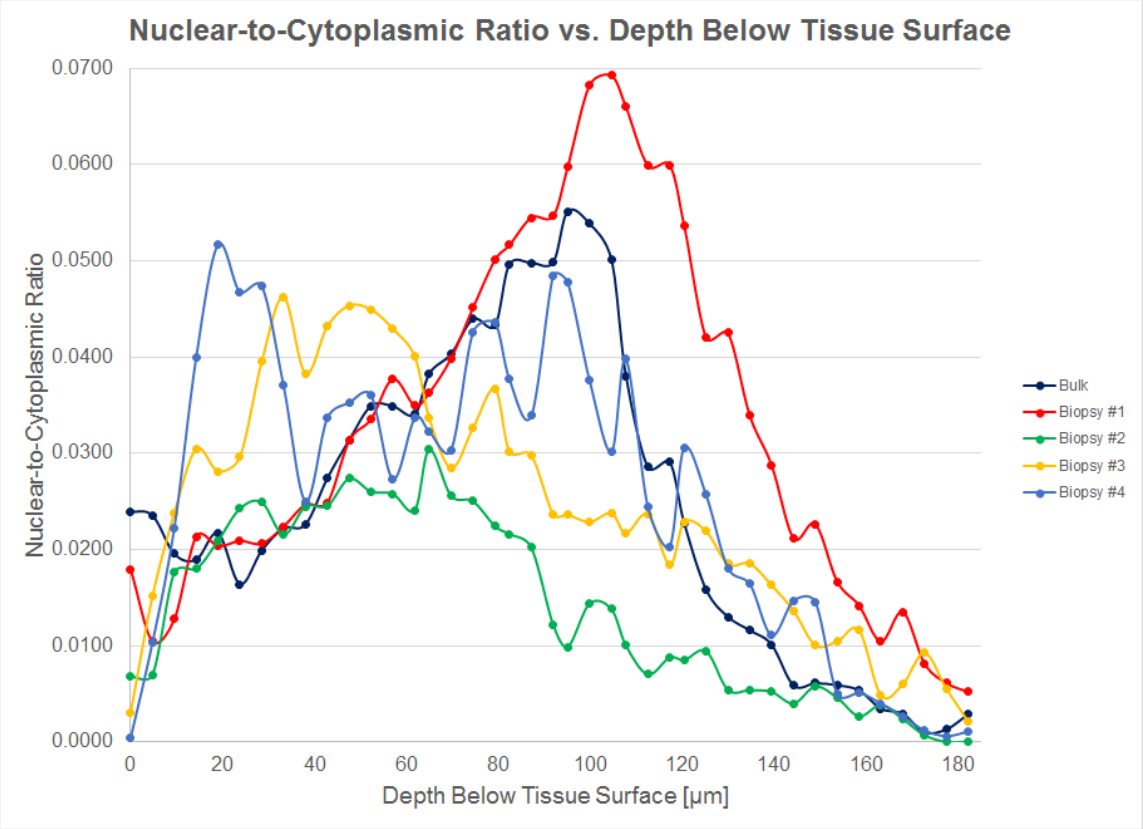

Fig 27. Nuclear-to-cytoplasmic ratio measured by SCM segmentation of confocal images versus depth below tissue surface for bulk and biopsied epithelial tissue.

Table 8 below lists the average area and standard deviation for the bulk tissue sample and all four biopsies excised by either a 3 mm punch biopsy (biopsies #1 - #3) or a scalpel (biopsy #4).

Table 8. Bulk and biopsy average area and standard deviation from SCM.

Sample	Bulk		Biopsy #1		Biopsy #2		Biopsy #3		Biopsy #4	
Depth [µm]	Avg Area	± SD	Avg Area	± SD	Avg Area	± SD	Avg Area	± SD	Avg Area	± SD
0	35.14	23.72	49.13	31.69	39.85	22.73	32.67	13.63	20.44	6.87
5	35.33	25.80	32.69	24.34	39.35	28.03	42.61	24.08	52.51	26.69
10	33.88	23.37	34.46	25.72	49.85	33.04	50.41	28.33	55.85	26.62
14	38.60	27.15	39.94	28.52	48.98	31.77	58.31	28.28	66.97	28.90
19	39.06	28.25	48.69	31.85	47.74	27.56	52.15	28.11	66.86	29.63
24	37.66	25.03	41.11	27.41	52.22	29.21	50.29	28.27	67.32	32.78
29	41.85	26.40	41.71	26.32	48.89	29.57	55.55	32.16	65.84	30.05
33	44.20	27.51	44.05	26.44	42.44	26.33	65.85	32.61	67.54	29.90
38	45.59	26.43	47.27	24.94	49.31	29.15	60.13	31.03	56.99	30.54
43	48.72	27.32	45.39	23.24	52.14	23.75	67.02	30.07	65.53	28.99
48	51.43	25.55	50.76	28.65	55.72	25.28	68.84	31.01	70.29	27.63
52	57.65	27.72	54.30	27.99	54.46	25.70	63.73	30.45	69.12	27.41
57	56.37	24.03	53.02	26.78	64.43	29.18	73.48	31.33	64.06	26.21
62	57.40	24.98	48.39	23.35	67.94	27.51	78.40	26.86	65.47	28.08
65	57.38	26.79	52.54	26.68	60.91	27.00	71.72	28.45	61.33	27.93
70	57.50	28.65	54.42	25.77	69.55	28.29	66.68	29.83	62.40	24.83
75	56.59	28.50	55.34	27.19	68.07	27.25	76.07	27.40	72.16	24.99
79	60.36	26.02	57.43	27.31	75.84	25.90	77.10	28.97	72.95	23.83
82	61.00	26.46	56.56	28.31	73.08	27.85	77.67	25.92	70.40	24.07
87	66.01	27.97	64.18	27.43	76.75	26.70	76.61	28.76	65.15	23.37
92	63.81	30.86	61.94	27.91	56.30	25.83	73.45	25.86	74.94	23.34
95	67.95	26.99	68.44	28.68	59.65	26.56	74.82	24.74	70.32	24.32
100	71.74	26.94	71.52	26.22	70.33	24.11	78.95	25.54	67.75	21.53
105	70.09	27.44	71.01	28.52	69.66	22.97	73.83	28.82	65.51	19.62
108	69.14	26.49	74.57	26.98	62.82	24.95	76.69	24.42	68.31	22.43
113	67.76	24.78	73.05	27.58	68.87	20.49	74.94	26.44	63.25	19.26
117	67.90	28.79	76.19	24.47	68.93	29.29	68.45	30.95	62.05	19.41
120	65.23	26.34	75.64	26.96	66.74	29.30	80.68	27.81	71.41	22.84
125	68.73	25.79	71.22	26.78	73.97	28.77	75.68	24.02	69.81	18.70
130	70.20	22.92	75.37	23.07	85.39	34.84	75.95	24.31	59.97	15.01
135	64.95	23.01	75.55	23.24	84.88	35.22	74.19	25.38	65.80	22.72
139	68.99	27.08	70.54	28.36	68.34	33.37	72.72	25.99	56.16	17.39
144	57.87	21.16	76.68	23.64	90.40	22.06	79.21	22.08	63.88	19.16
149	68.63	24.28	74.90	24.50	82.59	19.40	71.92	25.14	63.27	19.90
154	61.95	28.41	72.34	18.62	80.63	35.09	74.74	27.42	60.53	18.29
159	70.41	26.86	71.67	22.77	84.60	26.21	73.04	25.03	53.89	15.12
163	78.11	30.61	78.16	22.09	86.46	24.37	69.29	16.00	52.83	20.73
168	51.31	19.75	81.54	23.90	75.38	15.46	72.95	12.32	60.83	16.97
173	39.80	12.69	75.44	19.41	55.13	3.98	80.91	21.00	47.39	8.12
178	69.19	42.79	64.35	16.65	0	0	67.02	24.47	48.09	3.58
182	76.22	31.73	63.04	18.05	0	0	66.60	30.42	56.81	19.97

Fig 28 below illustrates the data listed in Table 8 above. As expected and seen with NCR, the bulk sample and biopsy #1 are similar in average area of detected objects per imaging depth. The spike in average area for biopsy #2 and lower measured NCR values could indicate that larger artifacts are detected by the SCM algorithm, but at a lesser rate. This is confirmed in Table 7 by comparing the lesser number of objects detected than the other samples. Biopsies #3 and #4 have consistently higher average areas than the other samples. Biopsy #3 remains fairly consistent in average area after 120 µm where biopsy #4 shows a decrease in value.

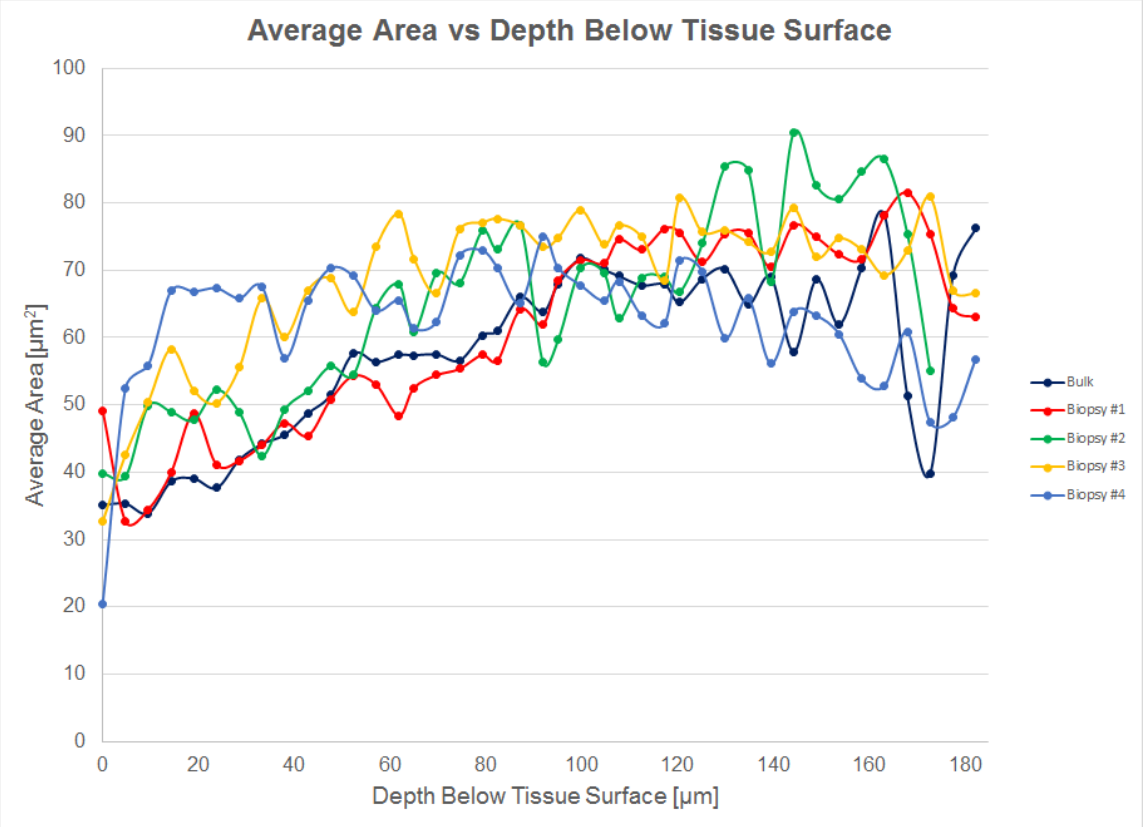

Fig 28. Average nuclear area versus depth below tissue surface for bulk and biopsied epithelial tissue.

In order to validate that a single vertical stack through the bulk sample was representative of the entire bulk sample, an area of 3 by 3 images or 2.25 mm × 2.25 mm was analyzed over multiple depths with SCM segmentation. Due to artifacts and a varying range of depth across the sample at a single image plane, a smaller localized mosaic is more accurate than averaging across the entire 7.5 mm × 7.5 mm area. In comparison to the single vertical stack, the averaged data has a similar shape and peak, indicating that the vertical stack is representative of the bulk sample. The difference between the two curves is that the averaged data is left shifted so the NCR peaks at a more shallow depth, likely due to variation from where the vertical stack was captured. All of the vertical stacks begin at an approximate depth of 0 μm relative to the tissue surface, ensuring a better comparison of data.

7.3.2 Nuclear-to-Cytoplasmic Ratio Comparison of Autolysis in Porcine Oral Mucosa Stored in PBS Measured with Reflectance Confocal Microscopy

Following automated nuclear segmentation using the SCM algorithm, all data was organized into Table 9 below showing measured NCR and number of segmented objects for each time point from 0 to 2.5 hours after biopsy removal from bulk tissue.

Table 9. Biopsy NCR and number of objects compared over time.

Time [Hrs]	0		0.5		1		1.5		2		2.5	
Depth [µm]	NCR	# Ob	NCR	# Ob	NCR	# Ob	NCR	# Ob	NCR	# Ob	NCR	# Ob
5	0.0057	64	0.0011	17	0.0023	31	0.0018	27	0.0021	32	0.0039	62
24	0.0030	50	0.0027	31	0.0035	43	0.0022	29	0.0055	60	0.0036	67
43	0.0039	54	0.0025	35	0.0033	39	0.0028	34	0.0055	48	0.0025	44
62	0.0029	41	0.0031	43	0.0042	49	0.0042	54	0.0035	26	0.0023	23
81	0.0041	46	0.0035	39	0.0039	45	0.0042	45	0.0008	7	0.0014	15
100	0.0046	54	0.0026	34	0.0041	45	0.0045	53	0.0014	9	0.0012	9
119	0.0053	61	0.0031	37	0.0038	40	0.0040	46	0.0015	11	0.0003	3
138	0.0042	44	0.0056	62	0.0044	47	0.0043	44	0.0009	10	0.0008	7
157	0.0042	43	0.0061	60	0.0041	39	0.0039	43	0.0010	11	0.0005	4
176	0.0055	48	0.0059	57	0.0045	42	0.0034	39	0.0006	7	0.0004	3
195	0.0067	60	0.0065	61	0.0039	38	0.0033	36	0.0003	3	0.0005	4
214	0.0077	67	0.0066	54	0.0051	52	0.0029	35	0.0000	2	0.0005	4
233	0.0051	50	0.0081	66	0.0040	45	0.0024	28	0.0001	1	0.0002	2
252	0.0052	55	0.0058	54	0.0019	22	0.0016	23	0.0000	0	0.0001	1
271	0.0014	20	0.0052	52	0.0007	9	0.0013	18	0.0002	2	0.0000	0

Fig 29 shows the measured NCR values versus the approximate depth below the tissue surface for all time points. The first three data points in depth are excluded from the following charts due to inconsistencies in measurements caused by tissue artifacts near the surface. In Fig 29, samples imaged at time 0 hours and time 0.5 hours show an increasing trend in NCR with increasing depth before dropping off at depths greater than 225 µm. Times 1 and 1.5 hours appear more consistent in measured NCR from 60 µm to 175 µm where both exhibit decreasing NCR values as depth increases. At increased

periods of time in between imaging and biopsy excision, cellular and tissue features become more challenging to automatically segment with the SCM algorithm due to poor contrast and resolution. Times 2 and 2.5 hours have lower initial NCR values than times 0 and 0.5 hours and both show a decreasing trend in NCR over increasing depth due to this loss of segmentation ability.

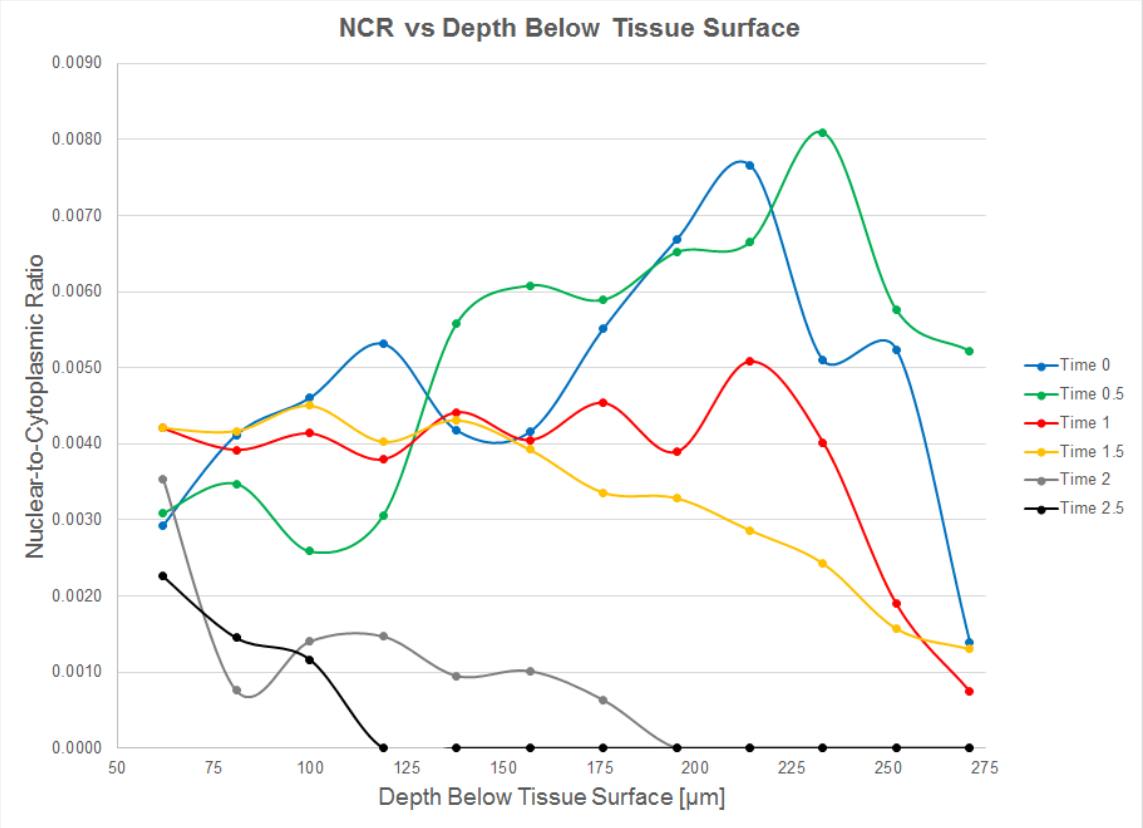

Fig 29. Measured nuclear-to-cytoplasmic ratio with depth below tissue surface over 2.5 hours from time of biopsy from bulk tissue.

The average nuclear area listed in Table 10 is calculated by adding up the area of all objects segmented in a single image and then dividing by the total number of objects segmented per frame. Figure 30 shows a plot of average nuclear area in square microns versus depth below the tissue surface in microns. Times 0, 0.5, 1, and 1.5 hours

all show consistent average areas of objects that gradually increase with increasing imaging depth. This correlates to the cellular structure of epithelial tissues. After 225 µm, the average nuclear area appears to decrease, likely due to decreasing image contrast, leading to fewer and smaller objects segmented as nuclear borders become more challenging to segment. Times 2 and 2.5 hours having initially higher average areas per object and exhibit a spike near the 100 µm depth below the tissue surface. Due to degradation of image contrast and tissue quality, this is likely attributed to artifacts detected by the automated segmentation algorithm which may appear similar to nuclei.

Table 10. Biopsy average area and standard deviation from SCM segmentation over time.

Time [Hrs]	0		0.5		1		1.5		2		2.5	
Depth [µm]	Avg Area	± SD	Avg Area	± SD	Avg Area	± SD	Avg Area	± SD	Avg Area	± SD	Avg Area	± SD
5	49.86	26.29	37.75	22.62	41.08	17.66	36.96	20.85	36.67	29.07	34.86	21.35
24	33.57	18.63	49.48	27.70	46.24	25.12	41.76	20.47	51.01	31.69	30.10	21.11
43	40.69	24.44	40.02	24.25	47.45	20.46	46.31	22.16	64.43	28.46	31.54	23.93
62	40.02	25.90	40.24	21.60	48.05	25.43	43.65	21.13	76.35	31.97	55.08	32.51
81	50.15	26.81	49.92	28.05	48.81	20.32	51.86	24.38	60.59	26.47	54.23	27.82
100	47.73	22.26	42.67	21.85	51.50	22.38	47.54	26.21	87.44	24.13	72.63	28.41
119	48.74	22.49	46.29	23.29	53.20	21.94	49.04	21.55	74.97	22.97	54.00	16.34
138	53.18	16.30	50.33	25.25	52.60	19.53	54.86	21.41	53.38	21.04	63.80	23.86
157	54.16	18.61	56.66	26.47	58.18	17.34	51.11	22.50	51.75	31.96	68.63	15.03
176	64.21	19.97	57.80	24.29	60.51	18.91	48.27	17.25	50.87	23.85	74.81	30.25
195	62.23	21.27	59.71	25.46	57.42	15.09	51.16	20.04	50.06	23.10	71.16	15.97
214	63.86	22.48	68.81	21.62	54.71	21.48	45.87	20.53	13.78	1.99	76.78	21.98
233	57.06	19.18	68.40	24.09	50.03	21.96	48.60	18.36	83.81	0.00	59.91	9.94
252	53.29	16.79	59.64	24.40	48.32	16.59	38.30	13.65	0	0	50.63	0.00
271	39.18	12.90	56.16	23.32	46.50	18.80	40.53	17.09	47.53	9.15	0	0

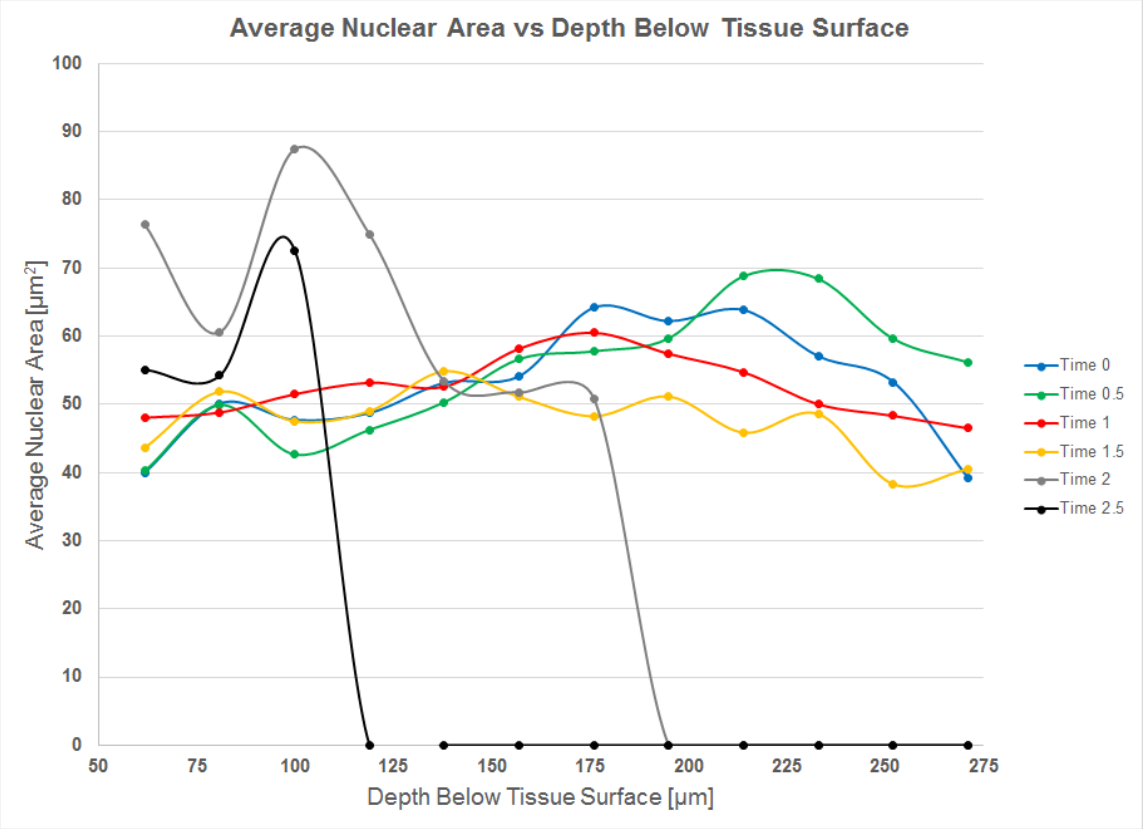

Fig 30. Average nuclear area with depth below tissue surface over 2.5 hours from biopsy.

After all samples were imaged and placed in formalin for fixation, they were mailed to Dr. Yi-Shing Lisa Cheng, dental pathologist at the Texas A&M University Health Science Center – Baylor College of Dentistry, for histopathological analysis. Her observations are noted in Table 11 below.

Table 11. Histopathology analysis of biopsies from autolysis experiment.

Sample/Time [Hours]	Histopathology Analysis
Control – 1	The tissue looked well preserved.
Control – 2	The tissue looked well preserved.
Time 0	Intra-cellular edema in the spinous cell layer, basal cell alterations and dissolution of the basement membrane noted.
Time 0.5	Intra-cellular edema and mild changes in the basal cells and basement membrane noted.
Time 1.0	Same as Time 0.5. Basal cell and basement membrane changes noted in focal areas.
Time 1.5	Same as Time 0.
Time 2.0	Same as Time 0.
Time 2.5	Same as Time 0.

Two cuts were made in the control piece of tissue for histopathological analysis. The two samples, Control 1 and Control 2, were most well preserved out of all samples. The sample imaged at Time 0 hours exhibited intra-cellular edema and dissolution of the basement membrane. Similarly for Time 0.5 hours, intra-cellular edema was also noted as well as changes in the basal cells and basement membrane. Time 1.0 hour looked similar to Time 0.5 with noted basal cell and basement membrane changes. As seen in the confocal images both qualitatively and quantitatively, image degradation was most severe at times 2 and 2.5 hours. Dr. Cheng noted that the cellular changes were all subtle and it was inconclusive if these changes would interfere with the interpretation for dysplasia or not when dysplasia is present. The epithelium appeared normal for all samples. The tissue showed slight cellular alteration that potentially all pathologists would be able to tell were due to sub-optimal tissue preservation.

7.4 Discussion

Although there were only slight changes in average area between bulk and biopsied samples, the NCR values for all samples showed greater variability. The NCR values for the bulk sample showed a consistently increasing trend for a greater imaging depth than the biopsy samples. This may be attributed to the fact that the bulk sample was imaged first, and therefore had less time for autolysis to occur. However, the variation in localized tissue structure, such as rete ridges, appears to have the greatest effect on the measured NCR. Therefore, the difference in measured NCR of bulk tissue compared to tissue biopsies is not found to be substantial in this small sample size. Further experiments with mucosal tissue from multiple animals and multiple imaging locations are needed to test for significance.

If fixed immediately after biopsy excision, epithelial tissue seems to remain intact and appears normal for histopathological diagnosis. Increased tissue manipulation and a delay in fixation resulted in degradation of epithelial structure. This typically led to intra-cellular edema with changes in the spinal cells, basal cells, and possible dissolution of the basement membrane. For reflectance confocal microscopy of epithelial cells, an increased delay in imaging post-biopsy resulted in decreased contrast and eventual inability to automatically segment cell nuclei using the SCM segmentation algorithm. Imaging within 1.5 hours post-biopsy appeared to have no significant effect on segmentation and NCR measurement.

8. CONCLUSIONS

A fluorescence and reflectance confocal microscope capable of imaging in beam scanning and rapid stage scanning modalities was designed and constructed for preclinical studies of epithelial tissues. Compared to other custom and commercial systems, the length of our images and speed of acquisition are significantly higher. The image acquisition speed is currently limited by the maximum speed of the translation stage. Use of a faster stage would further increase image acquisition speed to the point that the polygon scanning mirror, our fast axis line scanner, would be the limiting factor. The acquisition of image stacks is currently limited by data transfer and saving, and not limited by the translation stage.

Large area microscopy is demonstrated on excised mouse colon for qualitative evaluation of induced inflammation along the length of the colon. Normal mouse colon structure exhibited homogeneous distribution of colon crypts along the entire length of the colon. Mouse colon tissue with induced inflammation exhibited loss of structure, and varying crypt size, shape, and distribution. Since regions of the inflamed mouse colon appeared as normal, a rapid stage scanning image technique to evaluate the entire organ to identify regions of interest may be valuable.

Automated segmentation of epithelial tissue nuclei is conducted by the developed SCM algorithm. The PCNN based algorithm was developed in MATLAB and outputs quantitative measurements such as area and eccentricity of each segmented object with standard deviations. The NCR, total number of objects segmented, averages for area and

eccentricity are also reported for each image in a separate file. The SCM code has a graphical user interface to make image processing fast and easy. Multiple images may be uploaded at once for continuous processing and optional automatic saving of the segmented images and raw data. The algorithm was validated on generated confocal images with epithelial tissue properties and then tested on porcine and human oral mucosa.

Axial resolution does not appear to have a significant effect on NCR. Image contrast directly affects SCM segmentation, which leads to a significantly lower NCR approximation due to lack of automated object detection for increased imaging depths and increased axial resolution. The automated SCM segmentation algorithm outputs an area value reported in microns per object detected. Using the average area of all objects in a single image, average object diameter was calculated which was less than 8 μm for all images. For an axial resolution of 9 μm, it is expected that this is where a change in NCR would most likely be observed. The measured NCR values remain fairly constant for axial resolutions of 4.5 μm, 6 μm, and 9 μm at 64 μm and 134 μm depths below the tissue surface. Object size does not vary much with increasing axial resolution or with increasing depth. The average diameters are all less than 8 um, which could mean that at an axial resolution of 9 um, more cell layers are observed in the focal plane thickness. Since the NCR values remain relatively constant, it is concluded that optical imaging systems with increased axial resolution have comparable quantitative analysis measurements to other confocal imaging systems with lesser axial resolutions.

Average nuclear area measurements of bulk tissue and biopsy samples were comparable. NCR measurements did not appear to be significantly affected by the physical

size of a tissue sample – 3 mm biopsy, shave biopsy, or bulk tissue. However, the small sample size and variation of tissue structure limit the strength of this finding.

If fixed immediately after biopsy excision, epithelial tissue seems to remain intact and appears normal for histopathological diagnosis. Minor changes to tissue structure were observed in histopathology with increased tissue handling and time to fixation. With an increased time delay from biopsy to imaging, confocal imaging of epithelium had reduced nuclear to cytoplasmic contrast. This loss of contrast resulted in limited automatic segmentation and NCR measurement.

REFERENCES

1. Jemal A, Bray F, Center MM, Ferlay J, Ward E, Forman D. Global cancer statistics. CA Cancer J Clin. (2011); 61: 69-90.

2. Franco EL, Rohan TE. Cancer precursors: epidemiology, detection, and prevention. New York, NY: Springer. (2002).

3. Pawley JB. Handbook of biological confocal microscopy. New York, NY: Springer. (2006).

4. Jabbour JM, Saldua MA, Bixler JN, Maitland KC. Confocal Endomicroscopy: Instrumentation and Medical Applications. Ann Biomed Eng. (2011): 378-397.

5. Saldua MA, Olsovsky CA, Callaway ES, Chapkin RS, Maitland KC. Imaging inflammation in mouse colon using a rapid stage-scanning confocal fluorescence microscope. J Biomed Opt. (2012); 17: 0160061-0160067.

6. Abeytunge S, Li Y, Larson B, Toledo-Crow R, Rajadhyaksha M. Rapid confocal imaging of large areas of excised tissue with strip mosaicing. J Biomed Opt. (2011); 16: 050504-050504.

7. Jabbour JM, Cheng S, Malik BH, Cuenca R, Jo JA, Wright J, et al. Fluorescence lifetime imaging and reflectance confocal microscopy for multiscale imaging of oral precancer. J Biomed Opt. (2013); 18: 046012-046012.

8. Kester RT, Tkaczyk TS, Descour MR, Christenson T, Richards-Kortum R. High numerical aperture microendoscope objective for a fiber confocal reflectance microscope. Opt Express. (2007); 15: 2409-2420.

9. Tabatabaei N, Kang D, Wu T, Kim M, Carruth RW, Leung J, et al. Tethered confocal endomicroscopy capsule for diagnosis and monitoring of eosinophilic esophagitis. Biomed Opt Express. (2013); 5: 197-207.

10. Jeong J-W, Kim S, Solgaard O. Split-frame gimbaled two-dimensional MEMS scanner for miniature dual-axis confocal microendoscopes fabricated by front-side processing. Journal of Microelectromechanical Systems. (2012); 21: 308-315.

11. Meining A, Saur D, Bajbouj M, Becker V, Peltier E, Höfler H, et al. In vivo histopathology for detection of gastrointestinal neoplasia with a portable, confocal miniprobe: an examiner blinded analysis. Clinical Gastroenterology and Hepatology. (2007); 5: 1261-1267.

12. Polglase AL, McLaren WJ, Skinner SA, Kiesslich R, Neurath MF, Delaney PM. A fluorescence confocal endomicroscope for in vivo microscopy of the upper- and the lower-GI tract. Gastrointest Endosc. (2005); 62: 686-695.

13. Wu K, Liu JJ, Adams W, Sonn GA, Mach KE, Pan Y, et al. Dynamic real-time microscopy of the urinary tract using confocal laser endomicroscopy. Urology. (2011); 78: 225-231.

14. Guitera P, Menzies SW, Longo C, Cesinaro AM, Scolyer RA, Pellacani G. In vivo confocal microscopy for diagnosis of melanoma and basal cell carcinoma using a two-step method: analysis of 710 consecutive clinically equivocal cases. Journal of Investigative Dermatology. (2012); 132: 2386-2394.

15. Nehal KS, Gareau D, Rajadhyaksha M. Skin imaging with reflectance confocal microscopy. Seminars in Cutaneous Medicine and Surgery. (2008); 27: 37-43.

16. Maitland KC, Gillenwater AM, Williams MD, El-Naggar AK, Descour MR, Richards-Kortum RR. In vivo imaging of oral neoplasia using a miniaturized fiber optic confocal reflectance microscope. Oral Oncol. (2008): 1059-1066.

17. Carlson K, Pavlova I, Collier T, Descour M, Follen M, Richards-Kortum R. Confocal microscopy: imaging cervical precancerous lesions. Gynecol Oncol. (2005); 99: S84-S88.

18. Tanbakuchi AA, Udovich JA, Rouse AR, Hatch KD, Gmitro AF. In vivo imaging of ovarian tissue using a novel confocal microlaparoscope. American journal of Obstetrics and Gynecology. (2010); 202: 90. e91-90. e99.

19. Boudoux C, Leuin S, Oh W, Suter M, Desjardins A, Vakoc B, et al. Preliminary evaluation of noninvasive microscopic imaging techniques for the study of vocal fold development. Journal of Voice. (2009); 23: 269-276.

20. Fuchs FS, Zirlik S, Hildner K, Schubert J, Vieth M, Neurath MF. Confocal laser endomicroscopy for diagnosing lung cancer in vivo. European Respiratory Journal. (2013); 41: 1401-1408.

21. Ragazzi M, Piana S, Longo C, Castagnetti F, Foroni M, Ferrari G, et al. Fluorescence confocal microscopy for pathologists. Modern Pathology. (2013); 27: 460-471.

22. Carlson AL, Coghlan LG, Gillenwater AM, Richards-Kortum RR. Dual-mode reflectance and fluorescence near-video-rate confocal microscope for

architectural, morphological and molecular imaging of tissue. J Microsc. (2007); 228: 11-24.

23. Wilson T, Carlini AR. Size of the detector in confocal imaging systems. Optics Letters. (1987); 12: 227-229.

24. Müller M. Introduction to confocal fluorescence microscopy. Bellingham, Wash.: SPIE-The International Society for Optical Engineering. (2006).

25. Cavanagh HD, Petroll WM, Alizadeh H, He YG, McCulley JP, Jester JV. Clinical and diagnostic use of in vivo confocal microscopy in patients with corneal disease. Ophthalmology. (1993); 100: 1444-1454.

26. Corcuff P, Leveque JL. In vivo vision of the human skin with the tandem scanning microscope. Dermatology. (1993); 186: 50-54.

27. Rajadhyaksha M, Anderson RR, Webb RH. Video-rate confocal scanning laser microscope for imaging human tissues in vivo. Appl Opt. (1999); 38: 2105-2115.

28. White WM, Rajadhyaksha M, Gonzalez S, Fabian RL, Anderson RR. Noninvasive imaging of human oral mucosa in vivo by confocal reflectance microscopy. Laryngoscope. (1999); 109: 1709-1717.

29. Polglase A. A fluorescence confocal endomicroscope for in vivo microscopy of the upper- and lower-GI tract. Gastrointestinal Endoscopy. (2005); 62: 686-695.

30. Sakashita M, Inoue H, Kashida H, Tanaka J, Cho JY, Satodate H, et al. Virtual histology of colorectal lesions using laser-scanning confocal microscopy. Endoscopy. (2003); 35: 1033-1038.

31. Nakao M, Yoshida S, Tanaka S, Takemura Y, Oka S, Yoshihara M, et al. Optical biopsy of early gastroesophageal cancer by catheter-based reflectance-type laser-scanning confocal microscopy. J Biomed Opt. (2008); 13: 054043-054043.

32. Kiesslich R, Gossner L, Goetz M, Dahlmann A, Vieth M, Stolte M, et al. In vivo histology of Barrett's esophagus and associated neoplasia by confocal laser endomicroscopy. Clinical Gastroenterology and Hepatology. (2006); 4: 979-987.

33. Bajbouj M, Vieth M, Rosch T, Miehlke S, Becker V, Anders M, et al. Probe-based confocal laser endomicroscopy compared with standard four-quadrant biopsy for evaluation of neoplasia in Barrett's esophagus. Endoscopy. (2010); 42: 435-440.

34. Leong RW, Nguyen NQ, Meredith CG, Al-Sohaily S, Kukic D, Delaney PM, et al. In vivo confocal endomicroscopy in the diagnosis and evaluation of celiac disease. Gastroenterology. (2008); 135: 1870-1876.

35. Zambelli A, Villanacci V, Buscarini E, Lupinacci G, De Grazia F, Brambilla G, et al. Confocal laser endomicroscopy in celiac disease: Description of findings in two cases. Endoscopy. (2007); 39: 1018-1020.

36. Watanabe O, Ando T, Maeda O, Hasegawa M, Ishikawa D, Ishiguro K, et al. Confocal endomicroscopy in patients with ulcerative colitis. J Gastroenterol Hepatol. (2008); 23 Suppl 2: S286-290.

37. Howlader N, A. M. Noone MK, N. Neyman,, R. Aminou WW, S. F. Altekruse, C. L. Kosary,, J. Ruhl ZT, H. Cho, A. Mariotto, M. P. Eisner,, D. R. Lewis HSC, E. J. Feuer, K. A. Cronin,, Edwards. aBK. SEER Cancer Statistics Review. National Cancer Institute: Bethesda, MD. (2011).

38. Kiesslich R, Burg J, Vieth M, Gnaendiger J, Enders M, Delaney P, et al. Confocal laser endoscopy for diagnosing intraepithelial neoplasias and colorectal cancer in vivo. Gastroenterology. (2004); 127: 706-713.

39. Xie XJ, Li CQ, Zuo XL, Yu T, Gu XM, Li Z, et al. Differentiation of colonic polyps by confocal laser endomicroscopy. Endoscopy. (2011); 43: 87-93.

40. Kiesslich R, Goetz M, Burg J, Stolte M, Siegel E, Maeurer MJ, et al. Diagnosing Helicobacter pylori in vivo by confocal laser endoscopy. Gastroenterology. (2005); 128: 2119-2123.

41. Kitabatake S, Niwa Y, Miyahara R, Ohashi A, Matsuura T, Iguchi Y, et al. Confocal endomicroscopy for the diagnosis of gastric cancer in vivo. Endoscopy. (2006); 38: 1110-1114.

42. Sonn GA, Jones SN, Tarin TV, Du CB, Mach KE, Jensen KC, et al. Optical biopsy of human bladder neoplasia with in vivo confocal laser endomicroscopy. J Urol. (2009); 182: 1299-1305.

43. Drezek RA, Collier T, Brookner CK, Malpica A, Lotan R, Richards-Kortum RR, et al. Laser scanning confocal microscopy of cervical tissue before and after application of acetic acid. American Journal of Obstetrics and Gynecology. (2000); 182: 1135-1139.

44. Sung KB, Richards-Kortum R, Follen M, Malpica A, Liang C, Descour M. Fiber optic confocal reflectance microscopy: a new real-time technique to view nuclear morphology in cervical squamous epithelium in vivo. Opt Express. (2003); 11: 3171-3181.

45. Carlson K, Pavlova I, Collier T, Descour M, Follen M, Richardskortum R. Confocal microscopy: Imaging cervical precancerous lesions. Gynecologic Oncology. (2005); 99: S84-S88.

46. Tan J, Quinn MA, Pyman JM, Delaney PM, McLaren WJ. Detection of cervical intraepithelial neoplasia in vivo using confocal endomicroscopy. BJOG. (2009); 116: 1663-1670.

47. Gillenwater A, Papadimitrakopoulou V, Richards-Kortum R. Oral premalignancy: new methods of detection and treatment. Curr Oncol Rep. (2006); 8: 146-154.

48. Haxel BR, Goetz M, Kiesslich R, Gosepath J. Confocal endomicroscopy: a novel application for imaging of oral and oropharyngeal mucosa in human. Eur Arch Otorhinolaryngol. (2010); 267: 443-448.

49. Just T, Stave J, Boltze C, Wree A, Kramp B, Guthoff RF, et al. Laser scanning microscopy of the human larynx mucosa: a preliminary, ex vivo study. Laryngoscope. (2006); 116: 1136-1141.

50. Thiberville L, Moreno-Swirc S, Vercauteren T, Peltier E, Cave C, Bourg Heckly G. In vivo imaging of the bronchial wall microstructure using fibered confocal fluorescence microscopy. Am J Respir Crit Care Med. (2007); 175: 22-31.

51. Lane PM, Lam S, McWilliams A, Leriche JC, Anderson MW, Macaulay CE. Confocal fluorescence microendoscopy of bronchial epithelium. J Biomed Opt. (2009); 14: 024008.

52. Thiberville L, Salaun M, Lachkar S, Dominique S, Moreno-Swirc S, Vever-Bizet C, et al. Confocal fluorescence endomicroscopy of the human airways. Proc Am Thorac Soc. (2009); 6: 444-449.

53. Kiesslich R, Goetz M, Vieth M, Galle PR, Neurath MF. Confocal laser endomicroscopy. Gastrointest Endosc Clin N Am. (2005); 15: 715-731.

54. Information NLoMUNCfB. Molecular Imaging and Contrast Agent Database (MICAD). (2011). http://micad.nih.gov.

55. Administration USFaD. Drugs@FDA: FDA Approved Drug Products. (2011). http://www.accessdata.fda.gov/scripts/cder/drugsatfda/index.cfm.

56. Gheonea DI, Saftoiu A, Ciurea T, Popescu C, Georgescu CV, Malos A. Confocal laser endomicroscopy of the colon. J Gastrointestin Liver Dis. (2010); 19: 207-211.

57. Goetz M, Toermer T, Vieth M, Dunbar K, Hoffman A, Galle PR, et al. Simultaneous confocal laser endomicroscopy and chromoendoscopy with topical cresyl violet. Gastrointestinal Endoscopy. (2009); 70: 959-968.

58. Pierce MC, Javier DJ, Richards-Kortum R. Optical contrast agents and imaging systems for detection and diagnosis of cancer. Int J Cancer. (2008); 123: 1979-1990.

59. Becker A, Hessenius C, Licha K, Ebert B, Sukowski U, Semmler W, et al. Receptor-targeted optical imaging of tumors with near-infrared fluorescent ligands. Nat Biotechnol. (2001); 19: 327-331.

60. Hsiung PL, Hardy J, Friedland S, Soetikno R, Du CB, Wu AP, et al. Detection of colonic dysplasia in vivo using a targeted heptapeptide and confocal microendoscopy. Nat Med. (2008); 14: 454-458.

61. Hsu ER, Gillenwater AM, Hasan MQ, Williams MD, El-Naggar AK, Richards-Kortum RR. Real-time detection of epidermal growth factor receptor expression in fresh oral cavity biopsies using a molecular-specific contrast agent. Int J Cancer. (2006); 118: 3062-3071.

62. Goetz M, Ziebart A, Foersch S, Vieth M, Waldner MJ, Delaney P, et al. In vivo molecular imaging of colorectal cancer with confocal endomicroscopy by targeting epidermal growth factor receptor. Gastroenterology. (2010); 138: 435-446.

63. McLaren W, Anikijenko P, Barkla D, Delaney TP, King R. In vivo detection of experimental ulcerative colitis in rats using fiberoptic confocal imaging (FOCI). Dig Dis Sci. (2001); 46: 2263-2276.

64. Wang HW, Willis J, Canto MI, Sivak MV, Jr., Izatt JA. Quantitative laser scanning confocal autofluorescence microscopy of normal, premalignant, and malignant colonic tissues. IEEE Trans Biomed Eng. (1999); 46: 1246-1252.

65. Drezek R, Sokolov K, Utzinger U, Boiko I, Malpica A, Follen M, et al. Understanding the contributions of NADH and collagen to cervical tissue fluorescence spectra: Modeling, measurements, and implications. Journal of Biomedical Optics. (2001); 6: 385-396.

66. Collier T, Shen P, de Pradier B, Sung KB, Richards-Kortum R, Follen M, et al. Near real time confocal microscopy of amelanotic tissue: dynamics of aceto-whitening enable nuclear segmentation. Optics Express. (2000); 6: 40-48.

67. Collier T, Lacy A, Richards-Kortum R, Malpica A, Follen M. Near real-time confocal microscopy of amelanotic tissue: detection of dysplasia in ex vivo cervical tissue. Acad Radiol. (2002); 9: 504-512.

68. Wilson T. Optical Sectioning in Confocal Fluorescent Microscopes. Journal of Microscopy-Oxford. (1989); 154: 143-156.

69. Gareau DS, Li YB, Huang B, Eastman Z, Nehal KS, Rajadhyaksha M. Confocal mosaicing microscopy in Mohs skin excisions: feasibility of rapid surgical pathology. Journal of Biomedical Optics. (2008); 13: 054001-054001.

70. Loftus EV, Jr. The burden of inflammatory bowel disease in the United States: a moving target? Clin Gastroenterol Hepatol. (2007); 5: 1383-1384.

71. Strober W, Fuss I, Mannon P. The fundamental basis of inflammatory bowel disease. J Clin Invest. (2007); 117: 514-521.

72. American Cancer Society. (2008) Colorectal Cancer Facts & Figures 2008-2010. Atlanta: American Cancer Society.

73. Podolsky DK. Inflammatory bowel disease. N Engl J Med. (2002); 347: 417-429.

74. Itzkowitz SH, Yio X. Inflammation and cancer IV. Colorectal cancer in inflammatory bowel disease: the role of inflammation. Am J Physiol Gastrointest Liver Physiol. (2004); 287: G7-17.

75. Levin B, Lieberman DA, McFarland B, Smith RA, Brooks D, Andrews KS, et al. Screening and surveillance for the early detection of colorectal cancer and adenomatous polyps, 2008: a joint guideline from the American Cancer Society, the US Multi-Society Task Force on Colorectal Cancer, and the American College of Radiology. CA Cancer J Clin. (2008); 58: 130-160.

76. Larsson SC, Wolk A. Meat consumption and risk of colorectal cancer: a meta-analysis of prospective studies. Int J Cancer. (2006); 119: 2657-2664.

77. Jia Q, Lupton JR, Smith R, Weeks BR, Callaway E, Davidson LA, et al. Reduced colitis-associated colon cancer in Fat-1 (n-3 fatty acid desaturase) transgenic mice. Cancer Res. (2008); 68: 3985-3991.

78. Chapkin RS, Seo JM, McMurray DN, Lupton JR. Mechanisms by which docosahexaenoic acid and related fatty acids reduce colon cancer risk and inflammatory disorders of the intestine. Chemistry and Physics of Lipids. (2008); 153: 14-23.

79. Chapkin RS, McMurray DN, Lupton JR. Colon cancer, fatty acids and anti-inflammatory compounds. Curr Opin Gastroenterol. (2007); 23: 48-54.

80. Levine DS, Haggitt RC. Normal histology of the colon. Am J Surg Pathol. (1989); 13: 966-984.

81. Liu JTC, Mandella MJ, Friedland S, Soetikno R, Crawford JM, Contag CH, et al. Dual-axes confocal reflectance microscope for distinguishing colonic neoplasia. Journal of Biomedical Optics. (2006); 11: 054019-054019.

82. Watanabe O, Ando T, Maeda O, Hasegawa M, Ishikawa D, Ishiguro K, et al. Confocal endomicroscopy in patients with ulcerative colitis. Journal of Gastroenterology and Hepatology. (2008); 23: S286-S290.

83. Park CM, Reid PE, Walker DC, MacPherson BR. A simple, practical 'swiss roll' method of preparing tissues for paraffin or methacrylate embedding. J Microsc. (1987); 145: 115-120.

84. Amos WB, White JG. How the Confocal Laser Scanning Microscope entered Biological Research. Biology of the Cell. (2003); 95: 335-342.

85. Hoffman A, Goetz M, Vieth M, Galle PR, Neurath MF, Kiesslich R. Confocal laser endomicroscopy: technical status and current indications. Endoscopy. (2006); 38: 1275-1283.

86. Minsky M. Memoir on Inventing the Confocal Scanning Microscope. Scanning. (1988); 10: 128-138.

87. Sheppard C. 15 years of scanning optical microscopy at Oxford. SPIE MILESTONE SERIES MS. (1996); 131: 18-21.

88. Davidovits P. Scanning laser microscope. Nature. (1969); 223: 831-831.

89. Brakenhoff GJ, Blom P, Barends P. Confocal Scanning Light-Microscopy with High Aperture Immersion Lenses. Journal of Microscopy-Oxford. (1979); 117: 219-232.

90. White JG, Amos WB, Fordham M. An evaluation of confocal versus conventional imaging of biological structures by fluorescence light microscopy. Journal of Cell Biology. (1987); 105: 41-48.

91. Patel YG, Nehal KS, Aranda I, Li Y, Halpern AC, Rajadhyaksha M. Confocal reflectance mosaicing of basal cell carcinomas in Mohs surgical skin excisions. J Biomed Opt. (2007); 12: 034027-034027.

92. Kang D, Suter MJ, Boudoux C, Yoo H, Yachimski PS, Puricelli WP, et al. Comprehensive imaging of gastroesophageal biopsy samples by spectrally encoded confocal microscopy. Gastrointest Endosc. (2010); 71: 35-43.

93. Kim P, Chung E, Yamashita H, Hung KE, Mizoguchi A, Kucherlapati R, et al. In vivo wide-area cellular imaging by side-view endomicroscopy. Nat Methods. (2010); 7: 303-305.

94. Cooper HS, Murthy SN, Shah RS, Sedergran DJ. Clinicopathologic study of dextran sulfate sodium experimental murine colitis. Lab Invest. (1993); 69: 238-249.

95. Tanaka T, Kohno H, Suzuki R, Yamada Y, Sugie S, Mori H. A novel inflammation-related mouse colon carcinogenesis model induced by azoxymethane and dextran sodium sulfate. Cancer Sci. (2003); 94: 965-973.

96. McLellan EA, Medline A, Bird RP. Dose response and proliferative characteristics of aberrant crypt foci: putative preneoplastic lesions in rat colon. Carcinogenesis. (1991); 12: 2093-2098.

97. Luck BL, Carlson KD, Bovik AC, Richards-Kortum RR. An image model and segmentation algorithm for reflectance confocal images of in vivo cervical tissue. IEEE Trans Image Process. (2005); 14: 1265-1276.

98. Luck BL, Bovik AC, Richards-Kortum RR. Segmenting cervical epithelial nuclei from confocal images Gaussian Markov random fields; 2003. IEEE International Conference on Image Processing. pp. 1069-1072.

99. Dunn AK, Smithpeter C, Welch AJ, Richards-Kortum R. Sources of contrast in confocal reflectance imaging. Applied Optics. (1996); 35: 3441-3446.

100. Anuthama K, Sherlin HJ, Anuja N, Ramani P, Premkumar P, Chandrasekar T. Characterization of different tissue changes in normal, betel chewers, potentially malignant lesions, conditions and oral squamous cell carcinoma using reflectance confocal microscopy: Correlation with routine histopathology. Oral oncology. (2010); 46: 232-248.

101. Ma Z, Tavares JMRS, Jorge RN, Mascarenhas T. A review of algorithms for medical image segmentation and their applications to the female pelvic cavity. Computer Methods in Biomechanics and Biomedical Engineering. (2010); 13: 235-246.

102. Otsu N. A threshold selection method from gray-level histograms. Automatica. (1975); 11: 23-27.

103. Ziou D, Tabbone S. Edge detection techniques: An overview. International Journal of Pattern Recognition and Image Analysis. (1998); 8: 537-559.

104. Canny J. A computational approach to edge detection. Pattern Analysis and Machine Intelligence, IEEE Transactions on. (1986): 679-698.

105. Sobel I, Feldman G. A 3x3 isotropic gradient operator for image processing. a talk at the Stanford Artificial Project in. (1968): 271-272.

106. Prewitt JM. Object enhancement and extraction. Picture processing and Psychopictorics. (1970); 10: 15-19.

107. Lin G, Adiga U, Olson K, Guzowski JF, Barnes CA, Roysam B. A hybrid 3D watershed algorithm incorporating gradient cues and object models for automatic segmentation of nuclei in confocal image stacks. Cytometry A. (2003); 56: 23-36.

108. Belien JA, van Ginkel HA, Tekola P, Ploeger LS, Poulin NM, Baak JP, et al. Confocal DNA cytometry: a contour-based segmentation algorithm for automated three-dimensional image segmentation. Cytometry. (2002); 49: 12-21.

109. Sarti A, Ortiz de Solorzano C, Lockett S, Malladi R. A geometric model for 3-D confocal image analysis. IEEE Trans Biomed Eng. (2000); 47: 1600-1609.

110. Wang J, Trubuil A, Graffigne C, Kaeffer B. 3-D aggregated object detection and labeling from multivariate confocal microscopy images: a model validation approach. IEEE Trans Syst Man Cybern B Cybern. (2003); 33: 572-581.

111. Jiuxiang H, Razdan A, Nielson GM, Farin GE, Baluch DP, Capco DG. Volumetric segmentation using Weibull E-SD fields. IEEE Transactions on Visualization and Computer Graphics. (2003); 9: 320-328.

112. Luck BL, Carlson KD, Bovik AC, Richards-Kortum RR. An image model and segmentation algorithm for reflectance confocal images of in vivo cervical tissue. Ieee Transactions on Image Processing. (2005); 14: 1265-1276.

113. Eckhorn R, Reitboeck H, Arndt M, Dicke P. Feature linking via synchronization among distributed assemblies: Simulations of results from cat visual cortex. Neural Computation. (1990); 2: 293-307.

114. Lindblad T, Kinser JM, SpringerLink (Online service). Image processing using pulse-coupled neural networks. 2nd, rev. ed. Berlin; New York: Springer. (1998); pp. 2005-2018.

115. Ekblad U, Kinser JM. Theoretical foundation of the intersecting cortical model and its use for change detection of aircraft, cars, and nuclear explosion tests. Signal Processing. (2004); 84: 1131-1146.

116. Jabbour JM, Malik BH, Olsovsky C, Cuenca R, Cheng S, Jo JA, et al. Optical axial scanning in confocal microscopy using an electrically tunable lens. Biomed Opt Express. (2014); 5: 645-652.

117. Van AN, Harris MA, Maitland KC. Pulse Coupled Neural Network Segmentation Algorithm. (2014); Database: ZENODO. 10.5281/zenodo.12804.

118. Zhan K, Zhang H, Ma Y. New spiking cortical model for invariant texture retrieval and image processing. IEEE Transactions on Neural Networks. (2009); 20: 1980-1986.

119. Chen Y, Park SK, Ma Y, Ala R. A new automatic parameter setting method of a simplified PCNN for image segmentation. IEEE Trans Neural Netw. (2011); 22: 880-892.

120. Guns R, Lioma C, Larsen B. The tipping point: F-score as a function of the number of retrieved items. Information Processing & Management. (2012); 48: 1171-1180.

121. Ishimaru A. Wave propagation and scattering in random media. New York: Academic press. (1978).

122. Clark AL, Gillenwater AM, Collier TG, Alizadeh-Naderi R, El-Naggar AK, Richards-Kortum RR. Confocal microscopy for real-time detection of oral cavity neoplasia. Clin Cancer Res. (2003); 9: 4714-4721.

123. Sung KB, Richards-Kortum R, Follen M, Malpica A, Liang C, Descour MR. Fiber optic confocal reflectance microscopy: a new real-time technique to view nuclear morphology in cervical squamous epithelium in vivo. Optics Express. (2003); 11: 3171-3181.

124. Walker DC, Brown BH, Blackett AD, Tidy J, Smallwood RH. A study of the morphological parameters of cervical squamous epithelium. Physiological Measurement. (2003); 24: 121-135.

125. Landay MA, Schroeder HE. Quantitative electron microscopic analysis of the stratified epithelium of normal human buccal mucosa. Cell Tissue Res. (1977); 177: 383-405.

126. Landay MA, Schroeder HE. Differentiation in normal human buccal mucosa epithelium. Journal of Anatomy. (1979); 128: 31-51.

127. Ogden GR, Cowpe JG, Green M. Quantitative Exfoliative Cytology of Normal Buccal Mucosa - the Effect of Smoking. Journal of Dental Research. (1989); 68: 561-561.

128. Jin Y, White FH, Yang L. A histological morphometric study of nuclear size in benign and malignant neoplasms of the human cheek. Histopathology. (1993); 23: 271-274.

129. White FH, Jin Y, Yang L. An evaluation of the role of nuclear cytoplasmic ratios and nuclear volume densities as diagnostic indicators in metaplastic, dysplastic and neoplastic lesions of the human cheek. Histology and Histopathology. (1997); 12: 69-77.

130. Ramaesh T, Mendis BR, Ratnatunga N, Thattil RO. Cytomorphometric analysis of squames obtained from normal oral mucosa and lesions of oral leukoplakia and squamous cell carcinoma. J Oral Pathol Med. (1998); 27: 83-86.

131. de Arruda EP, Trevilatto PC, Camargo ES, Woyceichoski IEC, Machado MAN, Vieira I, et al. Preclinical Alterations of Oral Epithelial Cells in Contact with Orthodontic Appliances. Biomedical Papers-Olomouc. (2011); 155: 299-303.

132. Harris MA, Van AN, Malik BH, Jabbour JM, Maitland KC. A pulse coupled neural network segmentation algorithm for reflectance confocal images of epithelial tissue. PLoS One. (2015); 10: 1-20.

APPENDIX

SCM Segmentation MATLAB Code:

```
function varargout = SCM_seg(varargin)
% SCM_SEG MATLAB code for SCM_seg.fig
%      SCM_SEG, by itself, creates a new SCM_SEG or raises the existing
%      singleton*.
%
%      H = SCM_SEG returns the handle to a new SCM_SEG or the handle to
%      the existing singleton*.
%
%      SCM_SEG('CALLBACK',hObject,eventData,handles,...) calls the
local
%      function named CALLBACK in SCM_SEG.M with the given input
arguments.
%
%      SCM_SEG('Property','Value',...) creates a new SCM_SEG or raises
the
%      existing singleton*.  Starting from the left, property value
pairs are
%      applied to the GUI before SCM_seg_OpeningFcn gets called.  An
%      unrecognized property name or invalid value makes property
application
%      stop.  All inputs are passed to SCM_seg_OpeningFcn via varargin.
%
%      *See GUI Options on GUIDE's Tools menu.  Choose "GUI allows only
one
%      instance to run (singleton)".
%
% See also: GUIDE, GUIDATA, GUIHANDLES

% Edit the above text to modify the response to help SCM_seg

% Last Modified by GUIDE v2.5 19-Jun-2014 12:20:06

% Begin initialization code - DO NOT EDIT
gui_Singleton = 1;
gui_State = struct('gui_Name',       mfilename, ...
                   'gui_Singleton',  gui_Singleton, ...
                   'gui_OpeningFcn', @SCM_seg_OpeningFcn, ...
                   'gui_OutputFcn',  @SCM_seg_OutputFcn, ...
                   'gui_LayoutFcn',  [] , ...
                   'gui_Callback',   []);
if nargin && ischar(varargin{1}1)
    gui_State.gui_Callback = str2func(varargin{1});
end

if nargout
```

```
    [varargout{1:nargout}] = gui_mainfcn(gui_State, varargin{:});
else
    gui_mainfcn(gui_State, varargin{:});
end
% End initialization code - DO NOT EDIT

% DEFINE INITIAL VARIABLES/PARAMETERS HERE
% --- Executes just before SCM_seg is made visible.
function SCM_seg_OpeningFcn(hObject, eventdata, handles, varargin)
% This function has no output args, see OutputFcn.
% hObject    handle to figure
% eventdata  reserved - to be defined in a future version of MATLAB
% handles    structure with handles and user data (see GUIDATA)
% varargin   command line arguments to SCM_seg (see VARARGIN)

% Choose default command line output for SCM_seg
handles.output = '';

% Adjust settings
clc;
warning off all;

% Initialize Variables
handles.img{1} = 'null';
handles.seg = 0;
handles.filename = 0;
handles.pathname = 0;
handles.num = 0;
handles.B = 0;

% Get String Value and convert to double
handles.gsv =@(x) str2double(get(x,'String'));

% Get centroid function
handles.gcv=@(x,n) x(n).Centroid;

% Clear Table
set(handles.uitable1, 'Data', handles.B);

% Command Window Read
set(handles.listbox2, 'String', cmdwinout());

% Update handles structure
guidata(hObject, handles);

% UIWAIT makes SCM_seg wait for user response (see UIRESUME)

% --- Executes during object creation, after setting all properties.
function listbox1_CreateFcn(hObject, eventdata, handles)
% hObject    handle to listbox1 (see GCBO)
% eventdata  reserved - to be defined in a future version of MATLAB
```

```
% handles    empty - handles not created until after all CreateFcns
called

% Hint: listbox controls usually have a white background on Windows.
%       See ISPC and COMPUTER.
if ispc && isequal(get(hObject,'BackgroundColor'),
get(0,'defaultUicontrolBackgroundColor'))
    set(hObject,'BackgroundColor','white');
end

% --- Outputs from this function are returned to the command line.
function varargout = SCM_seg_OutputFcn(hObject, eventdata, handles)
% varargout  cell array for returning output args (see VARARGOUT);
% hObject    handle to figure
% eventdata  reserved - to be defined in a future version of MATLAB
% handles    structure with handles and user data (see GUIDATA)

varargout{1} = handles.output;

%%%%%%%%%%%%%%%%%%%%%% END COMPUTER GENERATED CODE
%%%%%%%%%%%%%%%%%%%%%%
%%%%%%%%%%%%%%%%%%%%%% START USER GENERATED CODE
%%%%%%%%%%%%%%%%%%%%%%

% Open Image
% --- Executes on button press in pushbutton1.
function pushbutton1_Callback(hObject, eventdata, handles)
% hObject    handle to pushbutton1 (see GCBO)
% eventdata  reserved - to be defined in a future version of MATLAB
% handles    structure with handles and user data (see GUIDATA)

[handles.filename, handles.pathname, ~] =
uigetfile({'*.bmp';'*.jpg';...
    '*.png';'*.tif';'*.tiff';}, 'File Selector', 'MultiSelect', 'on');

if ~isequal(handles.filename, 0)

    % If filename not cell array, make cell array
    if ~iscell(handles.filename)
        handles.filename = {handles.filename};
    end

    % Find the number of files opened
    handles.num = size(handles.filename ,2);

    % Create cell array
    handles.img = cell(1, handles.num);
    name = cell(1, handles.num);

    % Save each image/filename to memory
    for n=1:handles.num
```

```
        handles.img{n} = imread([handles.pathname
handles.filename{n}]);
        [path, name{n}, ~] = fileparts(handles.filename{n});
%#ok<ASGLU>
    end

    % Output List of images to listbox
    set(handles.listbox1, 'string', name);
    imshow(handles.img{1});
    handles.B = cell(handles.num+1);
    [handles.B{:}] = deal(0);
    set(handles.uitable1, 'Data', 0);
    handles.outputimg = handles.img;

    disp('#Files Selected!');
    set(handles.listbox2, 'String', cmdwinout());
else
    disp('#No Files Selected!');
    set(handles.listbox2, 'String', cmdwinout());
end

% Update variables to figure
set(handles.listbox2,'Value', length(cmdwinout()));
guidata(hObject, handles);

% Segment Image
% --- Executes on button press in pushbutton2.
function pushbutton2_Callback(hObject, eventdata, handles)
% hObject    handle to pushbutton2 (see GCBO)
% eventdata  reserved - to be defined in a future version of MATLAB
% handles    structure with handles and user data (see GUIDATA)

if ~strcmp(handles.img{1}, 'null') && ~strcmp(handles.img{1},
'segmented')

    % Initialize Varaibles
    handles.centroid = cell(1, handles.num);
    raw_area = cell(1, handles.num);
    obj_intensity = cell(1, handles.num);
    sd_obj_intensity = cell(1, handles.num);
    bg_intensity = zeros(1, handles.num+1);
    sd_bg_intensity = zeros(1, handles.num+1);
    NCR = zeros(1, handles.num+1);
    numberofobjects = zeros(1, handles.num+1);
    mean_area = zeros(1, handles.num+1);
    std_area = zeros(1, handles.num+1);
    mean_eccentricity = zeros(1, handles.num+1);
    std_eccentricity = zeros(1, handles.num+1);
    nameoffiles = cell(1, handles.num+1);

    % Choose Save Directory, if Save Image is TRUE
    if get(handles.checkbox1,'Value')
```

```
        savedirectory = uigetdir(handles.pathname, 'Directory to
Save');

        % Check if got directory successfully
        if savedirectory(1) ~= 0

        [xlssavename, xlspath, ~] = uiputfile({'*.xls';},...
            'Name Excel File', savedirectory);

            % Check if valid filename
            if (xlssavename(1) ~= 0) && (xlspath(1) ~= 0)
            % Excel Filename Failed
            else
                disp('#Invalid xls filename');
                set(handles.listbox2, 'String', cmdwinout());
                return;
            end

        % No Directory Chosen or Invalid Directory
        else
            disp('#Invalid or No Directory Chosen');
            set(handles.listbox2, 'String', cmdwinout());
            return;
        end
    end

    % Create waitbar
    h = waitbar(0, 'Segmenting Image(s)');

    % Create cells for segmented images
    handles.seg = cell(1, handles.num);

    % Get Parameters specified in options panel
    handles.maxarea = handles.gsv(handles.edit6);
    handles.minarea = handles.gsv(handles.edit8);
    handles.eccentricity = handles.gsv(handles.edit9);
    handles.solidity = handles.gsv(handles.edit11);
    handles.rb = handles.gsv(handles.edit16);
    handles.lateralres = (handles.gsv(handles.edit17)).^2;
    handles.res = handles.gsv(handles.edit18);

    for n=1:handles.num
        % Segmentation
        I = formatgrayscale(handles.img{n}, 'N');
        I = imcrop(double(I)/255,[1 1 999 999]);
        [w, l] = size(I);

        if ~get(handles.checkbox4,'Value')
            bg_area = 1000000;
            d_mask = ones(w,l);
            cut_mask = d_mask;
        else
```

```
            [~, bg_area, d_mask] = bg_remove(I, handles.listbox2);
            se = strel('disk',handles.rb);
            cut_mask = imerode(d_mask,se);
        end
        [filter_img, I_crop] = SCM(I, w, l,...
            handles.maxarea, handles.minarea,...
            handles.eccentricity, handles.solidity, 'Y',...
            d_mask, cut_mask, handles.lateralres, handles.listbox2);

        % Update variables to figure
        set(handles.listbox2,'Value', length(cmdwinout()));
        guidata(hObject, handles);

        % Outline Image
        BWoutline = bwperim(filter_img);
        Segout_R = I_crop; Segout_R(BWoutline) = 255;
        Segout_G = I_crop; Segout_G(BWoutline) = 0;
        Segout_B = I_crop; Segout_B(BWoutline) = 0;
        if get(handles.checkbox4,'Value')
            BGoutline = bwperim(d_mask);
            % Subtract where border objects intersect
            intersect = (double(BGoutline) - double(BWoutline)) == 1;
            Segout_R(intersect) = 0;
            Segout_G(BGoutline) = 0;
            Segout_B(BGoutline) = 255;
        end
        handles.seg{n} = cat(3, Segout_R, Segout_G, Segout_B);
        % imwrite(handles.seg{n}, '13_segmentedimage.png', 'png');

        % Get Image Info
        prop = regionprops(bwconncomp(filter_img), I, 'All');

        % Get 2 - 5 pixels from objects for bg
        se1 = strel('disk',5);
        se2 = strel('disk',2);
        bg = imdilate(filter_img,se1) - imdilate(filter_img,se2);
        prop2 = regionprops(bwconncomp(bg), I, 'All');

        % Save prop to get centroid for each object
        handles.centroid{n} = prop;

        % Get area and sd area for each object
        raw_area{n} = (handles.lateralres*[prop.Area])';

        % Get intensity and sd intensity for each object
        obj_intensity{n} = ([prop.MeanIntensity])';
        sd_obj_intensity{n} = ([prop.MaxIntensity]-
[prop.MinIntensity])'/4;

        % Get bg intensity and sd bg intensity
        bg_intensity(n+1) = mean([prop2.MeanIntensity]);
        sd_bg_intensity(n+1) = mean(([prop2.MaxIntensity]...
```

```
            -[prop2.MinIntensity])'/4);

        % Get NCR, # of obj, mean area, sd area, mean eccen, sd eccen
        NCR(n+1) = sum([prop.Area])/(bg_area - sum([prop.Area]));
        numberofobjects(n+1) = length(prop);
        mean_area(n+1) = handles.lateralres*mean([prop.Area]);
        std_area(n+1) = handles.lateralres*std([prop.Area]);
        mean_eccentricity(n+1) = mean([prop.Eccentricity]);
        std_eccentricity(n+1) = std([prop.Eccentricity]);

        % Save Image
        [path, name, ~] = fileparts(handles.filename{n}); %#ok<ASGLU>
        disp(['#Saving Image... ' name]);
        set(handles.listbox2, 'String', cmdwinout());

        % Update variables to figure
        set(handles.listbox2,'Value', length(cmdwinout()));
        guidata(hObject, handles);

        % Save Image to file
        if get(handles.checkbox1,'Value')
            if ispc()
                imwrite(handles.seg{n}, [savedirectory '\seg_' name...
                '.tif' ], 'tif', 'Resolution', [handles.res
handles.res]);
            else
                imwrite(handles.seg{n}, [savedirectory '/seg_' name...
                '.tif' ], 'tif', 'Resolution', [handles.res
handles.res]);
            end
        end

        % Index Filename
        nameoffiles{n+1} = name;

        % Update waitbar()
        waitbar(n/handles.num);
    end

    % Create table from data
    for i=2:handles.num+1
            raw_area{i-1} = cellstr(num2str(raw_area{i-1}))';
            obj_intensity{i-1} = cellstr(num2str(obj_intensity{i-1}))';
            sd_obj_intensity{i-1} = cellstr(...
                num2str(sd_obj_intensity{i-1}))';
    end
    % Check if using PC
    if ispc()
        NCR = num2cell(NCR);
        numberofobjects = num2cell(numberofobjects);
        mean_area = num2cell(mean_area);
        std_area = num2cell(std_area);
```

```
    mean_eccentricity = num2cell(mean_eccentricity);
    std_eccentricity = num2cell(std_eccentricity);
    bg_intensity = num2cell(bg_intensity);
    sd_bg_intensity = num2cell(sd_bg_intensity);
else
    NCR = cellstr(num2str(NCR'))';
    numberofobjects = cellstr(num2str(numberofobjects'))';
    mean_area = cellstr(num2str(mean_area'))';
    std_area = cellstr(num2str(std_area'))';
    mean_eccentricity = cellstr(num2str(mean_eccentricity'))';
    std_eccentricity = cellstr(num2str(std_eccentricity'))';
    bg_intensity = cellstr(num2str(bg_intensity'))';
    sd_bg_intensity = cellstr(num2str(sd_bg_intensity'))';
end

% Set names for data table display
nameoffiles{1} = 'Image';
NCR{1} = 'NCR';
numberofobjects{1} = '# of Objects';
mean_area{1} = 'Average Area';
std_area{1} = 'SD Area';
mean_eccentricity{1} = 'Average Eccentricity';
std_eccentricity{1} = 'SD Eccentricity';
bg_intensity{1} = 'Mean BG Intensity';
sd_bg_intensity{1} = 'SD BG Intensity';

% Data Table Display
handles.B = [(nameoffiles); (NCR);...
    (numberofobjects); (mean_area); (std_area);...
    (mean_eccentricity); (std_eccentricity);...
    (bg_intensity); (sd_bg_intensity);];

if get(handles.checkbox1,'Value')
    % Excel Data Table
    A = [(nameoffiles)', (NCR)',...
        (numberofobjects)', (mean_area)', (std_area)',...
        (mean_eccentricity)', (std_eccentricity)',...
        (bg_intensity)', (sd_bg_intensity)'];

    % Create Empty Cell
    C = {};

    % Nuclei Area Data (Unaveraged)
    for k = 2:((handles.num)+1)
    C = [C; [cellstr(repmat(nameoffiles{k},...
        length(raw_area{k-1}),1)),(raw_area{k-1})',...
        (obj_intensity{k-1})',(sd_obj_intensity{k-1})',...
        cellstr(num2str((1:length(raw_area{k-1}))'))]]; %#ok<AGROW>
    end

    % Write to spreadsheet
    if ispc
```

```
            xlswrite([xlspath xlssavename], A);

            % Nuclei Area Data (Unaveraged)
            xlswrite([xlspath 'raw_data.xls'], C);
        else
            fid=fopen([xlspath strtok(xlssavename, '.') '.csv'],'wt');

            [rows, ~]=size(A);

            for i=1:rows
                fprintf(fid,'%s,',A{i,1:end-1});
                fprintf(fid,'%s\n',A{i,end});
            end

            fclose(fid);

            % Nuclei Area Data (Unaveraged)
            fid=fopen([xlspath strtok('raw_data.xls', '.')
'.csv'],'wt');

            [rows, ~]=size(C);

            for i=1:rows
                fprintf(fid,'%s,',C{i,1:end-1});
                fprintf(fid,'%s\n',C{i,end});
            end

            fclose(fid);
        end
    end

    % Show Image and close loading bar
    disp('#DONE!');
    set(handles.listbox2, 'String', cmdwinout());
    close(h);
    imshow(handles.seg{n});

    % Label Objects
%     hold on;
%     for k = 1:numel(handles.centroid{n})
%         x = handles.gcv(handles.centroid{n},k);
%         text(x(1),x(2),sprintf('%d',k),...
%             'HorizontalAlignment', 'center',...
%             'VerticalAlignment', 'middle',...
%             'Color', [1,0.6,0]);
%     end
%     hold off;

    % Display table
    set(handles.uitable1, 'Data', [handles.B(:,1) handles.B(:,n+1)]);
    handles.outputimg = handles.seg;
```

```
    handles.img = {'segmented'};

elseif strcmp(handles.img{1}, 'segmented')
    disp('#Image(s) already segmented, load new image(s) to segment');
    set(handles.listbox2, 'String', cmdwinout());
else
    disp('#No Image Loaded, Open Image First!');
    set(handles.listbox2, 'String', cmdwinout());
end

% Update variables to figure
set(handles.listbox2,'Value', length(cmdwinout()));
guidata(hObject, handles);

% Open Settings Panel
% --- Executes on button press in pushbutton5.
function pushbutton5_Callback(hObject, eventdata, handles)
% hObject    handle to pushbutton5 (see GCBO)
% eventdata  reserved - to be defined in a future version of MATLAB
% handles    structure with handles and user data (see GUIDATA)

if strcmp(get(handles.uipanel3, 'Visible'),'off')
    set(handles.uipanel3, 'Visible', 'on');
else
    set(handles.uipanel3, 'Visible', 'off');
end

% Selection Listbox
% --- Executes on selection change in listbox1.
function listbox1_Callback(hObject, eventdata, handles)
% hObject    handle to listbox1 (see GCBO)
% eventdata  reserved - to be defined in a future version of MATLAB
% handles    structure with handles and user data (see GUIDATA)
% Hints: contents = cellstr(get(hObject,'String')) returns listbox1
contents as cell array
%        contents{get(hObject,'Value')} returns selected item from
listbox1

% Get current selected image
index = get(handles.listbox1,'value');

% Display current selected image
imshow(handles.outputimg{index});

% % Label Objects
% hold on;
% for k = 1:numel(handles.centroid{index})
%     x = handles.gcv(handles.centroid{index},k);
%     text(x(1),x(2),sprintf('%d',k),...
%         'HorizontalAlignment', 'center',...
%         'VerticalAlignment', 'middle',...
%         'Color', [1,0.6,0]);
```

```
% end
% hold off;

% Set data table
set(handles.uitable1, 'Data', [handles.B(:,1) handles.B(:,index+1)]);

% update variables
guidata(hObject, handles);

% Exit Attempt
% --- Executes when user attempts to close mainbox.
function mainbox_CloseRequestFcn(hObject, eventdata, handles)
% hObject    handle to mainbox (see GCBO)
% eventdata  reserved - to be defined in a future version of MATLAB
% handles    structure with handles and user data (see GUIDATA)

if isequal(get(hObject, 'waitstatus'), 'waiting')
    % The GUI is still in UIWAIT, use UIRESUME
    uiresume(hObject);
    delete(hObject);
else
    % The GUI is no longer waiting, just close it
    delete(hObject);
end

% Exit
% --- Executes on button press in pushbutton6.
function pushbutton6_Callback(hObject, eventdata, handles)
% hObject    handle to pushbutton6 (see GCBO)
% eventdata  reserved - to be defined in a future version of MATLAB
% handles    structure with handles and user data (see GUIDATA)

if isequal(get(handles.mainbox, 'waitstatus'), 'waiting')
    % The GUI is still in UIWAIT, use UIRESUME
    uiresume(handles.mainbox);
    delete(handles.mainbox);
else
    % The GUI is no longer waiting, just close it
    delete(handles.mainbox);
end

%%%%%%%%%%%%%%%%%%%%%%%%%%%%%%%% NOT USED
%%%%%%%%%%%%%%%%%%%%%%%%%%%%%%%%

% --- Executes on button press in checkbox1.
function checkbox1_Callback(hObject, eventdata, handles)
% hObject    handle to checkbox1 (see GCBO)
% eventdata  reserved - to be defined in a future version of MATLAB
% handles    structure with handles and user data (see GUIDATA)
% Hint: get(hObject,'Value') returns toggle state of checkbox1

% --- Executes on button press in checkbox4.
```

```
function checkbox4_Callback(hObject, eventdata, handles)
% hObject    handle to checkbox4 (see GCBO)
% eventdata  reserved - to be defined in a future version of MATLAB
% handles    structure with handles and user data (see GUIDATA)

% Hint: get(hObject,'Value') returns toggle state of checkbox4

% --- Executes during object creation, after setting all properties.
function edit6_CreateFcn(hObject, eventdata, handles)
% hObject    handle to edit6 (see GCBO)
% eventdata  reserved - to be defined in a future version of MATLAB
% handles    empty - handles not created until after all CreateFcns
called

% Hint: edit controls usually have a white background on Windows.
%       See ISPC and COMPUTER.
if ispc && isequal(get(hObject,'BackgroundColor'),
get(0,'defaultUicontrolBackgroundColor'))
    set(hObject,'BackgroundColor','white');
end

% --- Executes during object creation, after setting all properties.
function edit8_CreateFcn(hObject, eventdata, handles)
% hObject    handle to edit8 (see GCBO)
% eventdata  reserved - to be defined in a future version of MATLAB
% handles    empty - handles not created until after all CreateFcns
called

% Hint: edit controls usually have a white background on Windows.
%       See ISPC and COMPUTER.
if ispc && isequal(get(hObject,'BackgroundColor'),
get(0,'defaultUicontrolBackgroundColor'))
    set(hObject,'BackgroundColor','white');
end

% --- Executes during object creation, after setting all properties.
function edit9_CreateFcn(hObject, eventdata, handles)
% hObject    handle to edit9 (see GCBO)
% eventdata  reserved - to be defined in a future version of MATLAB
% handles    empty - handles not created until after all CreateFcns
called

% Hint: edit controls usually have a white background on Windows.
%       See ISPC and COMPUTER.
if ispc && isequal(get(hObject,'BackgroundColor'),
get(0,'defaultUicontrolBackgroundColor'))
    set(hObject,'BackgroundColor','white');
end

% --- Executes during object creation, after setting all properties.
function edit10_CreateFcn(hObject, eventdata, handles)
% hObject    handle to edit10 (see GCBO)
```

```
% eventdata  reserved - to be defined in a future version of MATLAB
% handles    empty - handles not created until after all CreateFcns
called

% Hint: edit controls usually have a white background on Windows.
%       See ISPC and COMPUTER.
if ispc && isequal(get(hObject,'BackgroundColor'),
get(0,'defaultUicontrolBackgroundColor'))
    set(hObject,'BackgroundColor','white');
end

% --- Executes during object creation, after setting all properties.
function edit11_CreateFcn(hObject, eventdata, handles)
% hObject    handle to edit11 (see GCBO)
% eventdata  reserved - to be defined in a future version of MATLAB
% handles    empty - handles not created until after all CreateFcns
called

% Hint: edit controls usually have a white background on Windows.
%       See ISPC and COMPUTER.
if ispc && isequal(get(hObject,'BackgroundColor'),
get(0,'defaultUicontrolBackgroundColor'))
    set(hObject,'BackgroundColor','white');
end

% --- Executes during object creation, after setting all properties.
function edit16_CreateFcn(hObject, eventdata, handles)
% hObject    handle to edit16 (see GCBO)
% eventdata  reserved - to be defined in a future version of MATLAB
% handles    empty - handles not created until after all CreateFcns
called

% Hint: edit controls usually have a white background on Windows.
%       See ISPC and COMPUTER.
if ispc && isequal(get(hObject,'BackgroundColor'),
get(0,'defaultUicontrolBackgroundColor'))
    set(hObject,'BackgroundColor','white');
end

% --- Executes during object creation, after setting all properties.
function listbox2_CreateFcn(hObject, eventdata, handles)
% hObject    handle to listbox2 (see GCBO)
% eventdata  reserved - to be defined in a future version of MATLAB
% handles    empty - handles not created until after all CreateFcns
called

% Hint: listbox controls usually have a white background on Windows.
%       See ISPC and COMPUTER.
if ispc && isequal(get(hObject,'BackgroundColor'),
get(0,'defaultUicontrolBackgroundColor'))
    set(hObject,'BackgroundColor','white');
end
```

```
function edit6_Callback(hObject, eventdata, handles)
% hObject    handle to edit6 (see GCBO)
% eventdata  reserved - to be defined in a future version of MATLAB
% handles    structure with handles and user data (see GUIDATA)
% Hints: get(hObject,'String') returns contents of edit6 as text
%        str2double(get(hObject,'String')) returns contents of edit6 as
a double

function edit8_Callback(hObject, eventdata, handles)
% hObject    handle to edit8 (see GCBO)
% eventdata  reserved - to be defined in a future version of MATLAB
% handles    structure with handles and user data (see GUIDATA)
% Hints: get(hObject,'String') returns contents of edit8 as text
%        str2double(get(hObject,'String')) returns contents of edit8 as
a double

function edit9_Callback(hObject, eventdata, handles)
% hObject    handle to edit9 (see GCBO)
% eventdata  reserved - to be defined in a future version of MATLAB
% handles    structure with handles and user data (see GUIDATA)
% Hints: get(hObject,'String') returns contents of edit9 as text
%        str2double(get(hObject,'String')) returns contents of edit9 as
a double

function edit10_Callback(hObject, eventdata, handles)
% hObject    handle to edit10 (see GCBO)
% eventdata  reserved - to be defined in a future version of MATLAB
% handles    structure with handles and user data (see GUIDATA)
% Hints: get(hObject,'String') returns contents of edit10 as text
%        str2double(get(hObject,'String')) returns contents of edit10
as a double

function edit11_Callback(hObject, eventdata, handles)
% hObject    handle to edit11 (see GCBO)
% eventdata  reserved - to be defined in a future version of MATLAB
% handles    structure with handles and user data (see GUIDATA)
% Hints: get(hObject,'String') returns contents of edit11 as text
%        str2double(get(hObject,'String')) returns contents of edit11
as a double

function edit16_Callback(hObject, eventdata, handles)
% hObject    handle to edit16 (see GCBO)
% eventdata  reserved - to be defined in a future version of MATLAB
% handles    structure with handles and user data (see GUIDATA)

% Hints: get(hObject,'String') returns contents of edit16 as text
%        str2double(get(hObject,'String')) returns contents of edit16
as a double

% --- Executes on selection change in listbox2.
function listbox2_Callback(hObject, eventdata, handles)
```

```
% hObject    handle to listbox2 (see GCBO)
% eventdata  reserved - to be defined in a future version of MATLAB
% handles    structure with handles and user data (see GUIDATA)

% Hints: contents = cellstr(get(hObject,'String')) returns listbox2
contents as cell array
%        contents{get(hObject,'Value')} returns selected item from
listbox2

function edit17_Callback(hObject, eventdata, handles)
% hObject    handle to edit17 (see GCBO)
% eventdata  reserved - to be defined in a future version of MATLAB
% handles    structure with handles and user data (see GUIDATA)

% Hints: get(hObject,'String') returns contents of edit17 as text
%        str2double(get(hObject,'String')) returns contents of edit17
as a double


% --- Executes during object creation, after setting all properties.
function edit17_CreateFcn(hObject, eventdata, handles)
% hObject    handle to edit17 (see GCBO)
% eventdata  reserved - to be defined in a future version of MATLAB
% handles    empty - handles not created until after all CreateFcns
called

% Hint: edit controls usually have a white background on Windows.
%       See ISPC and COMPUTER.
if ispc && isequal(get(hObject,'BackgroundColor'),
get(0,'defaultUicontrolBackgroundColor'))
    set(hObject,'BackgroundColor','white');
end



function edit18_Callback(hObject, eventdata, handles)
% hObject    handle to edit18 (see GCBO)
% eventdata  reserved - to be defined in a future version of MATLAB
% handles    structure with handles and user data (see GUIDATA)

% Hints: get(hObject,'String') returns contents of edit18 as text
%        str2double(get(hObject,'String')) returns contents of edit18
as a double


% --- Executes during object creation, after setting all properties.
function edit18_CreateFcn(hObject, eventdata, handles)
% hObject    handle to edit18 (see GCBO)
% eventdata  reserved - to be defined in a future version of MATLAB
% handles    empty - handles not created until after all CreateFcns
called
```

```
% Hint: edit controls usually have a white background on Windows.
%       See ISPC and COMPUTER.
if ispc && isequal(get(hObject,'BackgroundColor'),
get(0,'defaultUicontrolBackgroundColor'))
    set(hObject,'BackgroundColor','white');
end
```